KINEMATIC STUDIES OF EXTENDED OBJECTS IN ASTROPHYSICS USING HIGH-RESOLUTION SPECTROSCOPY

BY

DIPANKAR PRASHANT KUMAR BANERJEE

PHYSICAL RESEARCH LABORATORY

AHMEDABAD - 380009

INDIA

A THESIS

SUBMITTED TO THE GUJARAT UNIVERSITY
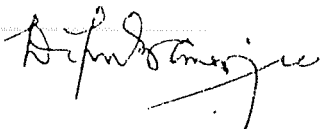
FOR THE DEGREE OF

DOCTOR OF PHILOSOPHY
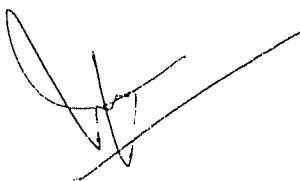
AUGUST 1990

CERTIFICATE

I hereby declare that the work presented in this thesis is original and has not formed the basis for the award of any degree or diploma by any University or Institution.

Author

DIPANKAR. P. K. BANERJEE
Physical Research Laboratory
Ahmedabad - 380009, India

Certified by

J. N. DESAI
Professor- in -charge
Physical Research Laboratory
Ahmedabad - 380009, India

SPATIO-KINEMATIC INVESTIGATIONS OF PLANETARY NEBULAE

CONTENTS

CHAPTER III: KINEMATIC OBSERVATIONS OF SELECTED PLANETARY NEBULAE

CHAPTER IV: SPATIO-KINEMATIC MODELS FOR THE OBSERVED PLANETARY NEBULAE

CHAPTER V: A PHYSICAL MECHANISM FOR THE STRUCTURAL DEVELOPMENT OF PLANETARY NEBULAE ENVELOPES

CHAPTER VI: SUMMARY AND SCOPE FOR FUTURE WORK

REFERENCES

STATEMENT

The work contained in this thesis has been carried out at the Physical Research Laboratory, Ahmedabad under the supervision of Prof. B.G.Anandarao. The observations of all the planetary nebulae described herein have been made at the Vainu Bappu Observatory, Kavalur.

The contents of this thesis are divided into six chapters. Chapter I contains an introductory review of planetary nebulae (PNe). Here the general properties and characteristics of PNe, the important physical processes ocurring in them and the viable physical mechanisms for the formation and structural development of PNe shells are described. The relevance and importance of the kinematic studies of PNe are highlighted and the aims and scope of the thesis are indicated.

Chapter II deals with the experimental techniques and instrumentation used for the observations. The basic theory of the Fabry-Pérot spectrometer is given. The design, fabrication and performance evaluation of a high-resolution, piezo-scanning, servo-controlled Fabry-Pérot spectrometer which was constructed for the present studies is discussed. In this chapter an analysis of the errors in observations is also made and the numerical methods for data analysis and reduction are also discussed.

In Chapter III the author presents the kinematic observations made on selected planetary nebulae and indicates the main results. A detailed discussion is then made of five PNe viz.

IC 4593, NGC 6153, NGC 2818, IC 4406 and NGC 6302 emphasizing the important and new kinematic results that have been obtained in them. In particular , some of the unusual kinematic features found in these PNe and the probable physical processes which give rise to them are discussed. For instance,in NGC 2818, unusual triple-structured line profiles are found in the [OIII], [NII] and Hα lines. In the case of NGC 6153, evidence is found for the presence of a fast bipolar flow. Finally, in the multiple shell planetary nebula IC 4593, the kinematic results indicate that the outer shell is expanding faster than the inner shell - a relatively rare occurence.

In Chapter IV the author discusses the observed kinematics of five PNe viz. NGC 2440, 2346, 1535, 5882 and 650/1 which were studied relatively more extensively than the PNe discussed in Chapter III. The new expansion velocity results in some of these PNe are highlighted. Spatio-kinematic models are presented for the PNe with a view to understand the observed velocity field, the intensity distribution, the observed morphology and the physical conditions in them in terms of viable physical mechanisms that have been proposed for the formation and structural development of PNe envelopes.

In Chapter V, a general mechanism for the formation and shaping of PNe envelopes is presented. The model shows how PNe of different morphologies can arise and also indicates the expected velocity fields in them. We compare the observed morphology and kinematics of the PNe covered in this study with the model and also with other proposed mechanisms for the shaping of PNe and thereby indicate the possible formation mechanisms for

the observed PNe.

In Chapter VI the important conclusions that have been reached from the present investigation are summarized and the scope for future work in this field is indicated.

A substantial part of the work presented here has been published as indicated in the list of publications. Specific references to these publications have not been made in the text.

LIST OF PUBLICATIONS

1. **D.P.K. Banerjee**, B.G. Anandarao, J.N. Desai, N.S. Jog, P.K. Kikani, R.K. Mahadkar, K.S.B. Manian, F.M. Pathan, N.C. Shah and M. Thomas, 1987, Astrophys. Space Sci., **139**, 327

   A high resolution Fabry-Pérot spectrometer for emission line studies in planetary nebulae and other extended astronomical objects

2. B.G. Anandarao and **D.P.K. Banerjee**, 1988, Astron. Astrophys., **202**, 215

   High resolution observations of the Planetary Nebulae NGC 6153 and IC 4593

3. B.G. Anandarao, **D.P.K. Banerjee**, J.N. Desai, S.K. Jain and D.C.V. Mallik, 1988, Mon. Not. R. astr. Soc. **235**, 221.

   Morphology of the bipolar planetary nebula NGC 2346 from emission line profile studies.

4. **D.P.K. Banerjee**, B.G. Anandarao, J.N. Desai, S.K. Jain and D.C.V. Mallik, 1989, IAU Symp. No. 131, "Planetary Nebulae", ed: S. Torres-Peimbert, Kluwer, Holland, p.187

   Evidence of expansion in the central region of NGC 2346.

5. **D.P.K. Banerjee** and B.G. Anandarao, to appear in the proceedings of the Symposium - "From Miras to Planetary Nebulae: which path for stellar evolution" - held in Montpellier, France (September, 1989).

   A kinematic model for the multiple shell planetary nebula NGC 1535.

6. **D.P.K. Banerjee**, B.G. Anandarao, S.K. Jain and D.C.V. Mallik, to appear in Astron. Astrophys., 1990

   Kinematic studies of five galactic planetary nebulae.

ACKNOWLEDGEMENTS

CHAPTER I
AN INTRODUCTION TO PLANETARY NEBULAE

1.1 Introduction:

A planetary nebula (PN, plural PNe) represents a transitory phase in the life of an intermediate mass star ($1 < M/M_\odot < 8$, where $M_\odot$ is the solar mass) as it evolves from the red giant to the white dwarf stage. The nebula, in essence, consists of a shell (or shells) of expanding, gaseous matter which has been ejected from the star during the course of its evolution on the asymptotic giant branch. The nebular matter is photo-ionized by the ultra-violet flux from the hot central star which have high temperatures in the range of 30,000 ^{0}K to 300,000 ^{0}K. The nebular spectrum displays the recombination lines of Hydrogen and Helium but is dominated by the strong forbidden lines from ionized species like Oxygen, Nitrogen, Neon and Sulphur. A wide range of morphologies is observed in PNe viz. spherical, ellipsoidal, bipolar, multiple shell and irregular shaped PNe. A typical planetary nebula has a radius of about 0.1 pc, an electron density between 10^3-10^4/cm^3 and an electron temperature of approximately 10000 ^{0}K. The nebular shells are found to expand with a typical velocity of $\sim$ 20 km/s.

Planetary nebulae form one of the most important sources for enriching the interstellar matter from which new stars take birth by the gravitational collapse of condensations. The study of how the mass loss takes place from the progenitors of PNe is therefore an important astrophysical problem. Furthermore,

1

planetary nebulae present a unique opportunity for studying certain physical phenomena which are difficult to investigate in a terrestrial laboratory viz. the study of forbidden transitions.

1.2 The early years of PNe studies:

PNe were known at the time of the French astronomer Charles Messier (1730-1817) who first compiled a catalogue of several nebulous objects in the sky. These nebulous objects included galaxies, diffuse nebulae and a few PNe. This "List of nuisances" (Aller, 1956) was compiled in order to aid the comet hunter. Subsequently Sir William Herschel (1738-1822) further extended this catalogue by discovering two thousand more "nebulae". Among these objects, however, Herschel recognized a class of objects different from the others which he named as planetary nebulae due to their resemblance with the disk like appearance of the planets. The first spectroscopic observation of a planetary nebula was made by William Huggins in 1864 - the object that was studied being NGC 6543 in the Draco constellation. His observations showed a single bright emission line in the visible spectrum. A year later using a spectroscope with a higher resolving power, Huggins again repeated his observations. The single bright line was this time resolved into three components. One of these lines could be identified with the Hydrogen Balmer β 4861Å line. The other two stronger lines could not however be identified at that time with any laboratory-produced line and were attributed to a mysterious element "nebulium". A parallel example exists for naming a "new element" in this manner. A line in the solar corona was originally attributed to a new element "coronium"

but was later identified to be due to iron in its thirteenth stage of ionization. The true identity of nebulium was estalished much later in 1927 by Bowen who showed that nebulium was none other than Oxygen and that the two bright lines at 4959Å and 5007Å arise from forbidden transitions of doubly ionized Oxygen.

With the advent of larger telescopes and more sophisticated instrumentation much progress has been made towards the understanding of PNe since Bowen's time. Today we know that PNe are an important part in the stellar evolution process.

1.3 The progenitor stars of PNe and their evolution:

Extensive studies by several authors suggest that most stars which begin their life on the main sequence with an intermediate mass between 1 to 8 $M_\odot$ pass through the planetary nebula stage and end up as white dwarfs (Iben and Truran, 1978; Renzini and Voli, 1981; Renzini, 1981; Iben, 1985). To illustrate the evolutionary history of different stars we show in Figs. 1.1 and 1.2, the model tracks on the HR diagram for a $5M_\odot$ star and for a representative sample of stars respectively as given in Iben (1985). In this section we discuss in particular the evolution of an intermediate mass star on the asymptotic giant branch (AGB) on which PNe are supposed to be formed. It may be mentioned that the asymptotic giant branch is distinct from the red giant branch (RGB). The RGB may be roughly defined as a narrow band of width $\Delta \log T_e \sim 0.1$ (T_e is the surface temperature of the star) on the HR diagram which extends nearly vertically upwards from an average $\log T_e \sim 3.65$ to an average $\log T_e \sim 3.45$ at the highest

LOG (L)

3.50
3.45
3.40
3.35
3.30
3.25
3.20
3.15
3.10
3.05
3.00
2.95
2.90
2.85
2.80

CORE NEUTRINO
LOSS,
THIN HELIUM
BURNING SHELL

THICK HELIUM
BURNING SHELL

13

MAJOR PHASE OF
CORE HELIUM BURNING
$(9 \times 10^6$ YR)

10'   10

12

10^6 YR

11

14

ESTABLISHMENT
OF SHELL SOURCE
$(1.4 \times 10^5$ YR)

HYDROGEN BURNING
IN THICK SHELL
$(12 \times 10^6$ YR)

OVERALL CONTRACTION
WITH EXHAUSTION OF
CENTRAL HELIUM

5

3   4

DISAPPEARANCE OF
DEEP CONVECTIVE
ENVELOPE,
RAPID CONTRACTION
$(10^6$ YR)

9

IGNITION OF TRIPLE-
ALPHA PROCESS

7

OVERALL
CONTRACTION
PHASE
2   $(2.2 \times 10^6$ YR)

FIRST PHASE OF
CORE HELIUM BURING
$(6 \times 10^6$ YR)

8

SHELL
NARROWING
PHASE
$(8 \times 10^5$ YR)

RED GIANT PHASE
$(5 \times 10^5$ YR)

HYDROGEN
BURNING
IN CORE
$(6.44 \times 10^7$ YR)

CONVECTIVE ENVELOPE
BEGINS TO EXTEND
INWARD RAPIDLY-
SURFACE ABUNDANCES
BEGIN TO CHANGE

6

1

4.3   4.2   4.1   4.0   3.9   3.8   3.7   3.6

LOG (T_e)

Fig.1.1:   Evolutionary tracks for a 5M$_\odot$ star on the HR diagram.
The different nuclear processes occuring in the star and their
time duration are indicated (from Iben (Jr), 1985).
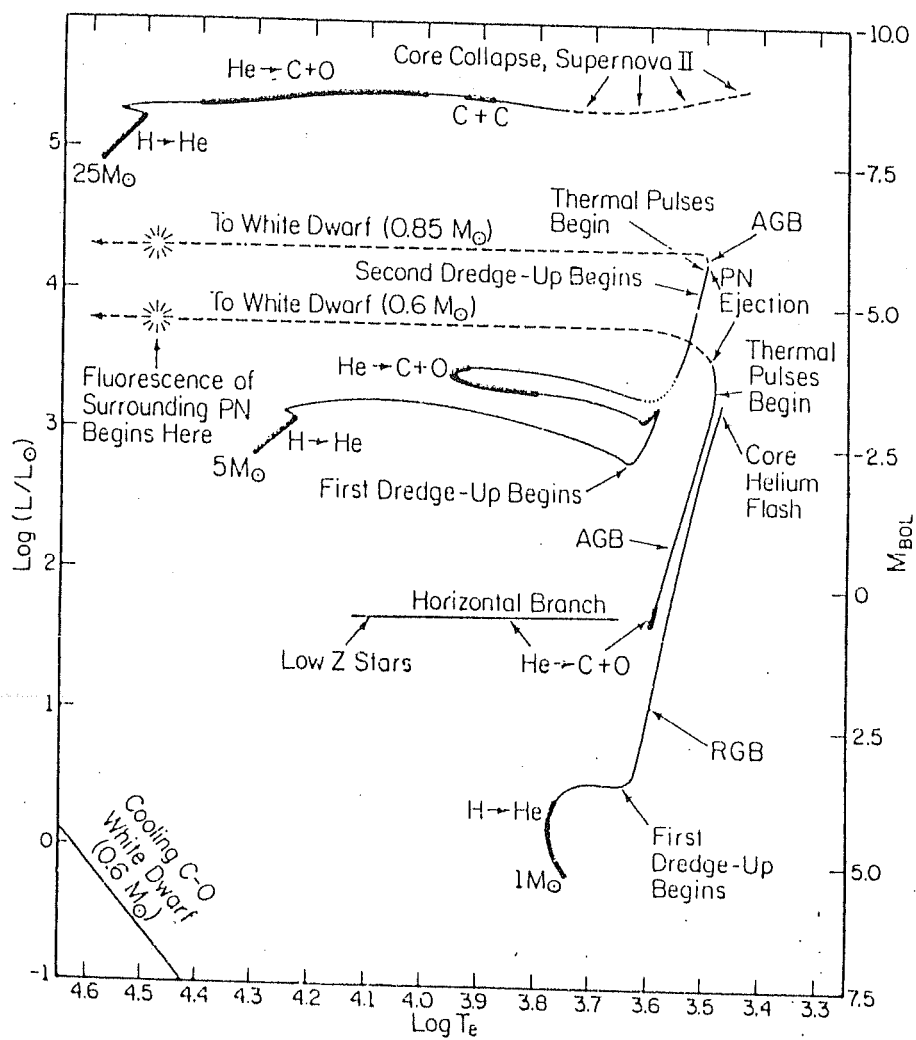
Fig.1.2: Evolutionary tracks in the HR diagram for a representative selection of stars (from Iben (Jr), 1985).

luminosities (Iben, 1981). The RGB phase is characterized by a Helium core surrounded by a Hydrogen burning shell. The ascent of the star up the red giant branch is terminated by the ignition of Helium in the core of the star and its subsequent conversion into Carbon via the triple alpha process. On the other hand the AGB phase represents a second ascent of the star on the HR diagram. This star in this phase is characterized by a Carbon-Oxygen core (formed after core helium exhaustion) in which the electrons are highly degenerate, surrounded by Helium and Hydrogen burning shells. The term AGB arises from the fact that the red giant branch in globular clusters actually consists of two branches that approach each other closely (or asymptotically) at high luminosities.

Nuclear burning in the Hydrogen and Helium shells during the AGB phase does not proceed steadily but rather in an off and on manner. For most of the time the principal source of almost all the energy escaping from the surface comes from the Hydrogen burning shell. As Hydrogen burning in the shell progresses; the mass of the Helium zone beneath it grows as a consequence of Hydrogen shell burning. When the temperature and density in the Helium shell reach a critical value, a runaway thermonuclear process occurs (called the Helium shell flash) with Helium being converted into Carbon by the triple alpha process. The rate of energy released in this process becomes larger than the rate at which it can radiatively diffuse outwards and as a consequence the temperature in the Helium burning zone increases sharply and the accompanying increase in pressure goes into expanding the matter in and around the burning zone. The expansion

and cooling of layers above the Helium burning zone is so large that nuclear burning in the Hydrogen shell is extinguished. Ultimately cooling of the Helium burning shell due to expansion terminates the thermonuclear runaway and Helium begins to burn quiescently.

Towards the end of the quiescent Helium burning phase, Hydrogen is again re-ignited and becomes the dominant source of energy that escapes from the star. The cycle described above then repeats itself and the star is at this stage said to be in a thermally pulsing phase. Although there appears to be considerable uncertainty as to the exact stage at which the PN shell is ejected, it is believed that the thermally pulsing AGB stage is terminated by the ejection of the PN shell. We discuss this aspect in a little more detail in the forthcoming sections where we discuss some of the different mechanisms that have been proposed for PN formation. While the intermediate mass stars end up ejecting a PN with the remnant core forming a white dwarf, the stars of masses $\geq 9M_\odot$ meet a different fate after their main sequence phase. It is believed that such heavy mass stars end on the AGB with a Carbon-Oxygen core mass greater than the critical Chandrasekhar mass of 1.4 $M_\odot$ and that in such stars Carbon is ignited in the Carbon-Oxygen core. A subsequent chain of nuclear reactions follows with heavier elements being synthesized successively until a central iron core is formed. The central core, which cannot undergo any further nuclear reactions and thus lacks nuclear fuel, collapses to form a neutron star or a blackhole and the envelope is blown off in a type II supernova explosion thereby terminating the life of such massive stars

(Renzini, 1981; Iben, 1985).

The evolutionary tracks of post-AGB stars (the nuclei of PNe) with different core masses have been studied by several authors (e.g., Paczynski, 1971; Harm and Schwarzschild, 1975; Schönberner, 1981, 1983; Schönberner and Weidemann, 1988). We show in Fig.1.3 a representative diagram of the post-AGB evolution of the central stars. A striking point in this figure is the position of the white dwarfs with respect to the position of the PNe nuclei on the HR diagram. They seem to clearly form an extension of the PNe evolutionary sequence and from this it may be inferred that the central stars of PNe finally evolve into white dwarfs. Further corroboration for this scheme of evolutionary sequence is seen in the observed formation ratio of PNe and white dwarfs i.e., 1.5×10^{-12} PNe pc^{-3} yr^{-1} as found in a region within 1 kpc of the Sun and 1.5×10^{-12} white dwarfs pc^{-3} yr^{-1} as found in a region of 100 pc around the Sun (Pottasch 1984).

1.4 Temperature of the central stars of PNe:

We have discussed in the previous section the evolution of the central stars of PNe and indicated their position on the HR diagram in Fig. 1.3. It is relevant to see how the temperature of the central stars of PNe are measured so that their location on the HR diagram can be determined. We describe here one of the methods for determining the central star temperature of a PN as proposed by Zanstra (1931). Zanstra himself referred to it as a "cheap way to do space research". The principle of the method is elegant and quite straightforward. If the nebula is optically thick to the Lyman continuum radiation from the central star then
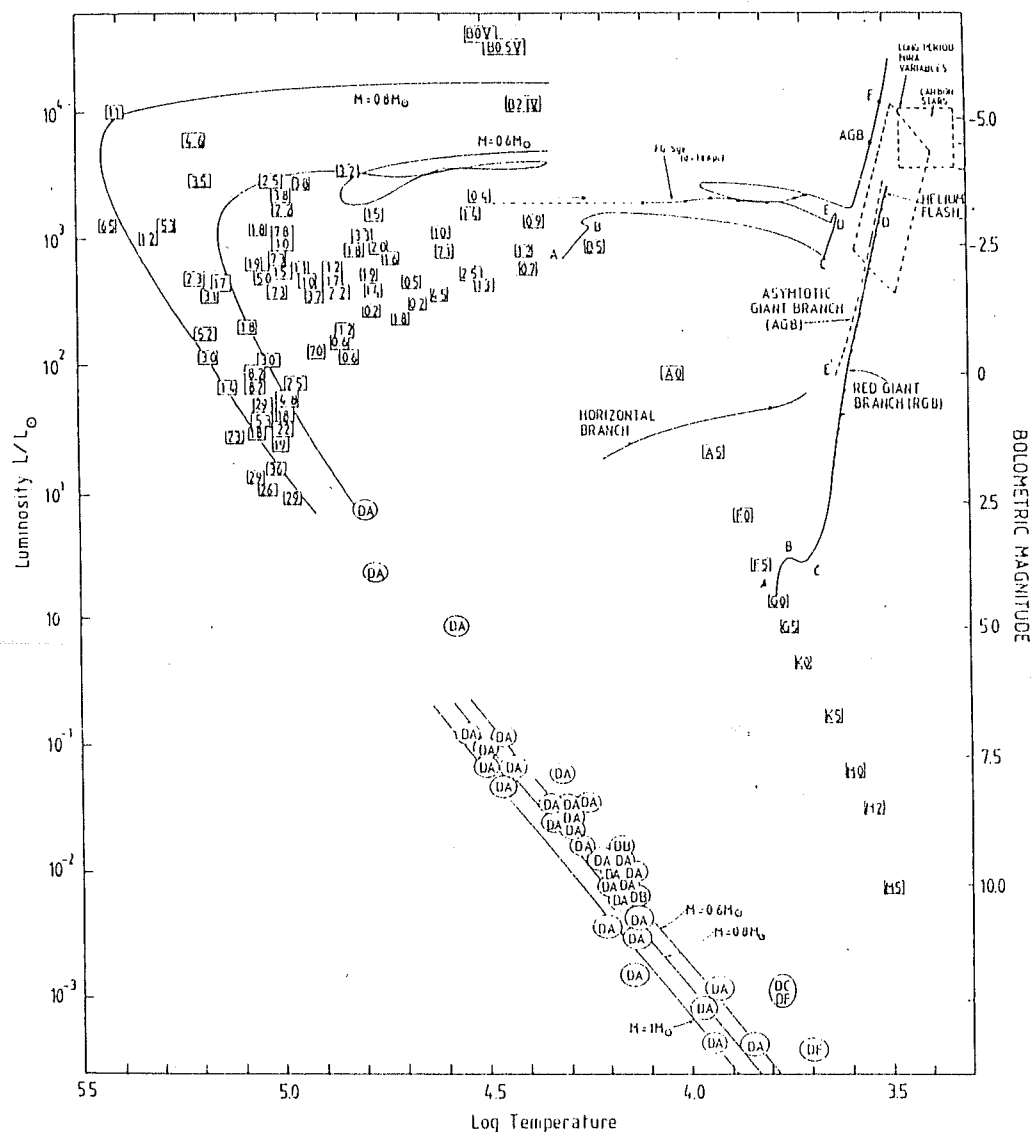
Fig.1.3:   The   top   right   hand   side   of   the   figure   shows   the
theoretical   evolution   of   two   stars   of   masses $1.1M_\odot$ and $5M_\odot$
respectively.   The   post-AGB   evolutionary   tracks   of   two   completely
degenerate   stars   of   core   mass $0.6M_\odot$ and $0.8M_\odot$ respectively   are
also   shown.   For   orientation,   the   main   sequence   stars   (spectral
class   indicated   in   squares),   the   position   of   the   central   stars   of
PNe   (their   estimated   ages   in   units   of 10^3 years   indicated   in
squares)   and   the   white   dwarfs   (marked   in   brackets   by   DA,   DB,   DC
and   DF)   are   also   shown.(From   Pottasch,   1984).

each photon will create an ionized Hydrogen atom. After a certain time the electron ejected by photo-ionization will be recaptured by the Hydrogen ion. Zanstra showed that every such recombination should necessarily result in the emission of one Lyman α and one Balmer series photon apart from other quanta which may be emitted. The Balmer photons escape from the nebula which is optically thin at these wavelengths. Thus by measuring the total number of Balmer quanta emitted, the total number of ionizing photons in the Lyman continuum of the central star can be obtained. In practice it is necessary to measure the Balmer flux in only one line (Hβ is usually used) since the ratio of this line to the total Balmer emission can be predicted. This ratio depends weakly on the nebular temperature which can be sufficiently well determined.

Next the number of photons emitted by the star at some particular wavelength in the visual region is determined by observations. Once this is done, the central star temperature may be determined by comparing the observed visual and estimated ultraviolet fluxes (after making the necessary corrections for the extinction) with that predicted for a black-body (here it is assumed that the radiation from the central star has a black-body distribution). In essence therefore, "a long base-line colour index of the star between the Lyman ultraviolet region and an ordinary optical region" (Osterbrock, 1974) is being constructed from which the temperature of the star may be determined. Temperatures derived in the above manner are called Zanstra Hydrogen temperatures. In a similar manner a Zanstra Helium temperature may be determined by calculating the ionizing flux for Helium atoms (i.e., photons with wavelength shortward of 228Å). In

this case the intensity of the HeII line at 4686Å is used (corresponding to the transition from n = 4 to n = 3) to determine the ionizing flux.

1.5 Mechanisms of PNe formation :

The evolution of an intermediate mass star along the AGB is accompanied by a process of mass loss from its outer envelopes leading thereby to the formation of a PN. Different mechanisms have been proposed for the cause of the mass loss, the rate of the mass loss and the stage at which it occurs thereby leading to different scenarios for PNe formation. Overall it may not be wrong to say that the method of PNe formation is not too well understood and that a general concensus in this direction has not been reached. We discuss in this section some of the important mechanisms that have been proposed for PNe formation.

1.5.1 PNe formation due to Dynamical and Pulsational Instabilities:

Extensive studies have been made of the properties of AGB star envelopes to determine whether sudden mass loss can occur from such envelopes due to dynamical instability thereby leading to the formation of PN shells (Roxburgh 1967, Paczynski and Ziolkowsky 1968, Keeley 1970, Smith and Rose 1972, Wood 1974, Tuchman, Sack and Barkat 1978). For example, Tuchman, Sack and Barkat (1978) have found that the onset of dynamical instabilities can lead to PNe shell ejection. However, this mechanism suffers from the drawback (as pointed out in a subsequent paper by Tuchman, Sack and Barkat, 1979) that when stability has been

11

re-established, the remaining envelope mass of the central star is too high ($\geq 0.1 M_\odot$) compared to the normally believed values of 10^{-3} $M_\odot$. To remove the above inconsistency they have therefore considered whether PNe can arise from mass loss earlier (at lower luminosities) in the life of the star. The mechanism for mass loss in this case is due to the onset of pulsational instabilities in the stellar envelope when the star occupies that part of the HR diagram which is populated by Mira variables. Tuchman, Sack and Barkat (1979) find that there exists a critical luminosity $l_p(m)$ beyond which pulsations of a Mira variable are no longer stable and mass loss occurs. This critical luminosity is dependent on the mass of the star and can be approximated by the linear relation

$$l_p(m)/l_\odot \quad = 8280 \; (M/M_\odot) - 4680 \tag{1.1}$$

The above authors find that the onset of pulsational instabilities leads to approximately 3% of the envelope mass being ejected semi-regularly every 25-30 years. The entire shell is ejected in about 900 years leaving behind a central star with an envelope mass consistent with PNe nuclei. Further the velocity of the ejected matter is always close to the relevant escape velocity. The presence of thermal pulses or double shell flashes (described in section 1.3), which occur at around the same luminosity range as do the pulsational instabilities, may lead to further developments viz. the formation of multiple shell PNe. It is not yet clear whether or not such double shell flashes would lead to the the formation of bipolar PNe.

1.5.2 The interacting winds mechanism for PNe formation :

The interacting-winds mechanism is an alternative model for PNe formation. In the two wind mechanism proposed by Kwok, Purton and Fitzgerald (1978) it is postulated that mass loss along the AGB occurs through a slow dense wind and that this mass loss continues till the hot core of the star is exposed. At this stage a second fast tenuous wind is initiated which snow-ploughs into the AGB wind and sweeps up the matter. Thus a high density shell is formed at the interface of the two winds over a period of several thousand years.

The mass loss rates that have been considered by Kwok, Purton and Fitzgerald (1978) for the AGB wind and fast wind are in the ranges 3×10^{-6} to 10^{-5} $M_{\odot}$/yr and 3×10^{-7} to 10^{-6} $M_{\odot}$/yr respectively. The wind velocities that have been considered are of the order of 5-10 km/s for the AGB wind and 500 to 1000 km/s for the fast wind. By adopting the above mentioned values for the different parameters, Kwok et al (1978) show that the PN shell formed by the interaction of the two winds will have similar observed characteristics of a PN viz. similar expansion velocities, electron densities and shell thicknesses.

It may be relevant to examine whether the AGB wind by itself can lead to a PN formation without invoking a fast wind. In this context the mass loss rate in the AGB wind is generally characterized by the Reimers formula (Reimers, 1978; Kudritzki and Reimers, 1978) viz.,

$$\dot{M} = -4 \times 10^{-13} \eta \ L/g \ R \quad (M_{\odot}/yr) \qquad (1.2)$$

13

where the luminosity L, the surface gravity g and the radius R of the star are in solar units and η is a parameter of the order of unity. Using the above formula, the maximum mass loss rates by AGB stars is found to be of the order of 10^{-6} $M_{\odot}$/yr (Renzini, 1981). Renzini (1981) has argued that such mass loss rates cannot lead to PNe formation for the following reason. Assuming a typical expansion velocity of ~ 20 km/s and radius ~ 0.1 pc for a PN, the age of a PN is found to be of the order of 10000 years. The mass loss during this period (for the above mass loss rate) is then found to be significantly smaller than the typical mass of PNe (~ 0.1 $M_{\odot}$).

Therefore to produce PNe with the observed characteristics, Renzini (1981) has proposed that the AGB phase must be terminated by a process of rapid mass loss i.e., by a superwind. He has also suggested that one of the causes for the superwind may be due to the onset of dynamical or pulsational instabilities in the extended envelopes of AGB stars as described in the previous section. Based on such a concept of a superwind, models have been constructed to study the formation and evolution of PNe. For example Schmidt-Voigt and Köppen (1987a,b) have constructed several numerical models to estimate the nebular parameters like electron density, nebular mass, expansion velocity etc. that would result from the interaction of three-winds viz., a slow AGB wind, a superwind and a fast tenuous wind. They find that the observed PN characteristics are best reproduced by considering a model in which the nebula is considered to be formed by a single sudden ejection (i.e., in about 1000 years) of matter by a superwind which "accretes" material from the AGB wind which the

star had blown off earlier (at mass loss rates of 10^{-6} to 10^{-5} $M_\odot$/yr).

1.6 The morphological forms of PNe:

The mechanisms described above, as such, seem to predict a spherical morphological form for PNe with an isotropic distribution of matter and expansion. However, the *vrai monde* is different, as it happens to be often. A great deal of variety in the structural form and shape is seen in the approximately 1500 galactic PNe that are known today. The gamut of observed morphologies span diverse shapes ranging from spherical, ellipsoidal, hour-glass (also known as bipolar or butterfly) to irregular shaped PNe. In addition, several PNe also exhibit multiple shell structure. Based on their morphology, several classification schemes have been proposed for PNe for example by Khromov and Kohoutek (1967), Gurzadyan (1970), Greig (1971) and Balick (1987). For instance, Balick (1987) has defined three broad morphological categories into which most PNe can be classified viz. round, elliptical and butterfly. Apart from these three main morphological archetypes, he has also proposed three other morphological forms viz. irregular, peculiar and amorphous.

Within the group of multiple shell PNe itself, further sub-classification schemes have been proposed (eg., Kaler, 1974; Chu, Jacoby and Arendt, 1987;). For example, based on their study of 41 known multiple shell PNe, Chu, Jacoby and Arendt (1987) find that there are essentially two kinds of morphologies : type I with faint, detached outer shells and type II with bright attached outer shells. The type II MSPNe have been further

15

subdivided into subclasses a, b, c and p. The definitions of these classes are reproduced from Chu, Jacoby and Arendt (1987) and are as follows: "a", a complete and uniform outer shell, e.g., IC 3568 and NGC 1535; "b", a complete outer shell with noticeable surface brightness variation, e.g, NGC 3242 and 7662; "c", an outer shell more developed in most directions but less pronounced in the poles, e.g., IC 289 and NGC 7354; and "p", a peculiar and irregular outer shell, sometimes filamentary, e.g., NGC 1514 and NGC 4361.

It may however be pointed out that classification schemes based on morphologies have to take into consideration a few other factors. One of these is that, due to the stratification of ionic species in PNe, the observed morphology will depend on the emission line chosen for procuring the image. Secondly, several PNe show considerable difference in their structural forms in images taken with different exposures. In addition the true morphology may differ from the observed morphology since a given geometrical form can map into another when viewed from different lines of sight. However, by taking into account all the above factors, it is seen that only a few intrinsically different shapes of PNe are observed. The common forms amongst these are the spherical, ellipsoidal, hour-glass and multiple shell PNe.

1.7 Mechanisms for the shaping of PNe envelopes :

A survey of the variety of morphological forms displayed by PNe culminates in a natural question as to why and how such diverse forms are produced especially if the ejection of the shell in all these PNe is assumed to originate from a common

mechanism. The presence of finer structures in PNe shells like filaments, knots etc. further add to the complexity of the observed morphologies of PNe. Though much progress has been made in understanding the origin of the diverse morphologies and the effective mechanisms that lie behind the structural development of PNe shells, there are still some problems that are not well understood. We discuss here, in general, some of the mechanisms proposed for the shaping of PNe.

One of the detailed models for the shaping of PNe based on a rapid/sudden mode of shell ejection, has been proposed by Phillips and Reay (1977). These authors have considered the effect of stellar rotation, gravitational braking and Lyman continuum radiation pressure on the shell development and dynamics. In the above model several morphologies are produced (spherical, ellipsoidal, toroidal) but not hour-glass structures. Further, Phillips and Reay (1977) have not considered the case of multiple shell PNe.

Based on the interacting two winds mechanism, several models have been proposed for explaining how the commonly observed forms of PNe viz. spherical, ellipsoidal and hour-glass arise (Kahn and West, 1985; Icke, 1988; Balick, Preston and Icke, 1989; Icke, Preston and Balick, 1989). The above models are hydrodynamical models which consider the different morphologies that should arise when a shock wave due to the fast stellar wind propagates into the surrounding AGB wind. In general, the above authors find that the important parameter which can give rise to the different morphologies is the "density contrast" in the AGB wind. The "density contrast" measures the ratio of the polar to

17

the equatorial density of the AGB wind which is assumed to be anisotropic. The physical mechanism for the creation of such a density contrast or anisotropy is still not well understood in the case of AGB stars, altough rotation is believed to effect such an anisotropy in rapidly rotating stars (Poe and Friend, 1986; Friend and Abbott, 1986). However, if such a density contrast does exist in the AGB wind, then different morphologies can result by the propagation of the subsequent fast wind into the former. Moderate and high density contrasts produce elliptical and hour-glass PNe respectively whereas the absence of a density contrast results in a spherical morphology.

The effect of a binary nuclei on the shaping of PNe envelopes has also been the subject of considerable investigation. For example, Bond and Livio (1990) have shown that mass loss from a close binary nuclei in a common envelope phase is concentrated in the orbital plane thereby creating a density contrast. This contrast, followed subsequently by a fast wind can then lead to ellipsoidal or hour-glass PNe as mentioned earlier. Similar studies, to see how the companion star effects the ejection of matter from the primary star, has also been carried out earlier by Morris (1981) and Kolesnik and Pilyugin (1986). Their work indicates that such binary systems can lead to the formation of bipolar PNe.

The above discussion summarizes the important models, factors and mechanisms that have been proposed for the shaping of PNe. Apart from these, however, the effect of magnetic fields on PNe morphology has also been considered by certain authors. Some examples of the work in this direction can be

obtained from the investigations of Woyk (1968), Gurzadyan (1970) and Bennett (1987). The work of the above authors show how it is possible to reproduce some of the morphological forms of PNe by invoking magnetic field effects.

1.8 The relevance of kinematic studies:

We have discussed in the preceding sections some of the important mechanisms that have been proposed for the formation and structural development of PNe envelopes of different morphologies. It is pertinent to ask now whether there are any observational tests that can be conducted to verify which of the mechanisms (acting either singly or together) is really responsible for the shaping of PNe. It is in this context that the kinematic studies of PNe can play a vital role.

The mechanisms that have been discussed for the shaping of PNe also predict the expected kinematics of the shell for different morphological types of PNe. It is therefore possible to compare the observed velocity field in a PN with predicted values and thereby test to a certain extent the validity of a proposed mechanism. Therefore kinematic studies can be used as a tool to verify different proposed mechanisms for the mode of shell ejection and also for the dynamical evolution and shaping of PNe envelopes.

From the velocity field studies of a PN it is also possible to get information on the three-dimensional structure of the nebula. An ordinary image of the object obtained for example by photography or CCD does not contain this three-dimensional information. In fact as mentioned earlier, the size and appearance

of a PN depends on the emission line in which it is being imaged since considerable stratification of ionic species occurs in PNe. In general, highly ionized species like [NeV], [HeII], [OIII] are found in regions closer to the central star while the lower ionised forms like [NII], [SII], [OII] are found in the outer regions. Thus the velocity field obtained by studying a PN in different emission lines can give information on different regions of the nebula thereby giving a 3-D velocity structure of the object. Based on model calculations the velocity field associated with a particular morphology can also be predicted and this may then be checked with observations to infer the true morphology of the object.

Further, the profile of a particular emission line from a PN contains information about the kinematics of the emitting gas all along the line-of-sight. Thus by suitable modelling (as will be discussed in details in Chapter IV)it may be possible to recover from the line profile parameters such as the temperature of the nebular gas, the magnitude of the turbulence present and the dependence of expansion velocity and electron density on radial distance. Therefore kinematic studies can also yield information on the physical conditions within the nebula. However, it should be mentioned, that a certain degree of uncertainty exists in the uniqueness of such spatio-kinematic models.

1.9 Physical Processes in PNe :

In this section we describe some of the important physical processes occurring in PNe and their relevance in terms

of interpretation of observations. We describe here the nebular spectrum, the study of which yields much information regarding the physical conditions and properties of PNe (like nebular temperature, density, abundances, mass, central star temperatures, extinction towards the nebula etc.). We concentrate, in particular, on the emission line spectrum since the kinematic studies described in this thesis are carried out by obtaining the profiles of such emission lines. In this context, we also describe how the physical parameters like electron temperature and density are determined from the emission line spectrum, since these parameters are useful for the spatio-kinematic modelling of PNe.

As mentioned at the beginning of this chapter, the source of energy which enables PNe to radiate is the ultraviolet flux from the hot central star which photo-ionizes the nebular gas. Each photo-ionization leads to the creation of a photoelectron with a kinetic energy equal to the excess energy of the ionizing photon over the ionization potential of the ion under consideration. The liberated electrons can then partake in several processes. We first consider those processes which lead to the emission line spectrum observed in PNe.

1.9.1 The emission line spectrum of PNe :

The emission line spectrum in PNe can be broadly categorized into two classes viz. recombination lines and collisonally excited lines. The recombination lines arise due to the capture of an electron into an excited level of a positively charged ion. The captured electron then cascades downward through different energy levels. In this process the characteristic line

21

radiation corresponding to the transitions between the levels involved is emitted.

The forbidden lines on the other hand are caused by inelastic collisions between ions and free electrons which subsequently excite the former into meta-stable levels close to the ground configuration. Although downward transitions from such levels are forbidden under LS coupling since they violate the selection rules, there exists a finite probability for such transitions. For example in the case of the [OIII] ion the transition probability of the meta-stable level for the 5007Å line in 2.1×10^{-2}/sec (corresponding to a mean lifetime of 48 seconds) and 7.1×10^{-3} (mean lifetime 140 seconds) for the 4959Å line (Osterbrock 1974). It is relevant to ask why the forbidden lines of the ions in a typical PN spectrum are as strong as the Hydrogen recombination lines in spite of Hydrogen being several orders of magnitude more abundant than the ions involved. The reason for this is that the mean lifetime of a free electron before it undergoes recapture is $\sim$ 10 to 20 years whereas it loses energy in an inelastic collision with an ion (i.e., it collisionally excites the ion) approximately every two or three months (Bohm and Aller, 1947; Aller, 1956). The typical time scale of some of the other scattering processes may also be mentioned here. The free electron will dissipate its energy in free-free encounters (with other ions) in a matter of several weeks. But the process which occurs most frequently is electron-electron scattering in which free electrons exchange energy amongst themselves approximately every second. It is the short time scale of this process compared to other processes that tends to set up a Maxwellian distribution for

the electron velocities.

Another question that may be raised is why the permitted lines of ions caused by collisional excitation are not prominent in the visible nebular spectrum compared to the collisionally excited forbidden lines. In fact the average transition probability for the permitted lines are several orders of magnitude larger than the transition probabilities for the forbidden lines. The forbidden lines still dominate the spectrum for two reasons. First, the electron density in a typical PN is sufficiently low such that collisional de-excitation from the metastable levels (which give rise to the forbidden lines) is limited. Secondly, in general, the metastable levels of the involved ions, are separated from the ground level configuration by energy differences of the order of only a few kT (k is Boltzmann's constant and T is the electron temperature of the nebular gas). In Fig.1.4 we show for example the energy-level diagram for the [OIII] and [NII] ions. Electron energies of 2.5 and 1.89 ev are required in the case of [OIII] and [NII] respectively to collisionally raise the ions from their ground level configurations to the ^1D levels from which the prominent forbidden lines are formed (i.e., the [OIII] 4959, 5007Å and [NII] 6548, 6584Å lines). Such electron energies are readily available in a PN which is characterized by a typical electron temperature of $\sim 10^4$ ^oK (corresponding to a most probable kinetic energy of $\sim$ 1 ev). The permitted transitions, on the other hand, require higher energies thus making them more difficult to excite collisionally with the available electron energies.

Some of the other processes that lead to emission
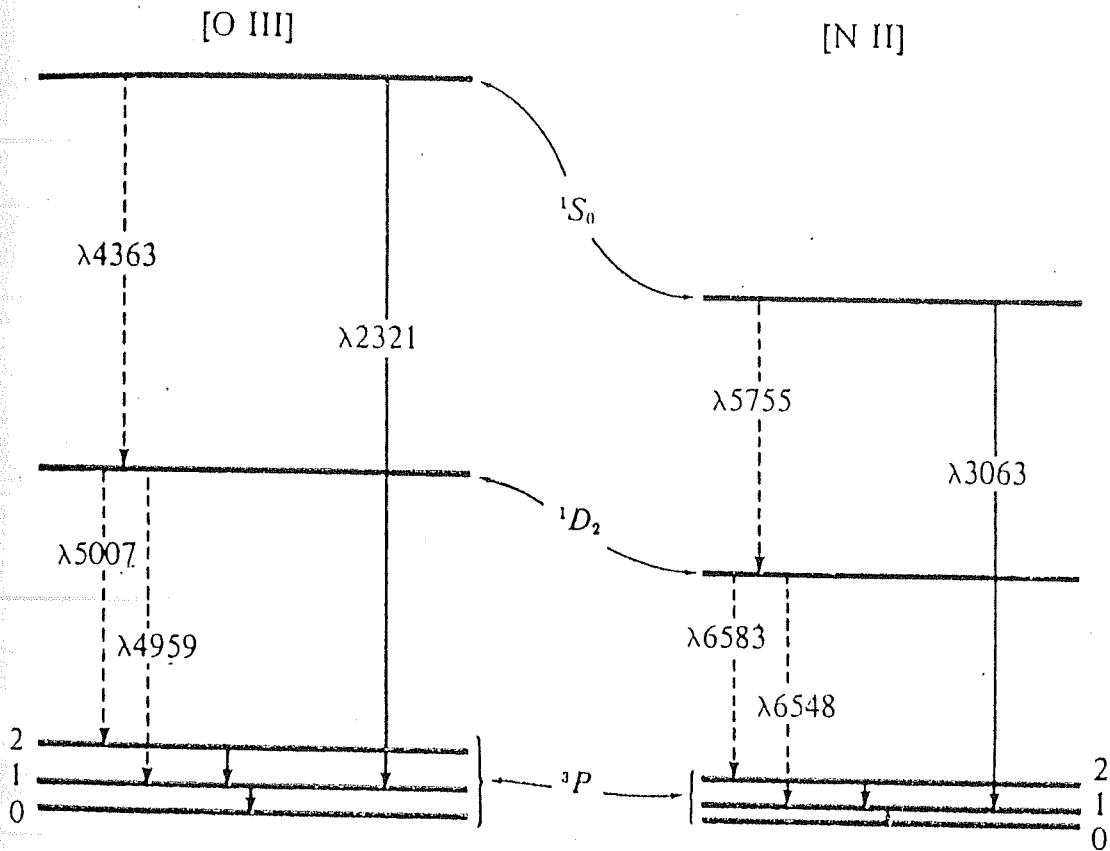
Fig.1.4: The energy level diagrams for the lowest terms of the [OIII] and [NII] ions in their ground $2p^2$ configuration. Emission lines in the optical region are indicated by the dashed lines and by solid lines for the ultraviolet. Only the strongest transitions have been shown (from Osterbrock, 1974).

line formation may be mentioned here without elaboration. These are line formation due to dielectronic recombination and recapture of electrons by ions leading to recombination lines. However, the strength of the lines due to these processes are considerably weaker than the collisionally excited lines. Finally in the case of the [OIII] ion there are a few lines near 3000Å which are formed by the Bowen resonance-fluorescence process.

1.9.2 The continuum radiation from PNe :

The continuum radiation observed in PNe occurs due to the following processes:

i)   Free-free emission or bremsstrahlung radiaion produced by the acceleration of an electron in the electic field of a positive ion. This radiation falls in the radio part of the spectrum and can be used independent of the emission line spectrum to determine nebular parameters like electron density and temperature.

ii)   Free-bound emission which occurs when a free electron is recaptured by ionized Hydrogen and Helium atoms. In each recapture the excess kinetic energy of the electron over the energy level to which it is captured is given off as a quantum of energy.

iii)   Two photon emission from Hydrogen and Helium wherein transitions from the metastable 2^2S levels of Hydrogen and Helium to lower levels can occur via a virtual level with two photons being emitted in the transition. The continuum radiation emitted by this process and also the one outlined in (ii) lies in the ultraviolet to the near infra-red region.

Apart from the above processes, the continuum radiation from the central star of the PN also contributes to the

25

observed nebular continuum.

1.9.3: Determination of electron temperature from emission lines:

Certain ions like [OIII] and [NII] have energy level configurations such that certain emission lines which occur in the visible region require significantly different excitation energies. Referring to Fig.1.4, it may be seen that the [OIII] 4363Å line occurs from the upper ^1S level while the 4959 and 5007Å lines occur from the lower ^1D level. Since the collisional excitation of the 4363Å line requires an electron energy of 5.3 ev whereas the other two lines require 2.5 ev (Aller 1947; Gurzadyan, 1970), it is clear that the relative rates of collisional excitation to ^1S and ^1D levels depend strongly on the temperature. Hence the relative intensities of the lines emitted in transitions from these levels can be used to measure the electron temperature. Similarly in the [NII] ion, the electron energies required to excite the ^1S and ^1D levels on 1.9 and 4.05 ev respectively. Based on a detailed analysis of the expected populations of the different levels under consideration and the subsequent relative strengths of the lines emitted by them, it may be shown that in the case of the [OIII] lines we have the relation (Osterbrock, 1974)

$$\frac{I\ (4959\ +\ 5007)}{I\ (4363)} = \frac{8.32\ \exp\left[\frac{3.29 \times\ 10^4}{T}\right]}{1\ +\ 4.5 \times 10^{-4}\ N_e/T^{1/2}} \qquad (1.3)$$

where T is the temperature, N_e is the electron density and I refers to the intensity of the line (wavelength of which is

indicated in brackets). A similar relation as eqn.1.3 holds for the intensity ratios of the [NII] 6548, 6584 and 5755Å lines. Some of the other relations for deriving the temperature from lines emitted by different ions species like [ArIII], [ClIV], [SIII], [NeIII] etc. can be found in Kaler (1976). Eqn. 1.3 or the corresponding equation for the [NII] lines can be used directly to evaluate the temperature if the nebula is assumed to be isothermal and to have sufficiently low electron density (Osterbrock, 1974). If collisional de-excitation is not completely negligible then even a rough estimate of the electron density substituted in eqn. 1.3 provides a good value of the temperature. In general however, the temperature is determined by plotting relations like eqn. 1.3 for different ions on an electron density versus temperature diagram and finding the common point through which all the curves pass or the common area which is bounded by the curves. More details on this aspect are given in Pottasch (1984).

1.9.4 Electron density measurements from emission lines:

The electron density in a PN may be obtained by studying the effect of collisional de-excitation on the intensity of certain emission lines. In principle, this can be done by comparing the intensities of two lines of the same ion which originate from levels requiring almost equal excitation energy. The relative excitation to these two levels will then depend on the ratio of the collision strengths. If the two levels have different transition probabilities or different de-excitation rates, the population of these two levels will depend on the electron density and subsequently the strength of the lines

emitted in transitions from these levels will also depend on the density. In PNe the lines which are generally used to measure the electron density are the 3726 and 3729Å lines of [OII] and the 6716 and 6731Å lines of [SII].

1.10 Aims and scope of this study:

We summarize the important aims and the scope of this study as follows:

(i) To observe the velocity fields in selected PNe and to construct spatio-kinematic models based on these observations. The aim of such models is to account for the observed velocity field, the intensity distribution and the observed morphology of a given/chosen nebula in terms of the physical mechanisms that have been proposed for the formation and structural evolution of PNe. To also determine from the observed data some of the physical parameters like temperature, turbulence etc. in the nebula.

In order to carry out the observations a high-resolution, piezo-scanning, Fabry-Pérot spectrometer suitable for the kinematic studies of PNe was designed and fabricated.

(ii) To formulate a general model to explain the structural development of PNe envelopes. The purpose of the model is to show how the commonly observed morphological forms of PNe may arise and to indicate the expected velocity fields in them. A need for such a general model exists since it appears that certain aspects of PNe related to either their morphology or kinematics may not be easily explained by the existing mechanisms for the formation and shaping of PNe shells.

the spectrometer and its advantages, principle of operation, design, fabrication, performance and finally the method of data reduction.

2.2 Choice of the spectrometer and its advantages:

The important advantage of the Fabry-Pérot spectrometer over other spectrometric devices like the grating or the prism is that it has a larger light gathering power (also known as throughput or "etendue") for the same spectral resolving power. The luminosity L of a spectroscopic instrument is defined as the ratio of the flux arriving at the detector to the monochromatic luminance of the source for the spectral element considered. It is given by (eg., Roessler, 1974)

$$L = \tau \, S \, \Omega \qquad (2.1)$$

where τ is the transmission factor, S is the area of the dispersing element of the spectrometer and Ω is the solid angle of light on the dispersing element. The quanity $S \, \Omega$ is the etendue of the instrument. Jacquinot (1954) has shown that for a particular spectroscopic instrument the product

$$LxR = constant \qquad (2.2)$$

when R is the resolving power of a spectrometer. Further, in a comparative study, he showed that the luminosity-resolution product of a F.P. spectrometer is much higher than some other devices :

(LxR) FP ~ 30 to 100 (LxR) grating ~ 300 to 1500 (LxR) prism

Compared to the Michelson interferometer, the F.P.S has the same LxR product. The gain or advantage (called Jacquinot advantage) that the Fabry-Pérot spectrometer has over a grating or prism spectrometer arises because, for the same resolution, the F.P.S can accept light from a much larger solid angle than these two instruments. This can reduce substantially the observing time needed for a required signal-to-noise ratio. The above luminosity advantage can be really beneficial when working on faint objects like PNe and on a relatively small (1m) telescope. The other advantages of the F.P.S are its simplicity of operation and its efficiency i.e., the transmission can be high (Ring, 1978).

2.3 Basic theory and definitions:

The basic theory and working of the Fabry-Pérot interferometer is dealt with extensively in several books (for eg., Born and Wolf, 1965; Thorne, 1974; Hernandez, 1986). In this section therefore we only present some of the salient features of the Fabry-Pérot (F.P) interferometer which are necessary and relevant to our work. The ideal F.P interferometer consists essentially of a pair of flat optical plates, the inner surfaces of which are coated for high reflection and low absorption. The plates which are spaced a certain distance apart are maintained parallel to each other. A monochromatic ray of light from an extended source incident on the assembly undergoes multiple reflection in the gap between the plates. The resultant transmitted beam therefore consists of a series of successively parallel rays with a constant path difference between them. These

rays may be allowed to undergo interference by focussing them at a point by means of a camera lens. The intensity distribution that is then observed is given by the Airy function viz.,

$$I = I_0 \left[\frac{T}{1-R}\right]^2 \frac{1}{1 + [4R/(1-R)^2]\sin^2(2\pi\mu\sigma t\cos\theta)} \qquad (2.3)$$

where I_0 is the intensity of the incident beam, T and R are the transmittivity and reflectivity of the coatings of the plate, μ is the refractive index of the material between the plates (which is assumed to be equal to 1 for air), θ is the angle of incidence, t is the inter plate separation and $\sigma = 1/\lambda$ is the wave number of the incident light.

As may be seen from eqn.2.3 the maxima of the Airy distribution occurs whenever

$$2 \mu \sigma t \cos\theta = n \qquad (2.4)$$

where n is an integer called the order number. For fixed n, t and θ the transmitted light consists of a series of sharp peaks separated in wave number by an important parameter called the free spectral range (F.S.R). The F.S.R at a particular wave number σ measures the spectral interval over which overlapping of orders does not take place and is given by

$$\Delta\sigma = F.S.R. = 1 / 2t \qquad (2.5)$$

In terms of the wave length the F.S.R is equal to $\lambda^2/2t$. The instrument function of the F.P. interferometer is represented

by the FWHM (full width at half maximum) of a fringe $\delta\sigma$. This quantity $\delta\sigma$ is a measure of the resolving power of the instrument and for a high reflectivity (i.e., sharp fringes) can be shown (from eqn. 2.3) to be given by

$$\delta\sigma = \frac{(1-R)\Delta\sigma}{\pi\sqrt{R}} \qquad (2.6)$$

The ratio of the F.S.R. to the half value width measures an important quantity called the coefficient of finesse (F). From eqn. 2.6 we have

$$F = \frac{\Delta\sigma}{\delta\sigma} = \frac{\pi\sqrt{R}}{1-R} \qquad (2.7)$$

The spectral resolving power of the instrument can be obtained by considering the intensity distribution of the superposed profiles of two equally intense lines separated by $\delta\sigma$. The resultant superposed profile shows at the dip, an intensity of 83 % compared to the value of 81% required by the application of Rayleigh's criterion. Therefore, considering that $\delta\sigma$ gives the limit of resolution we have from eqns. 2.4, 2.5 and 2.7

$$\text{Resolving power (R.P)} = \sigma/\delta\sigma = (\sigma/\Delta\sigma)F = nF \qquad (2.8)$$

The expression above however refers to a theoretical resolving power. In actual practice the instrument function of the F.P. is broadened as a result of convolution of several independent line broadening functions (Chabbal, 1958). The broadening factors are (a) plate defects including plate curvature

and microtopographical polishing errors (b) departure from strict parallelism of plates and (c) broadening due to a finite aperture size. The analytical forms of the various broadening functions are described in Chabbal (1958), Hernandez (1966,1970,1974, 1986) and have been summarised in Desai (1984). These are as follows:

(i) Broadening due to reflectivity being <100% and characterised by the associated reflective finesse $N_R = \pi\sqrt{R} / (1-R)$

(ii) Broadening associated with the plate curvature which is a rectangular function with associated finesse $N_C = \lambda/2x$, where x is the sagitta of curvature.

(iii) Broadening associated with microtopographic polishing errors (assumed to have a Gaussian distribution) which is a Gaussian function. The associated finesse coefficient is $N_G = \lambda/4.7y$, where y is the rms departure of the plate surface from an ideal plane.

(iv) Broadening associated with misalignment which is a cosine function with finesse coefficient $N_P = \lambda/\sqrt{3}z$, where z is the maximum departure of the plates from parallelism.

(v) Broadening due to a finite aparture which is a rectangular function with a coefficient of finesse $N_A = 2\pi/n\Omega$; where Ω is the solid angle subtended by the aperture(Jacquinot 1960; Atherton et al 1981).

The effective finesse N of the F.P system, assuming that all the above broadening factors can be approximated as gaussians is given by(Roessler, 1974)

$$N^{-2} = N_R^{-2} + N_D^{-2} + N_A^{-2} \qquad (2.9)$$

where N_D is the defect finesse arising from the plate defects (as outlined in points ii, iii and iv above). It is required to have $N_D \geq N_R$ to minimise loss of effeciency due to plate defects. This is realised in practice by polishing the plates to a flatness of $\lambda/100$ or more and also maintaining the parallelism to the same order. Such a degree of accuracy is easily available today with modern state-of-the-art equipiment.

Finally it may be pointed out that there are two main shortcomings of the Fabry- Pérot spectrometer which are its limited F.S.R and the rather broad wings of its instrument profile i.e., the Airy function. The Airy function has broader wings than the $(sinx/x)^2$ shape of the ideal grating which is itself worse than the $(sinx/x)$ instrument response of the Fourier Transform spectrometer (Ring, 1978).

2.4 Design and fabrication:

We show in Fig 2.1 a schematic diagram of the optical layout of the Fabry-Pérot spectrometer that has been constructed and used for the observation of planetary nebulae. In Fig 2.2 we show the data acquisition system of the FP spectrometer. The rationale behind the design and choice of various instrument parameters is described below.

2.4.1 Choice of etalon parameters:

The present work was aimed at investigating the kinematics of PNe by studying the more intense emission lines like

OPTICAL LAY-OUT OF FABRY-PEROT SPECTROMETER
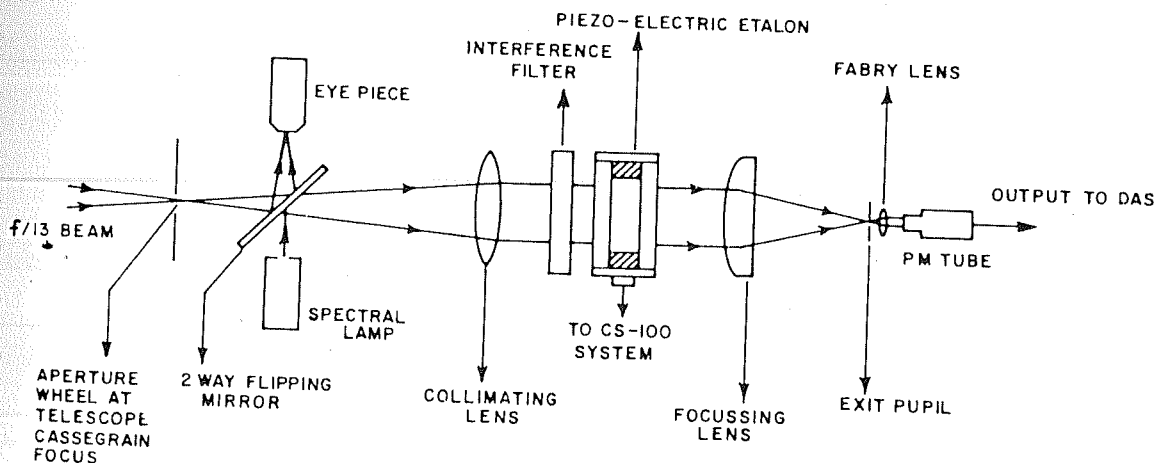
Fig.2.1:   A   schematic   diagram   of   the   optical   layout   of   the piezo-electric scanning Fabry-Pérot spectrometer.

SCHEMATIC LAY-OUT OF DATA—ACQUISITION SYSTEM
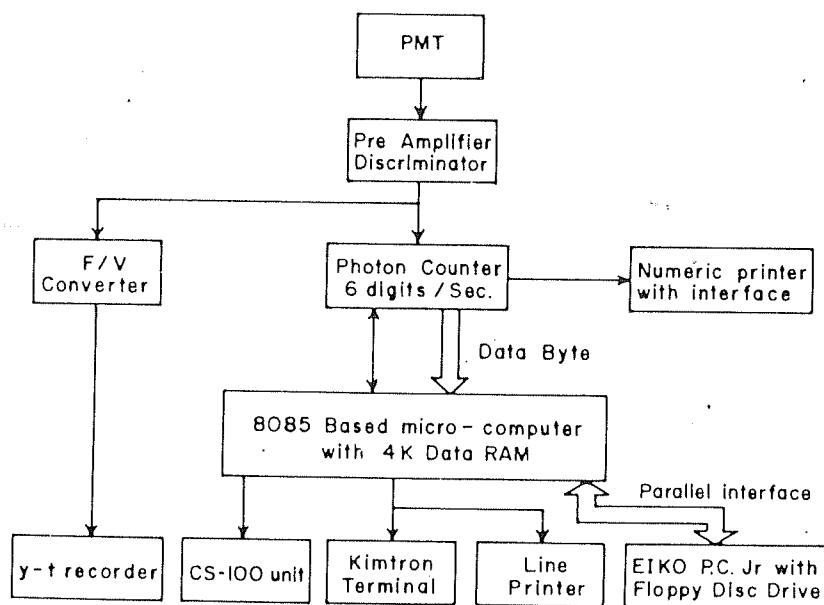
Fig.2.2:   A schematic layout of the data acquisition system used with the Fabry-Pérot spectrometer.

[OIII] 5007Å, Hα 6563Å and [NII] 6548,6584Å lines. The etalon characteristics have therefore been chosen keeping in mind the typical characteristics of these emission lines as found in PNe. For the [OIII] 5007Å line, the typical line width in PNe seldom exceeds 2Å which corresponds to an expansion velocity of 120 km/s. Hence an F.S.R of 3Å (at 5000Å) in the green region was chosen which adequately covers the line profile. In the red region the Hα 6563Å line shows a broader profile due to larger thermal broadening and hence an etalon with an F.S.R of 4.34Å (at 6563Å) was chosen. For the choice of the above values of the free spectral range the second etalon parameter to be decided is the effective finesse or the resolving power of the etalons. The etalon parameters like reflectivity, plate flatness etc were chosen such that an effective finesse of 20 could be expected. Since in general the expansion velocities (V_{exp}) in PNe do not fall below 4-5 km/s in any of the above lines; an etalon with a finesse of 20 (corresponding to a resolving power of 3×10^4) would be adequately able to resolve expansion velocities and fine structures in the lines.

Since the spectral coverage of a single etalon is usually not more than 1000Å, two etalons were used separately for the spectral ranges 4500-5500 Å and 5500-6700Å respectively. Both the etalons maintain a high reflectivity over a large band-spread (90-95% over a range of ~ 1000Å), so that a high resolution is obtained over a large spectral range. The parameters which characterize the two etalons used are listed in Table 2.1.

Table 2.1
Etalon characteristics

Characteristic	Etalon 1	Etalon 2
Type	Piezoelectric	Piezoelectric
Spectral range	(4500-5500Å)	(5500—6700Å)
Usable aperture	50 mm	85mm
Plate flatness	$\lambda/100$	$\lambda/100$
Plate separation	416 μm	496 μm
Peak reflectivity	93% at 5000Å	93% at 6563Å

2.4.2 Optical system:

The optical layout of the F.P.S is shown in Fig.2.1. As can be seen from the diagram an aperture wheel at the f/13 Cassegrain focus of the telescope provides the required field of view. The aperture wheel is of a rotatable kind with different aperture settings which can be varied from a minimum of 8" to 155" with intermediate values of 15",30",45",60" and 80". However it must be noted that in order not to degrade the resolving power of the instrument a choice of aperture should not be made which exceeds the acceptance angle of the spectrometer. The acceptance angle Ω_A of the instrument in terms of the resolving power R.P is given by (Meaburn, 1976)

$$\Omega_A^2 = 8/R.P \qquad (2.10)$$

For a resolving power $= 3\times10^4$ (for the above F.P.S) the value of $\Omega_A = 56$ arc minutes. Since the ratio of the Cassegrain focal length of the 1-meter telescope (f/13) to the collimator focal length of the spectrometer is 50, the above value of Ω_A corresponds to a $67''$ field of view in the sky. This sets the limit for the maximum possible apperture that should be used. A flipping mirror follows after the aperture wheel. The mirror serves a dual purpose. It allows the image of the object at the focal plane to be viewed through the eyepiece and also enables the light from a spectral lamp to enter the spectrometer for calibration purpose. The f/13 beam from the telescope is then collimated and passed through the etalon after pre-filtering by an interference filter (details of which are given in Table 2.2). The fringe system formed by the etalon is then focussed by means of a camera lens on the plane of the exit aperture. A Fabry lens following the exit aperture images the lens on to the photocathode of the photomultiplier tube.

2.4.3 Interference filters:

Because of the rather small free spectral range of the F.P.S, an interference filter has to be used to isolate the desired emission line before the signal from the object falls on the etalon. The details of the various interference filters that were used are listed in Table 2.2.

Table 2.2

Filter characteristics

Type: Interference filters (Spectro Film Inc.)

Size: Circular, 2 inch diameter

Peak transmission wavelength/FWHM:

(1) 4861Å / 10Å at 23^0C	for	Hβ 4861Å
(2) 5010Å / 20Å at 23^0C	for	[OIII] 5007Å
(3) 6565Å / 5Å at 23^0C	for	Hα 6563Å
(4) 6586Å / 12Å at 23^0C	for	[NII] 6584Å
(5) 6714Å /7.5Å at 23^0C	for	[SII] 6717Å

Temperature coefficients of the filters: 0.15Å red shift/ ^{0}C

Peak transmission: 40-50% (for different filters)

2.4.4 Detection system:

An S-20 photomultiplier tube was used in the photon-counting mode as a detector. The photomultiplier is cooled in a housing containing solid carbon dioxide (dry ice). The low dark counts of the cooled detector enables the instrument to record signals from faint objects. The characteristics of the detector are given in Table 2.3

Table 2.3

PMT characteristics

Make	ITT FW130
Spectral response	S20
Photo cathode	Multi Alkali K, Na, Cs, Sb
Photo cathode dimension	2.5 mm (diameter)
Gain	10^8 (16 stage multiplier system)
Operating voltage	1300-2200 V (median voltage 1800 V)
Dark counts at 0^0C	5 counts per second

2.4.5 Scanning of the etalon:

Both the etalons used in the F.P.S are piezo-electrically tuned with an interactive servo-control system to ensure parallelism during scanning. Before the advent of capacitance micrometery as a means to control and monitor plate parallelism, Ramsay (1962, 1966) and Smeethe and James (1971) had developed servo-controlled interoferometers utilizing Brewster's fringes as auxilliary signals for servo-control. However the disadvantage of the above system is that it cannot be used for very faint sources. Jones and Richards (1973) developed capacitance micrometers which could detect mechanical displacements in the etalon plates of the order of picometers. Using the above technique of capacitance micrometry, Hicks, Reay and Scaddan (1974) developed a servo-controlled Fabry-Pérot interferometer which could with great accuracy determine and maintain the mean spacing and parallelism of the plates to an order of $\lambda/200$.

In the F.P.S developed for the present studies, both the etalons and the servo-control stabilization system (CS100) were procured from M/s Queensgate Instruments. The etalons are piezo-electrically tuned having three piezo-electric transducer stacks cemented between the plates giving a change in plate separation of $\sim \pm 2.0$ microns for a voltage range of ± 750 V (User's manual for CS100, Queensgate Instruments). Capacitance micrometers are also cemented between the etalon plates. Parallelism and spacing are sensed by these capacitance micrometers, deriving error signals which are fed to the CS100 servo stabilization system. The CS100 system reads the error signals sensed by the capacitance micrometers and feeds back the appropriate voltages for corrections to the piezo-electric actuators which determine the etalon spacing. Hence, the CS100 behaves as a closed-loop stabilization system which renders the etalon insensitive to mechanical shocks or vibrations. It maintains the parallelism and spacing of the etalon to an overall accuracy better than $\lambda/2000$ at 5000Å (Reay, Hicks and Atherton 1984; User's manual for CS100, Queensgate Instruments). Scanning of the etalon in wavelength is done by using control logic which provides a sequence of numbers which vary the plate spacing by the requisite amount. The sequence of numbers may be provided in such a way as to increase the spacing in increments of 1, 2, 4, 8, or 16 steps. The choice of the increment lies with the user and depends on the requirement of the observation. Using a stepsize increment of 4 for changing plate separation one can scan 0.023Å per step at a wavelength of 5000Å and 0.025Å per step at 6563Å. The step-size chosen is a compromise between the scan duration

which should not be unduly long and the accuracy imposed by us for measuring the internal velocities in PNe which is $\leq$ 1 km/s. The number of orders to be scanned is also kept as an input parameter which may be varied as required by the user. As may be seen from eqn.2.4, a change in plate separation of $\lambda/2$ is required to scan one order.

2.4.6 Data acquisition:

A schematic block-diagram of the data acquisition system is given in Fig.2.2. Signal from the photomultiplier tube (PMT) in the form of pulses is amplified by a pulse amplifier and discriminator (PAD 101) and fed to a six digit counter (photon counter) which integrates the input count for 1 second. The 6 digit stored counts in the photon counter serve as the signal data which is displayed on the photon counter and also fed to the 8085 micro-processor-based computer board for storing as well as printing.

This micro-processor board controls and coordinates the operation of the instrument as follows:

(i) It initializes the system in the required variable parameters, viz., the stepsize increment required for the scan and also the numbers of orders to be scanned. These parameters are fed through the terminal before the beginning of the scan.

(ii) After initialization it starts the process of scanning by feeding step-position information to the CS100 unit. After this it generates a time-delay period for the stabilization of the etalon in the new step-position. The micro-processor circuit then

initiates the photon counter to accumulate the photon counts for a period of one second. On completion of accumulation of the photon count data the micro-processor acquires the data along with the step number in its memory. This information is then sent to the printer and simultaneously displayed on the terminal.

(iii) On completion of the forward scan, the reverse scan starts with the same input parameters like stepsize etc, which were used for the forward scan and thus in the reverse scan the etalon traces back, in steps, to its starting position. The data in the reverse scan is acquired, displayed and printed as before. On completion of forward and reverse scans the total data acquired in the memory of the micro-processor board is transferred enblock to a personal computer (PC) to store in a floppy disc for later processing.

For an on-line graphical display the PAD-101 output is also fed to an F/V converter whose analog output is proportional to the input photon count rate. This analog output is fed to a chart recorder which is time synchronized with the scan and thus a graphical output of the scan is obtained. This serves the purpose of a quick look-up of the nature of the scan.

2.5 Instrument profile and performance :

The instrument profiles of the two etalons used in the F.P.S were obtained by using emission lines from spectral lamps. For the etalon operating in the 4500-5500Å range, The HeI 5015.7Å line from a helium spectral lamp was used. For the second etalon, the 6598.9Å line from a neon spectral lamp was used. Fig.2.3 shows three orders of the instrument profile obtained by using the neon

line. An analysis of a single order in Fig.2.3 shows that the effective finesse is ~ 20. The FWHM width of the profile is found to be 0.25Å. Since the intrinsic width of the spectral line is only about 6 to 30 mÅ (Thorne 1976) the broadening of the profile is purely instrumental.

As shown in section 2.3 the width of the instrument profile is caused by a convolution (denoted by the asterisk) of several broadening factors i.e.,

$$I = AF*DF*AP$$

where AF is the Airy function which depends on the reflectivity of the plates. DF is the defect function which is itself a convolution of several functions as discussed in section 2.3 and AP is the aperture function. It is possible to estimate the effective finesse of the instrument due to the convolution of all these factors by using the formulae for the different broadening factors outlined in the end of section 2.3. For a reflectivity R = 92.5% at 6598.9Å we find the reflective finesse N_R = 40. For the given $\lambda/100$ plate flatness, N_G is found to be ~ 21. Since the plate parallelism is maintained at $\lambda/2000$, the misalignment finesse is very large i.e., N_P = 1150. To evaluate N_C (finesse due to plate curvature) we note that since parallelism is maintained all over the usable aperture of the etalon, N_C may be approximated equal to N_P. The aperture finesse N_A is found to be ~ 48 by using $\Omega = 7.85\times10^{-5}$ steradians (the value of the solid angle subtended by the aperture in the F.P.S). Assuming a gaussian

THREE ORDERS OF THE INSTRUMENT PROFILE
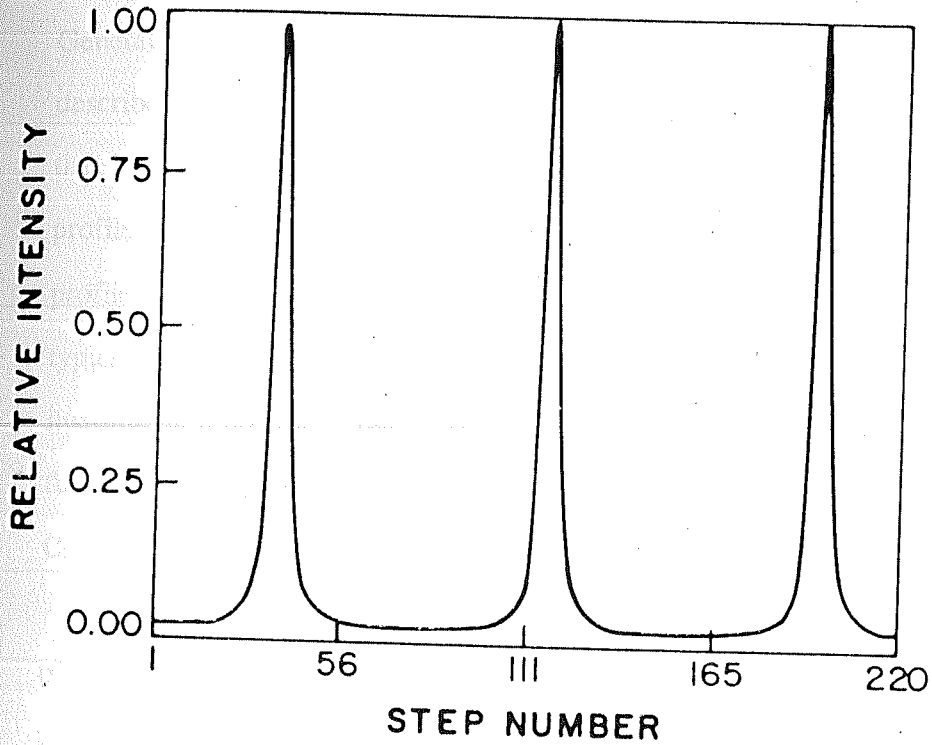
Fig.2.3:   Three   orders   of   the   instrument   profile   obtained   using
the 6598.9Å line   from   a   Neon   spectral   lamp.   Step-number   varies
linearly with etalon plate spacing i.e. wavelength.

form for all the broadening factors, we obtain from eqn. 2.9 an effective finesse N=18.0 which is in good agreement with the observed effective finesse of ~ 20 of the F.P.S.

In Figs. 2.4 and 2.5 we show an individual order of the instrument profile. The profile has been fitted by (i) a Gaussian of the same width and (ii) a Voigt profile of the same width which is obtained by convolving a Lorentzian function and a Gaussian. Generation of the Voigt profile has been done as per the method described in Van de Hulst and Reesinck (1947). It may be noted that a Voigt profile agrees reasonably well with the instrument profile. Also it may be seen, that except at the wings, a Gaussian profile also approximates well the instrument profile. Since typical PNe emission line profiles are much broader than the instrument profile, the latter may be assumed as a Gaussian function in deducing some nebular parameters as described in Chapter III.

In this context it is also instructive to see the effect of the circular aperture (which isolates the central fringe) on the resolving power of the instrument. As mentioned earlier the output of the F.P gets convolved with the band pass of the aperture which is a rectangular function to yield the final instrument profile. If the aperture isolates a width $\delta\sigma$ of the fringe then as shown by Roessler (1974) the resolving power is reduced to 0.7 times the theoretical value. In Fig. 2.6 we show the effect of different widths of the aperture on the resolving power. In the top left hand side of the figure we show the individual Airy profiles of the two equally intense lines (each of FWHM $\delta\sigma$)separated by $\delta\sigma$ (i.e., "just-resolved" lines) and also
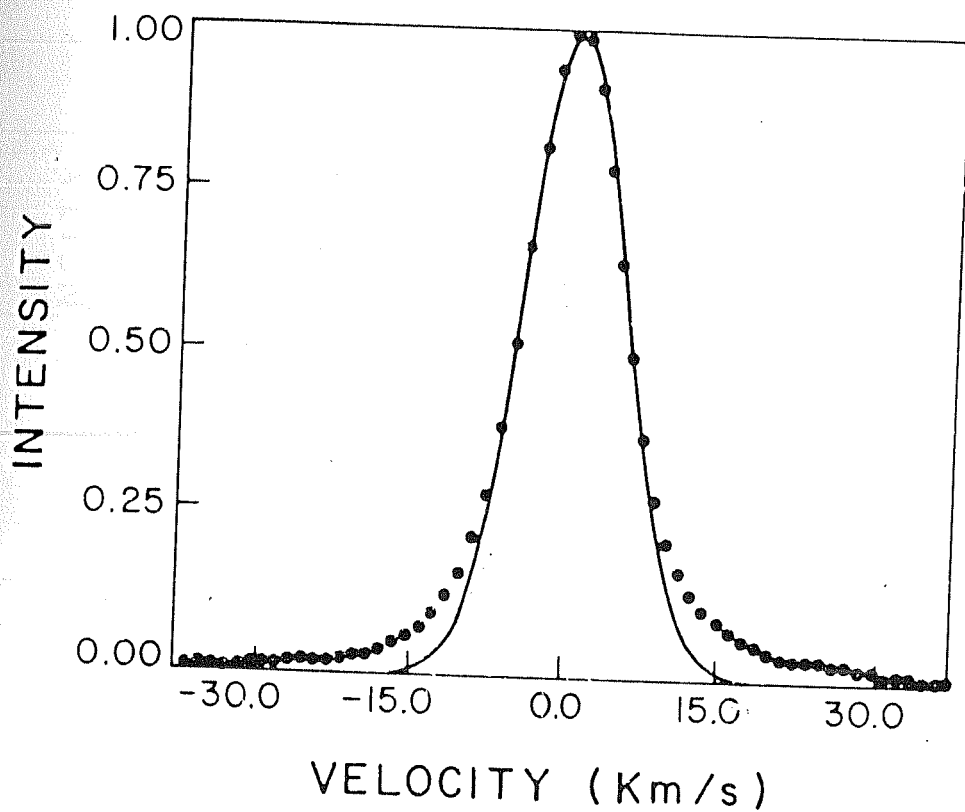
Fig.2.4:   One order of the instrument profile   in   the   6598.9Å   Neon
line fitted by a Gaussian of the same half-width.
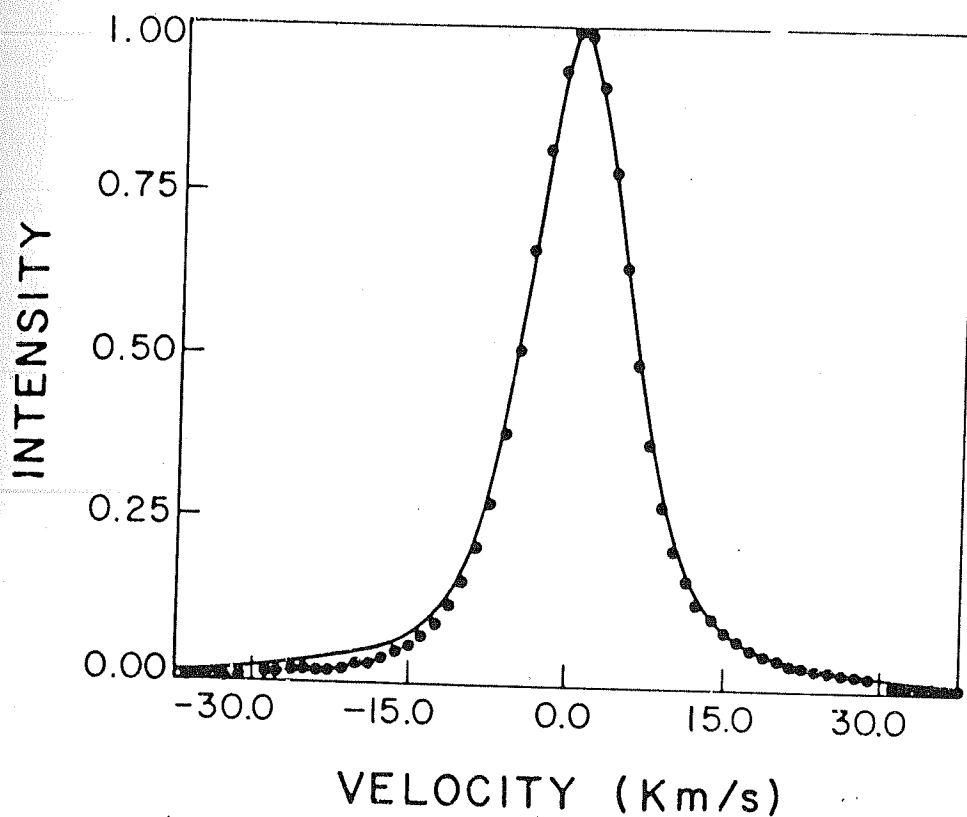
Fig.2.5: One order of the instrument profile in the 6598.9Å Neon line fitted by a Voigt function (obtained by convolving a Lorentzian function with a Gaussian) of the same half-width.

EFFECT OF APERTURE ON THE
RESOLVING POWER OF A F. P. SPECTROMETER
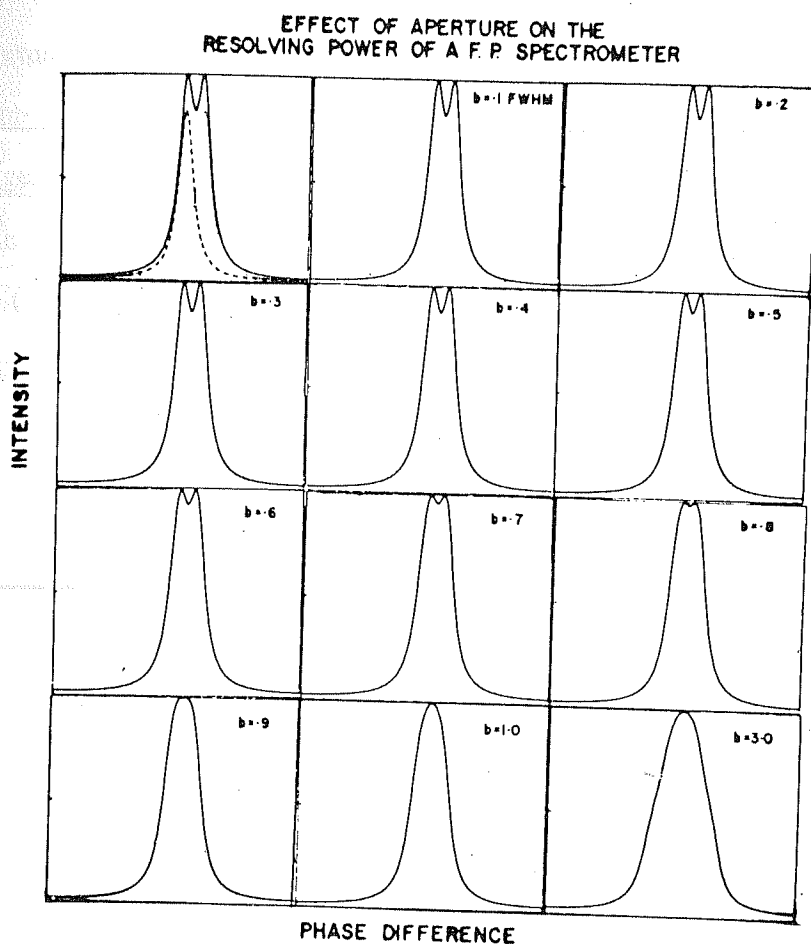
Fig.2.6: A study of the effect of increasing aperture size on the resolving power of a Fabry-Pérot spectrometer. The width of the aperture is indicated by "b" and is measured in terms of the FWHM of an individual Airy profile.

their superposed intensity profile. In the remaining diagrams of the figure we show the effect of sampling this "just-resolved" profile with an aperture of varying width (which is indicated by "b" and measured in terms of the FWHM $\delta\sigma$ of an individual Airy profile). The profiles are generated by convolving the rectangular aperture function with the Airy functions. As may be seen from the figure the dip to peak ratio of the profiles keeps increasing with bigger aperture i.e the resolution is decreased. The dip to peak ratio changes from 0.83 for the just resolved lines to 0.90 for b = $0.5\delta\sigma$. Another exercise was carried out by approximating the instrument function to a Gaussian profile and which yielded similar results. The above analysis throws some indirect light on the kind of aperture to use for the study of PNe kinematics. The PNe line profiles also show a double peak structure due to an expanding shell. If the expansion velocites expected are small and close to the resolution of the instrument, it is appropriate to use aperture widths small compared to the instrument half width provided the strength of the signal from the object permits it.

2.6 Observations and data collection:

The entire observations of the emission line profiles of planetary nebulae contained in this thesis were carried out at the Vainu Bappu observatory, Kavalur (latitude $+12^0$ $34'$ $35''$; longitude 78^0 $49'$ $45''$ E; altitude 2380ft above the mean sea level). The instrument was used at the Cassegrain focus of the 1m reflector. Data collection was done over a period spanning two years (1986-1988) and comprising of six observational campaigns in total.

2.7 Data analysis and reduction:

The generation of the emission line profile from the piezo-scanned F.P.S data is a fairly straight forward job. As mentioned in section 2.4.5 scanning of the etalon is done by changing the plate spacing in equal increments. A step number is assigned to each position of the plate spacing. The data stored on the line printer and on the PC is in the form of these step numbers versus photon counts per sec at each step. In order to calibrate the value of a step number in terms of wavelength, the number of steps (p) in one free spectral range of an emission line of a spectral lamp (of wavelength λ_c) is determined. The change in plate separation required to scan one order i.e., one F.S.R of a line of wavelength λ_c is given by $\Delta t = \lambda_c /2$ (from eqn. 2.4). Hence the change in plate separation per step $(\Delta t)_{ps}$ is given by

$$(\Delta t)_{ps} = \lambda_c /2p \qquad (2.11)$$

This value of the change in plate separation per step is also maintained while scanning an emission line from the object. Hence for an object line of wavelength λ_{pn}, the change in wavelength scanned per step $(\Delta \lambda)_{ps}$ can be obtained from the relation $\Delta\lambda/\lambda = \Delta t/t$ (see eqn. 2.4) as

$$(\Delta \lambda)_{ps} = \frac{\lambda_{pn} \lambda_c}{2pt} \qquad (2.12)$$

Since all the quantities on the right hand side of the above equation are known $(\Delta \lambda)_{ps}$ can be calculated. In terms of change in

53

velocity per step scanned, eqn.2.12 can be written using the Doppler relationship as

$$(\Delta V)_{ps} = c(\Delta\lambda)_{ps} / \lambda \qquad (2.13)$$

where c is the velocity of light.

Hence a line profile of intensity versus velocity can be generated to deduce further information on the kinematics. It may be pointed out here that in the case of a central-fringe scanning F.P.S, the absolute radial velocity of an object cannot be determined unambiguously. However this point is not of essence in deducing the expansion velocities or for the kinematic modelling of a PN wherein one either needs differences in radial velocities for a particular region of the nebula or the differences in radial velocities of different regions of the nebula with respect to each other.

2.8 Errors and their estimates :

Errors of basically two types can be identified. The first relates to errors connected with instrumentation and the second to errors introduced in the data processing. The details of these errors, their sources and estimates are discussed in the following sub-sections.

2.8.1 Stability of the F.P. etalons:

The capacitance micrometers cemented between the plates of the etalon sense variations in parallelism and departures from required plate spacing. These variations, as mentioned earlier,

are then corrected by the servo-control system CS100. However, unfortunately, capacitance variations are also brought about by changes in pressure, temperature and humidity which can change the dielectric constant of the air in the capacitor gaps. This may cause a drift of the instrument line profile with time. The stability of the etalons were therefore checked several times during each night's observations by taking calibration scans from a spectral lamp. The stability of the system can be estimated by the departure of the instrument profile peak from its original value. On an average during a scan of approximately 3 minutes duration, comprising of two orders and containing ~ 200 sampling points the maximum departure is found to be ~ 0.03 km/s in terms of velocity resolution. In fact for estimating expansion velocities only one order need be considered at a time. Hence the error introduced in expansion velocity determination will be half of the value quoted above. Thus dielectric constant variations in the capacitors do not introduce any significant error in expansion velocity measurements. However when the mapping of the velocity structure of the PN is done several scans have to be taken at different regions of the object. This process occupies approximately ≤ 2 hours time during which a comparatively larger drift of the profile peak may occur. A maximum departure of ~ 1 km/s for every two hour period of continuous observation is estimated. This error can be corrected since calibration scans were taken regularly between observations. Accordingly, this factor was taken into account when estimating the radial velocities of two different regions with respect to each other, the observations of each of which were separated in time. In

addition, as mentioned earlier in section 2.4.5, the stepsize chosen for scanning can introduce a maximum error of ≤ 1 km/s in the expansion velocity.

2.8.2 Errors in data reduction :

Smoothing of the data was done by taking a 2 to 9 point moving average. In general, since the signal-to-noise ratio was fairly good for most of the objects a 3 to 5 point moving average was found more than adequate for smoothing. This process of taking a moving average is in essence convolving the actual data with a rectangular function of width equal to the number of points in the moving average. Hence some broadening of the actual data should result. However since the widths of the observed data profiles are much larger than the width of the smoothing function, a very marginal broadening effect is noticed. The maximum change in width due to this process is estimated to be < 0.5 km/s. Further this process is not found to change the positions of the peaks of the profile in any significant manner and thereby it may be said that it does not affect the expansion velocity determinations. Estimation of expansion velocities from a smoothed pofile was done by fitting the profile by the appropriate number of gaussians (usually two) using a gaussian curve fitting routine (Anandarao and Rao, 1985). The above package is based on minimising the root mean square deviation between the fitting curve and the observed data points. The expansion velocity was obtained from the peak to peak separation of the individual guassians comprising the profile. The problem of fitting the observed line profiles with two or more gaussians, in general,

does not have a unique solution. Thus two separate fits to the same data may be made, with the gaussians comprising each of them varying slightly in their defining parameters i.e peak position and width. In this way we estimate that a maximum error of $\pm$ 1 km/s is possible in the widths and expansion velocities deduced from the gaussian decomposition of the profiles.

2.9 Pressure scanning F.P.S:

The early work on the study of the kinematics of PNe was initiated using a pressure scanning F.P.S. The instrument was largely the same one designed and fabricated by Sahu (1985) and described in details therein and also in Sahu, Desai and Jog (1984). Without embarking on details therefore, a brief summary of the instrument is given below.

In the pressure scanning F.P.S, scanning of a spectral line is achieved by changing the pressure within the cavity between the plates of the optically contacted etalon. This effectively changes the refractive index of the cavity medium which in the present case was freon gas. Thus as may be seen from eqn. 2.4 different spectral elements of the input signal are detected as the refractive index of the gas is changed. During operation, the pressure in the F.P. chamber is monitored accurately by a Digiquartz absolute pressure transducer which detects changes in pressure, again by capacitance micrometry. The output data is therefore obtained in terms of pressure and photon counts/sec. Conversion of pressure values in terms of wavelength is done in the following manner. First the change in refractive index due to change in pressure is related through $\delta\lambda$ α δP. The

proportionality constant in the last relation is easily found by measuring the change in pressure required to scan one free spectral range of the etalon - a quantity which is known. Thus the incremental change in wavelength due to an incremental change in pressure can be determined.

Some modifications and improvements were made to the instrument mentioned above. These included the fabrication of a near leak-free pressure chamber which houses the etalon, installation of a new stepper motor, construction of a new data acquisition system and other minor replacement of mechanical parts. With respect to the first point it may be noted that leakage of air into the F.P.chamber changes the refractive index of the gas and thereby introduces an error in the wavelength-pressure calibration scale used. This error may be minimised by ensuring that during a scan very marginal leakage takes place. However over a long period of time some leakage will take place and this may be corrected by taking regular calibration scans during observations using a spectral lamp. The new pressure chamber was found to be quite stable. Over a period of an hour of continuous scanning an average drift of ~ 1.0 km/s in terms of velocity resolution was noticed in the peak of the instrument profile. The mean error in the expansion velocity introduced by air leakage is found to be nominal (~ 0.1 km/s). In conclusion it may be said that the piezo-scanning F.P.S is a much more stable, accurate and easier-to-handle system than the pressure-scanning F.P.S.

CHAPTER III
KINEMATIC OBSERVATIONS OF SELECTED PLANETARY NEBULAE

3.1 Introduction :

In this chapter we present the details of the observations of the PNe that were studied and discuss the main results. All the objects chosen were restricted to galactic PNe with a total of ten PNe being covered in this study, viz: NGC 650/1, 1535, 2346, 2440, 2818, 5882, 6153, 6302, IC 4406, and IC 4593. It may be pointed out that on some of these objects the results are new. Most of the objects studied are known to exhibit bipolar morphology except NGC 1535, NGC 5882 and IC 4593. The reason for choosing a majority of the PNe to be bipolar is that the kinematic investigations of this class of objects are not very extensive and their formation mechanism is not very well understood. Hence, the detailed kinematic studies of these objects would be useful in providing clues to their formation mechanism.

In a few of the PNe studied, kinematic information could be obtained only in the central regions. In the other objects more extensive velocity mapping was carried out. It was originally intended at the commencement of this work to map extensively the velocity fields in a majority of the PNe under investigation. However this could not be fully realized due to vagaries of the weather, limited telescope time and non-availability of objects at different seasons of the year.

We first describe in this chapter the principle by

which kinematic information is extracted from the emission line profiles of PNe. Subsequently the observational details and the expansion velocity results are presented. A detailed discussion is then made of some of the PNe indicating the main results. Those PNe which have been studied more extensively through spatio-kinematic and morphological models are discussed in the subsequent chapter.

3.2 Kinematic information from PNe line profiles :

In general an emission line profile represents a plot of the intensity versus wavelength or velocity. In order to see, in principle, how kinematic information is extracted from an emission line profile we consider a simple case of a PN of spherical form. Then as may be seen, a line-of-sight through the nebula intercepts both the approaching and receding parts of the expanding shell of ionized gas. If the shell is expanding with a uniform velocity V_{exp} then an emission line emitted by the shell of ionized gas is split into two components due to the Doppler effect. The difference in wavelength between these two components is given by $\Delta\lambda = (V_{exp}/c)\lambda$ and can be measured spectroscopically. Thus one of the kinematic parameters that can be determined from a line profile is the expansion velocity.

However in a PN the realistic situation is more complex. For example the expansion velocity need not be constant across the shell but may change with radial distance from the star i.e., $V = V(r)$. Thus a line-of-sight traverses different portions of the shell moving with different velocities leading thereby to a broadening of the velocity profile. This information is latent in

the width of the components of the line profile and if it can be recovered by suitable modelling can give information on the variation of expansion velocity with radial distance. There are however, more important and dominant factors which broaden a profile and make the recovery of V(r) more complicated. These factors are (i) Thermal Doppler broadening of the line associated with the temperature of the nebular gas (ii) broadening due to a finite aperture being used to observe the nebula. Here the broadening is caused since several regions of the nebula expanding with different line-of-sight velocities are being viewed simultaneously through the aperture (iii) broadening due to turbulent motions in the gas and (iv) Instrument broadening of the profile as described in Chapter I.

Thus the observed profile is a convolution of several broadening factors and needs to be deconvolved to obtain kinematic information. The details of how this is done exactly is outlined and discussed in specific cases of PNe where emission line models have been constructed (for NGC 1535 and 5882 described in Chapter IV).

3.3 Observations of selected planetary nebulae:

In this section we present the observations made on the different PNe. The details of the observations have been summarized in Table 3.1

Although the table is largely self explanatory certain aspects need a little more elucidation. Column 2 of the table refers to the size of the observing aperture that was used in the central region of the nebula for the different emission

Table 3.1

Details of observations made on PNe

Sr. No.	Object	Aperture used in centre (arc sec)			Number of positions observed			SNR+ in the central region			Expansion velocity in central region (km/s)		
		[OIII]	Hα	[NII]	[OIII]	Hα	NII	[OIII]	Hα	NII	[OIII]	Hα	[NII]
1	NGC 650/1	30	-	-	3	-	-	8	-	-	8.0	-	-
2	NGC 1535	15	(refer text)		4	-	-	19	-	-	20.0	-	-
3	NGC 2346	15	30	30	2	1	1	5	5	7	8.0	10.0	11.0
4	NGC 2440	15	15	15	5	5	1	21	6	16	18.0	15.0	19.0
5	NGC 2818	60	45	45	1	1	1	5	5	8	23.0	25.0	28.0
6	NGC 5882	15	(refer text)		1	-	-	15	-	-	12.0*	-	-
7	NGC 6153	15	30	30	1	1	1	7	10	8	13.0	14.0	17.0
8	NGC 6302	-	-	30	-	-	1	-	-	25	-	-	-
9	IC 4406	45	-	-	1	-	-	10	-	-	5	-	12.0
10	IC 4593	8	15	15	1	1	1	6	10	6	17	22	44

+ SNR (signal to noise ratio) values indicated at the peak of a profile for a single scan.

* H-Beta observations also made of NGC 5882 give an expansion velocity of 13 km/s.

Table 3.1

Details of observations made on PNe

Sr. No.	Object	Aperture used in centre (arc sec) [OIII]	Hα	[NII]	Number of positions observed [OIII]	Hα	NII	SNR$^+$ in the central region [OIII]	Hα	NII	Expansion velocity in central region (km/s) [OIII]	Hα	[NII]
1	NGC 650/1	30	–	–	3	–	–	8	–	–	8.0	–	–
2	NGC 1535	15 (refer text)			4	–	–	19	–	–	20.0	–	–
3	NGC 2346	15	30	30	2	1	1	5	5	7	8.0	10.0	11.0
4	NGC 2440	15	15	15	5	5	1	21	6	16	18.0	15.0	19.0
5	NGC 2818	60	45	45	1	1	1	5	5	8	23.0	25.0	28.0
6	NGC 5882	15 (refer text)			1	–	–	15	–	–	12.0*	–	–
7	NGC 6153	15	30	30	1	1	1	7	10	8	13.0	14.0	17.0
8	NGC 6302	–	–	30	–	–	1	–	–	25	–	–	12.0
9	IC 4406	45	–	–	1	–	–	10	–	–	5	–	–
10	IC 4593	8	15	15	1	1	1	6	10	6	17	22	44

+ SNR (signal to noise ratio) values indicated at the peak of a profile for a single scan.

* H-Beta observations also made of NGC 5882 give an expansion velocity of 13 km/s.

lines. Sometimes a nebula has been studied in the same region with more than one aperture size (for eg. NGC 5882 and NGC 1535). In such cases a reference has been made to the text indicating that the details are given in the discussion of the individual PN. Further we have not indicated the aperture sizes used in different regions of the PN when the nebula has been studied in more than one region. These points are covered in the detailed discussion of individual PNe. Column 4 refers to the signal to noise ratio (SNR) obtained for the central region of the nebula for the different emission lines. The signal to noise ratio has been indicated for a single scan at the peak of the line profile and has been calculated using the relation (Dopita, 1972),

$$ SNR = \frac{N_s}{[\, N_s + N_d \,]^{1/2}} \tag{3.1} $$

where N_s and N_d are the source counts and dark counts respectively. In the table the SNR at different positions of the nebula, when it has been mapped in more than one position, has not been indicated. The last column gives the expansion velocities estimated for the different lines from the line profiles. In certain PNe however the line profile has shown a more complicated structure (refer IC 4593, NGC 2818, NGC 6153) than the typical double-peaked profile. In other cases no line splitting is observed (e.g. IC 4406). One is therefore referred, in general, to the discussion of the individual PNe as to how the expansion velocities have been estimated.

3.4 IC 4593:

IC 4593 [Perek and Kohoutek (1967, hereafter PK) number 25 +40^{0}1 ; R.A (1950) = 16^h 09^m 23^s ; Dec = 12^0 12$'$ 08$''$] is a compact planetary nebula with a radius of 6″ and a central star of spectral type O7f (Pottasch, 1984). Recent CCD imagery of the object by Chu, Jacoby and Arendt (1987) and Balick (1987) as reproduced in Fig. 3.1 shows, however, the existence of a fainter outer envelope of radius 21″ surrounding the inner nebula. The inner nebula itself seems to be a filled blob rather than a hollow shell. These authors have classified IC 4593 as a multiple shell nebula. Its internal motions have been studied through Coude spectrograph (dispersion 10Å/mm) by Wilson (1950). No lines were found by him to be resolved into components, the only trace of structure being in the [OII] 3726Å and 3728Å lines whose appearance consists of three blended components with the central one considerably the strongest. This has bearings on our observations as will be discussed at a later stage. Vityazev (1969) has quoted from Turoff (1965) an expansion velocity of 12.6 km/s for IC 4593. It appears that "Turoff used the Wilson (1950) and O'Dell (1962) data and determined the rate of expansion of thirteen nebulae from his statistical relations between the various parameters of nebulae and their nuclei". Welty (1983) has also studied this object using a 22″ aperture but has not found the line profile to be split clearly into components. He has therefore used the approximate relation that the full width at half maximum (FWHM) of a profile ~ 2V$_{exp}$ to deduce an expansion velocity of 12 km/s.
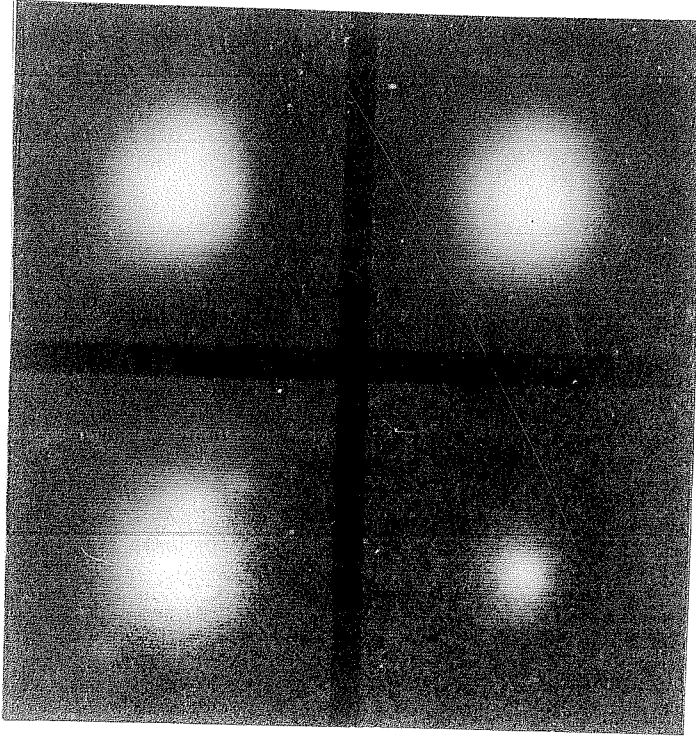
Fig.3.1: CCD images of the planetary nebula IC 4593 from Balick (1987). Starting from the top left hand corner and moving clockwise, the images have been obtained with filters centred on the Hα 6563Å, [OIII] 5007Å, HeII 4686Å and [NII] 6584Å lines.

It may be relevant to point out here how the relation FWHM ~ 2 V_{exp} is obtained. A consequence of using a finite aperture in the observations of line profiles from PNe is that the values of line splitting are found to decrease as the aperture increases. This effect is discussed by Bohuski and Smith (1974) who conclude that the expansion velocity measured from line-splitting obtained by using an aperture which subtends an angle greater than 25 percent of the nebular diameter should be taken as the lower limit of the expansion velocity. Using the Fabry-Pérot observations of Bohuski and Smith (1974) and also their own observations, Robinson, Reay and Atherton (1982) have constructed a model to estimate expansion velocities from observed line profiles where line-splitting is not clearly evident. In this model they find that the intrinsic FWHM of a profile i.e., the FWHM of a profile after it has been deconvolved for instrument and thermal broadening is given by

$$(FWHM)_{intrinsic} = 2V_R \left[1 + \delta/2 + \frac{(1-\alpha)\delta^2}{8} \right] \qquad (3.2)$$

where V_R is the expansion velocity, δ is the fractional thickness of the shell in terms of its radius and α is defined by assuming that the emissivity varies as $(radius)^{-\alpha}$. The above equation assumes a spherically symmetric nebula and is valid only for $\delta < 0.25$. Assuming a shell thickness within the above prescribed limit it is seen that eqn. 3.2 is fairly insensitive to the choice of α (i.e., whether $\alpha = 1,2,3$ etc) and that in general $(FWHM)_{intrinsic}$ is approximately equal to twice the expansion velocity. However in

66

the case of IC 4593 it is not clear apriori that the shell thickness is less than 0.25 times the radius. In fact the filling factor ε for this object is ~ 1.0 as calculated from the relationship given in Pottasch (1984, p.106) thereby indicating that it is almost a filled blob. In estimating ε, values of electron density = $1.7 \times 10^3 / cm^3$, angular radius = $6''$, log[f(Hβ)] = -10.55 (all from Pottasch, 1984), distance = 3.4 Kpc (Weinberger, 1989) and electron temperature $\sim 10^4$ ^{0}K (Kaler, 1986) were adopted. The use of distances as given in Cahn and Kaler (1971) or Daub (1982) still give a high value of ε. Thus it may be relevant to say, based on the preceding discussions, that no accurate determination of the expansion velocity from well-split emission line profiles exists for this object.

The profiles of the [OIII], Hα and [NII] lines are shown in Figs. 3.2, 3.3 and 3.4. As can be seen from the figures this nebula shows an unusual feature of a three component structure in the [NII] and [OIII] lines. This feature of three blended components with the central one considerably stronger was similarly found by Wilson (1950) in the [OII] 3726 and 3728Å lines but not in the [OIII] and [NII] lines. In our observed profiles, we also find a stronger (3 to 4 times) central component flanked by two weaker components. In view of their shape a three gaussian fit has been applied to the [OIII], Hα and [NII] profiles and the dotted lines in the figures indicate their composite sum. The positions (in terms of velocity) and relative intensities of the three gaussians with respect to the central component are given in Table 3.2.

[O III] LINE PROFILE IN IC 4593
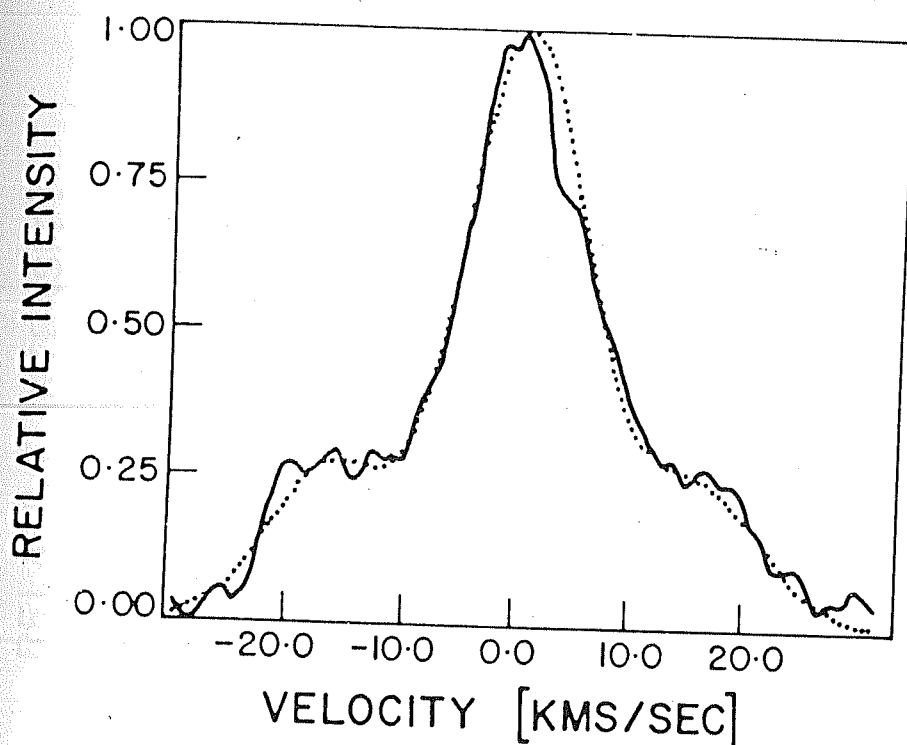
Fig.3.2:   The [OIII] 5007Å line profile in IC 4593. The observed profile (indicated by the continuous line) has been fitted by a double-component Gaussian indicated by the dotted line.
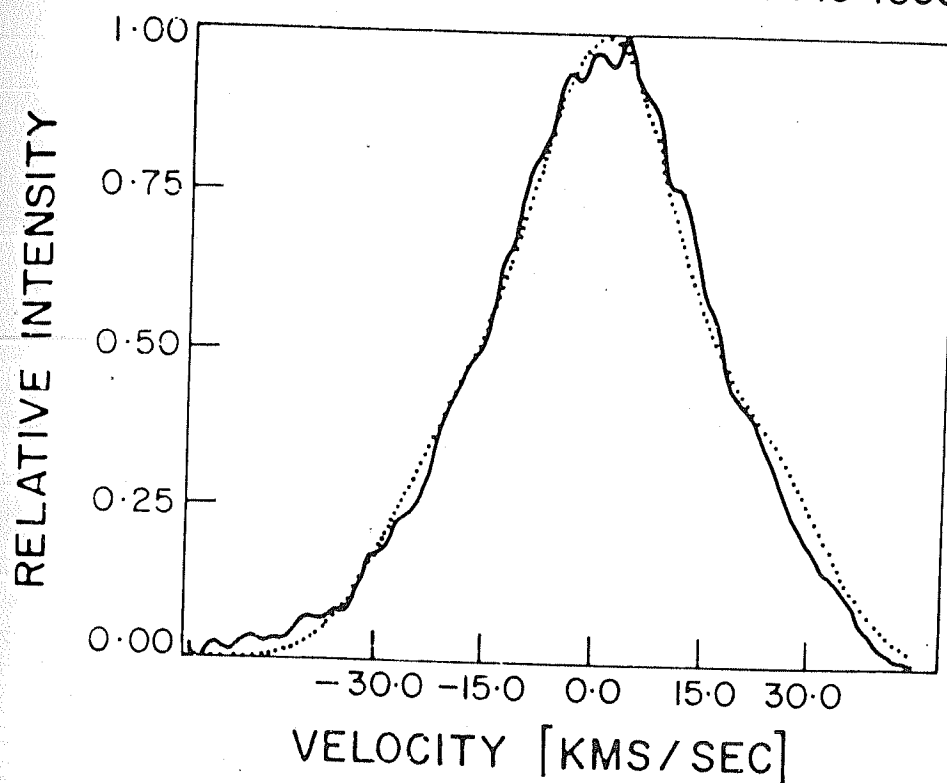
Fig.3.3:   The Hα 6563Å line profile in IC 4593. The observed
profile (indicated by the continuous line) has been fitted by a
double-component Gaussian indicated by the dotted line.
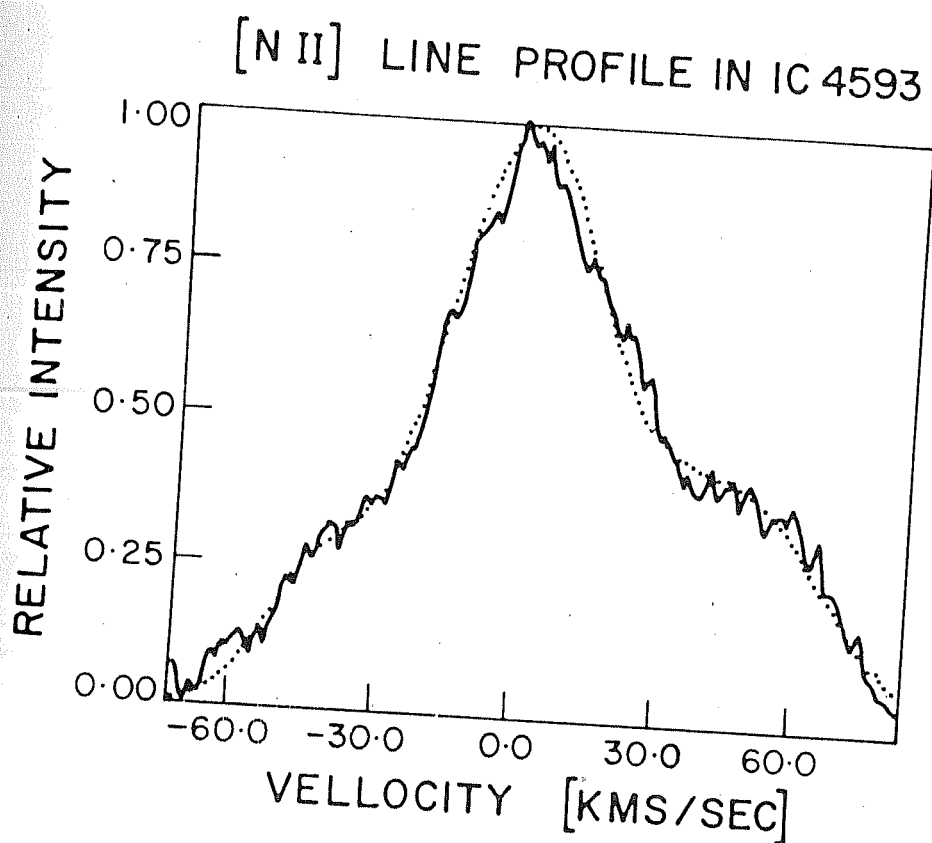
Fig.3.4: The [NII] 6584Å line profile in IC 4593. The observed profile (indicated by the continuous line) has been fitted by a double-component Gaussian indicated by the dotted line.

Table 3.2

Emission line parameters for IC 4593

Emission line	Velocity w.r.t. central component (km/s)			Intensity w.r.t. central component		
	G1[*]	G2	G3	G1	G2	G3
[OIII]5007Å	-17.0	0	16.0	0.27	1.0	0.24
[NII]6584Å	-41.0	0	47.0	0.22	1.0	0.39
Hα 6563Å	-21.0	0	23.0	0.30	1.0	0.30

* G1,G2,G3 refer to the 3 gaussians.

From the table it can be seen that it is not possible to assign a single expansion velocity to the nebula. The two outer components are on the average separated from the central one by 16.5 km/s and 44.0 km/s for the [OIII] and [NII] lines respectively and separated from each other by 33.0 km/s and 88.0 km/s for the same lines. There exists a large difference in the expansion velocity between the [NII] and the [OIII] lines as is similarly found for instance in NGC 6210 and NGC 6567 (Wilson 1950). This indicates that the outer edges of the nebula where the lower ionization stages ([NII]) are formed are expanding faster than the inner regions. To account for the triple component structure it may be conjectured that the spatial geometry of IC 4593 in the line-of-sight may be such that it could give rise to a triple component emission profile. It may be pointed out that such

a triple component structure in planetary nebulae is rare and has so far been found only in NGC 650/1 (Taylor 1979).

However, in view of the recent high-resolution CCD photographs published by Chu, Jacoby and Arendt (1987) and Balick (1987) the observed 3-component line profiles may be interpreted as being due to the multiple shell structure of the nebula. The two weaker outer components in the profiles of [OIII] and [NII] in the Figures 3.2 and 3.4 should then correspond to the outer shell of the nebula which is fainter (Chu, Jacoby and Arendt, 1987) while the central strong peak represents the inner nebula. This implies that in IC 4593 the outer shell is expanding with a higher velocity than the inner nebula. This is a rather interesting situation seen also in a few other multiple shell PNe like IC 3568, NGC 6826 and NGC 6891 (Chu, 1989) in which it is found that the outer shell is expanding faster than the inner one. This kind of kinematic behaviour is not expected from the interacting-winds model for PNe formation wherein a smaller velocity for the outer shell is predicted with respect to the inner one. The possibility of a fast inner shell sieving through the slower outer shell has also been shown by Kwok, Purton and Fitzgerald (1978) to be unfeasible because the mean free path of the atoms at the interface of the two shells is small compared to the characteristic dimensions of the shells. In both the two-winds model of Kwok, Purton and Fitzgerald (1978) and the three-winds model considered by Schmidt-Voigt and Köppen (1987), the outer halo or the outer shell of a multiple shell PN corresponds to the ionized precursor AGB wind which should in general have a lower expansion velocity than the inner shells.

Alternative mechanisms have therefore to be invoked which can preferentially accelerate the outer shell. One of such mechanisms proposed by Mathews (1978) requires that the outer shell of the nebula be richer in dust content than the inner one. The action of radiation pressure on dust can then preferentially accelerate the outer shell to a higher velocity than the inner one. This may explain the kinematics of IC 3568 which is known to be a high dust content PN (Cohen, Harrington and Hess, 1984). Whether this is the reason for the kinematic behaviour of the different shells of IC 4593 remains however to be ascertained. Another cause of preferential acceleration of the outer shell may be due to the diffusion of the gas from the outer shell into a vacuum like interstellar medium. A rough estimate can be made for this effect. The velocity with which diffusion takes place is of the order of the thermal velocity of the ions (Gurzadyan 1970). If we approximate the temperature of the nebula to be $T \sim 10^4 \ ^0K$ then the half width of the thermal velocity distribution of the [OIII] and [NII] ions is ~ 5 km/s. Thus the outer shell may expand this much faster than its true expansion velocity. However even allowing for this margin the observed expansion velocities in IC 4593 for the outer shell in [NII] and [OIII] appear to be significantly higher than the inner shell.

In the light of the above discussions it is seen that the kinematic properties of IC 4593 are intriguing and do not fit straight into the interacting-winds mechanism for PNe formation. In fact the kinematic behaviour of the multiple shell PNe, which within themselves have different morphological forms, poses a challenge and also provides clues to the formation

mechanism of PNe. However, progress in this direction has only begun very recently and kinematic data is sparse. Most of the work in this area is contained in Chu, Jacoby and Arendt (1987); Chu and Jacoby (1987) and Chu (1989). The work of the above authors indicate that any one single mechanism for PNe formation cannot by itself explain the various morphological forms and also the diverse kinematical properties of all the multiple shell PNe. This theme is discussed in greater details in Chapter V wherein the successes and possible limitations of the different PNe formation mechanisms in explaining the observations is discussed.

3.5 NGC 6153:

NGC 6153 (PK number 341 $+5^0 1$) is a southern object (R.A. (1950) = $16^h 28^m 05^s$, Dec = -40^0, $08'$, $58''$). Recent CCD images by Pottasch, Dennefeld and Mo (1986) given in Fig.3.5 shows that its morphology comprises of an ellipsoidal shell with its major axis of dimension 24" oriented approximately at a position angle of 14^0. Almost perpendicular to the major axis, at a position angle of ~ 110^0 are found two bright knots or ansae which are separated from each other by ~ 24". The image of the nebula also shows the presence of filaments and condensations. The work of Pottasch, Dennefeld and Mo (1986) also indicates that the abundances of most of the elements in this object are much higher than in other nebulae. This PN is not a well studied object and with respect to the kinematics no expansion velocities (see for example, Sabbadin 1984 or Weinberger 1989) had been reported till the present observations.

The observed [OIII], Hα and NII profiles in NGC

Fig.3.5:   A CCD picture of NGC 6153 taken with a B (Johnson)
filter (from Pottasch, Dennefeld and Mo, 1986). North is to the
top and East is to the right.

6153 are shown in Figs. 3.6, 3.7 and 3.8 respectively along with the double gaussian fits. Both the [OIII] and [NII] profiles show a distinct double component structure. In Hα a clear split is not seen probably due to the greater thermal broadening of the individual components of the profiles. In Table 3.3 we present the main characteristics of the emission lines in this PN.

Table 3.3

Emission line parameters for NGC 6153

Emission Line	Width of first Gaussian (km/s)[*]	Intensity of first Gaussian (I_1)	Width of second Gaussian (km/s)	Intensity of second Gaussian (I_2)	I_1/I_2	V_{exp} km/s
[OIII]5007Å	21.80	0.50	23.30	1.00	0.50	12.7
Hα 6563Å	40.10	0.67	37.50	0.66	1.01	14.0
[NII]6584Å	33.00	0.45	31.80	1.00	0.45	17.3

[*] widths refer to the FWHM

The most interesting feature in this PN seems to be the presence of a bipolar flow. As may seen from the [NII] profile, two weaker structures are found in the wings at ~ ±55 km/s probably associated with the two knots or ansae mentioned earlier. This association is supported by the fact that the [OIII] line profile obtained with a 15" aperture (which does not cover the knots) shows none of these high velocity components. These components were seen only when an aperture of 30" which
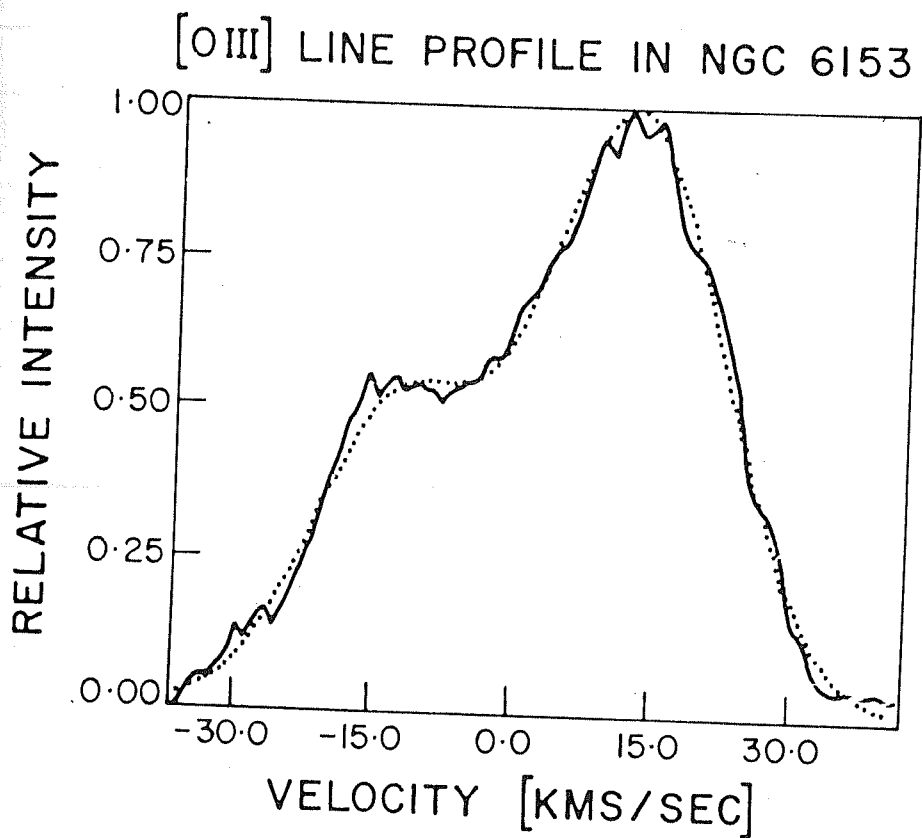
Fig.3.6: The [OIII] 5007Å line profile in NGC 6153. The observed profile (indicated by the continuous line) has been fitted by a double-component Gaussian indicated by the dotted line.
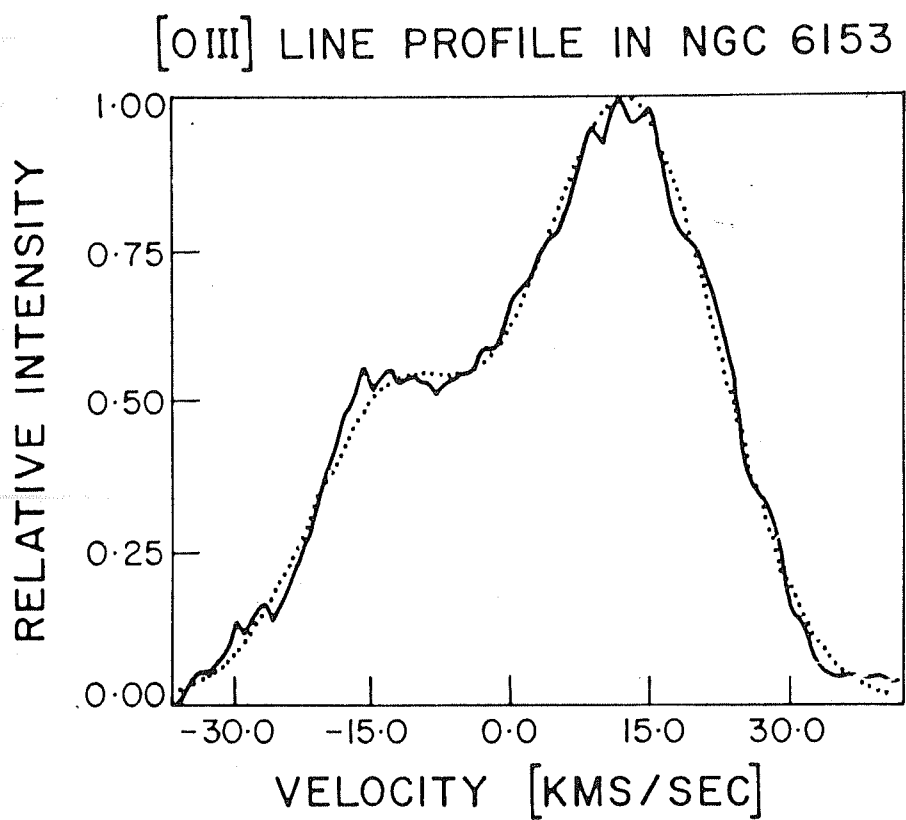
Fig.3.6: The [OIII] 5007Å line profile in NGC 6153. The observed profile (indicated by the continuous line) has been fitted by a double-component Gaussian indicated by the dotted line.
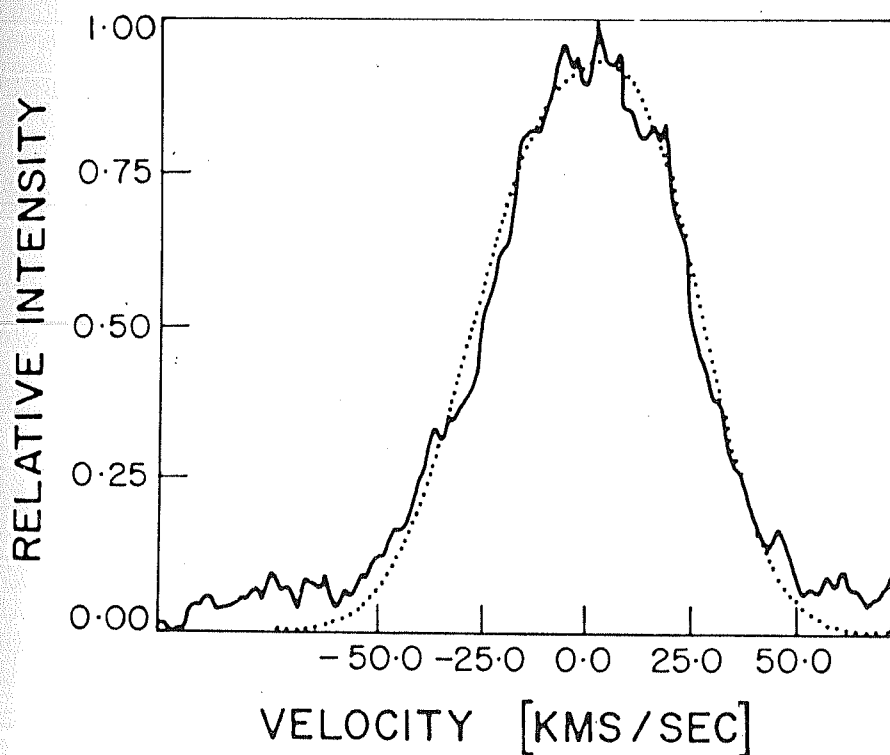
Fig.3.7:   The Hα 6563Å line profile in NGC 6153. The observed profile (indicated by the continuous line) has been fitted by a double-component Gaussian indicated by the dotted line.

[N II] LINE PROFILE IN NGC 6153
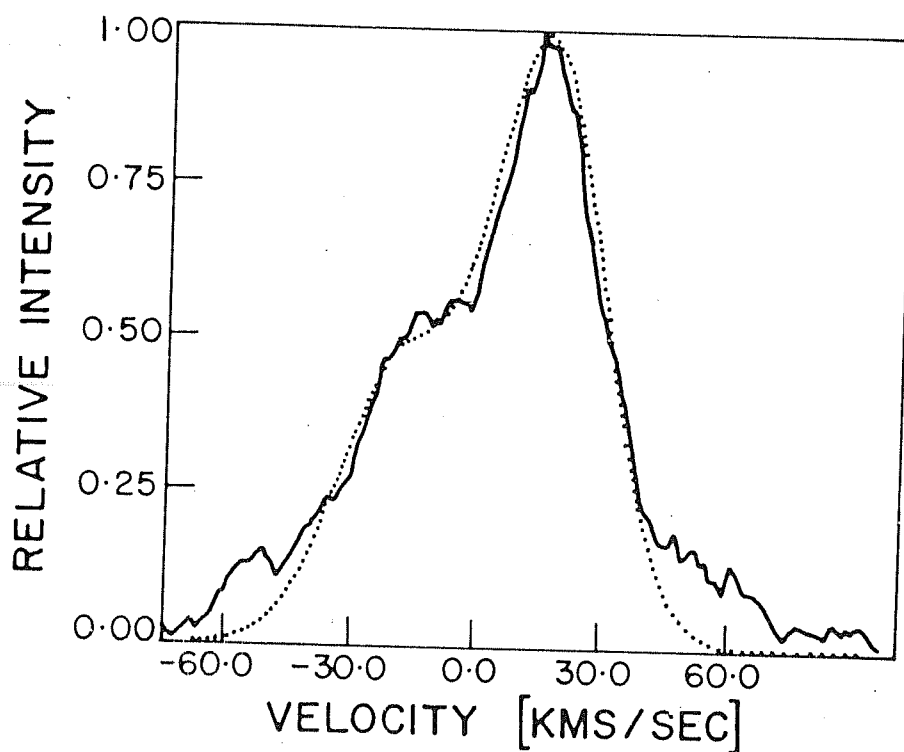
Fig.3.8:   The [NII] 6584Å line profile in NGC 6153. The observed profile (indicated by the continuous line) has been fitted by a double-component Gaussian indicated by the dotted line.

encompasses the knots was used as in the [NII] profile. The observed radial velocities of the bipolar flow of $\pm$ 55 km/s are the line-of-sight velocities. Since the spatial orientation of the object cannot be determined precisely, the observed bipolar flow velocity of $\pm$55 km/s is a lower limit and the true flow velocity may be considerably higher than this.

The presence of such bipolar flows characterized by line-of-sight velocities in the range 10-60 km/s have been found in several PNe-for e.g. NGC 40, 3242, 6543, 6826, 7009, 7354, 7662 (Balick, Preston and Icke, 1987) and also in NGC 6751 (Gieseking and Solf, 1986). The Eskimo nebula (NGC 2392) shows a flow velocity as high as ~ 170 km/s. A hydrodynamic mechanism based on the two-wind model has been proposed by Balick, Preston and Icke (1987) to explain these collimated fast flows. In the above mechanism it is assumed that the slow wind envelope that surrounds the star is denser at the equator than near the poles. This density gradient allows the fast wind to move more freely in the polar direction thereby leading to a prolate ellipsoidal shock front. A corresponding prolate ellipsoidal reverse shock front also occurs but facing towards the star and this reverse shock begins to collimate the fast wind. This collimated flow then breaks through the poles of the ionized prolate ellipsoidal envelope leading to the bipolar flows. However one particular point may perhaps be mentioned with respect to NGC 6153. In this object the bipolar flow is found to be perpendicular to the major axis of the ellipsoidal shell of the nebula whereas in the mechanism outlined above the collimated flows occur along the major axis. Whether this observed effect in NGC 6153 is due to a

geometrical orientation of the nebula or whether a new mechanism for the origin of the bipolar flows is required is not certain.

An estimate of the ion temperature in the nebula was also made from the widths of the Hα and [NII] lines using a method due originally to Courtes, Louise and Monnet (1968) who had applied it to extended HII regions. The principle of the method is briefly described here. The width of a line arises from thermal broadening, internal motions of the gas including turbulence and from instrument broadening. The very marginal wavelength difference between the Hα and [NII] lines will result in the same instrument broadening. Further, since the formation of the [NII] and Hydrogen ions require almost the same ionization potential (14.53 and 13.6 ev respectively) they may be assumed to coexist in the same region and hence be characterized by the same internal motions and turbulence. Therefore the difference in the widths of the Hα and [NII] lines will result primarily due to thermal broadening which is a function of the mass of the ionic species in question. Based on the above line of reasoning Courtes, Louise and Monnet (1968) and Dyson and Meaburn (1971) showed that the width h of a line in terms of the temperature T, wavelength λ and atomic mass M of the ion species is given by

$$h/\lambda = 0.716 \times 10^{-6} \left[T/M \right]^{1/2} \qquad (3.3)$$

The temperature of the nebula, in terms of the observed widths W_N and W_H of the [NII] and Hα lines respectively, is then easily obtained from the above equation as

81

$$T = 4.93 \times 10^{-4} \, (W_H{}^2 - W_N{}^2) \qquad (3.4)$$

In the above equation the extra broadening of the Hα line due to its fine structure should also be taken into account. The requisite correction to be made in W_H, by taking into account the above factor, has been outlined by Dyson and Meaburn (1971). Substitution of the observed widths of the profiles in eqn. 3.4 yields a temperature $T = 8950 \pm 2000^0 K$. This is the value obtained by averaging the temperatures computed for the approaching and receding components of the line profiles. The error in the temperature arises due to the error in the determination of the widths of the profiles from the gaussian decomposition. The measured temperature compares reasonably well with the electron temperature of 8100 ± 400^0 K measured from the forbidden line ratio of several ionic species by Pottasch, Dennefeld and Mo (1986). It may however be pointed out that temperature determination by the above method may have some drawbacks. Firstly, it cannot be ruled out that the [NII] line originates from the outer regions while the Hα line may come by and large from all over the nebula. Also there could be small-scale structures present along the line-of-sight and/or in the plane of the nebula within the field of view. Therefore, determination of ion temperatures by the above method will perhaps be more accurate in the case of observations of high-spatial resolution (Walsh and Meaburn, 1987).

3.6 IC 4406 :

IC 4406 (PK number 319 +$15^0$1) is another southern planetary nebula (R.A. 14^h 14^m 30.8^s, Dec -43^0 $55'$). In the Perek and Kohoutek (1967) catalogue its morphology appears to be that of a highly flattened ellipsoid with a maximum extent of ~ 90" along the major axis. The minor axis dimension is approximately 30". It has been classified as a rectangular PN by Gurzadyan (1970) but this description does not seem appropriate according to the PK images of the object.

Based on the recent PNe expansion velocity catalogue of Weinberger (1989) it does not appear that a precise [OIII] expansion velcity has been determined for this object. From the above catalogue the expansion velocities quoted are $2V_{exp} \leq 12$ km/s (Acker, 1976), $2V_{exp} = 12$km/s (Robinson, Reay and Atherton, 1982) and $2V_{exp} < 12$km/s (Meatheringham, Wood and Faulkner, as quoted in Weinberger, 1989 - this work has not appeared in print till date). The V_{exp} value quoted by Robinson et al is based on the observations of Bohuski and Smith (1974). These authors, using a pressure scanning FPS, have observed the nebula in [OIII] with 13" and 60" diaphragms centred on the object. However, their line profiles do not show a splitting into two components. To estimate the expansion velocity therefore, Robinson et al have applied the relation (FWHM) intrinsic $\simeq 2V_{exp}$ (details of this approximation are discussed in section 3.4) to the Bohuski and Smith data and inferred an expansion velocity of 6 km/s. Since our F.P.S. can resolve expansion velocities of ~ 5 km/s compared to the 12 km/s expansion velocity resolution of the FPS used by Bohuski and Smith it was hoped that a well split line profile could be obtained for

this object.

In Fig.3.9 we show the [OIII] line profile in IC 4406. The profile shows a clean gaussian nature with no hint of line-splitting. The low FWHM of the profile (~ 20 km/s) suggests a low expansion velocity. A double gaussian fit indicates that V_{exp} = 5 km/s. Alternatively one can use the method of Robinson et al (1982) to estimate the expansion velocity. If the intrinsic width of the line is assumed to be a gaussian, then since the thermal broadening is gaussian in nature and the instrument function is closely approximated by a gaussian (refer Fig 2.4 of Chapter II), we have

$$W^2(\text{observed}) = W^2(\text{intrinsic}) + W^2(\text{thermal}) + W^2(\text{instrument})$$

(3.5)

where W is the FWHM of the different broadening functions. In our case W(observed) $\simeq$ 20 km/s, W(thermal) = 5.35 km/s (for the [OIII] ion at 10^4 ^{0}K) and W(instrument) $\simeq$ 10 km/s. Using eqn. 3.5 to determine W(intrinsic) we infer a value of ~ 8 km/s for the expansion velocity. This agrees reasonably well with that derived from the double gaussian fit to the data and also with V_{exp} values obtained by Robinson et al by using the same method as above.

IC 4406, $[OIII]$ LINE, APERTURE 45"
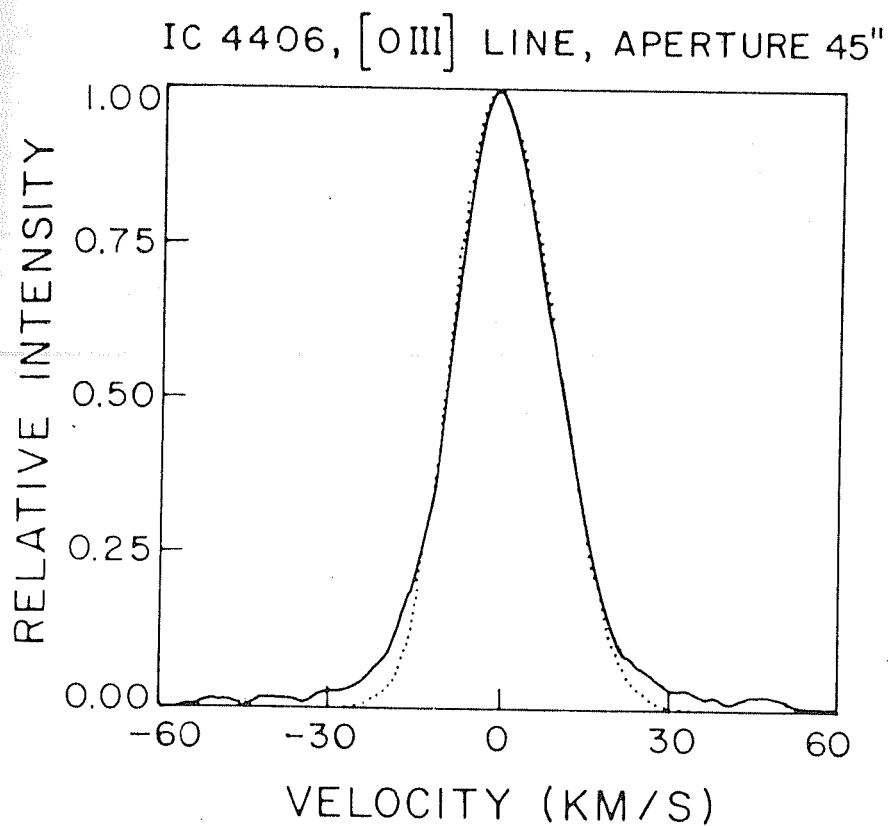
Fig.3.9: The [OIII] 5007Å line profile in the planetary nebula IC 4406. The observed profile (indicated by the continuous line) has been fitted by a double-component Gaussian indicated by the dotted line.

3.7 NGC 2818:

NGC 2818 is a southern PN (PK number 261 $+8^0$1, R.A.(1950) $= 9^h\ 13^m\ 59^s$, Dec $= -36^0\ 24'\ 58''$) showing a bipolar morphology. It is unique among galactic PNe in the sense that it is the only known object which is probably associated with an open cluster having the same name. The morphological structure of this PN comprises of an hour-glass form (of angular dimension 60"x130") oriented in the N-S direction with the narrow waist oriented in the E-W direction. A photograph of the object (from Dufour, 1984) is given in Fig.3.10. The kinematics of NGC 2818 have been studied by Dufour (1984) using an echelle slit spectrograph with the 1.4" wide slit oriented in position angle 0^0. From the slit spectra Dufour finds the expansion velocities in [NII] and [OIII] to be 51 km/s and 53 km/s respectively.

We present in Fig.3.11 the line profiles obtained in NGC 2818 using the FPS. Each of the profiles have been fitted with three gaussians to estimate the profile parameters. The details of the line profile parameters are given in Table 3.4.

Table 3.4

Emission line parameters for NGC 2818

Emission line	FWHM of the Gaussian components (km/s)			Relative Intensity of the components			V_{exp} (km/s)
	G1*	G2	G3				
[OIII]5007Å	09.5	22.0	20.0	0.47	1.00	0.90	23.0
Hα 6563Å	32.5	16.3	27.5	0.95	0.75	0.50	25.0
[NII]6584Å	24.0	19.7	21.0	0.62	0.95	0.90	27.0

* G1, G2 and G3 refer to the three gaussians
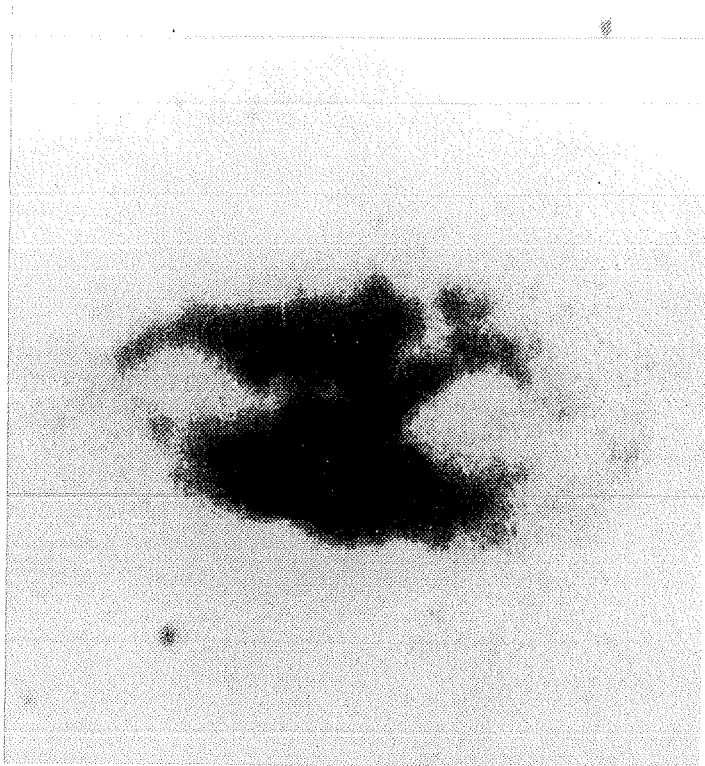
Fig.3.10:   The planetary nebula NGC 2818 photographed through a
[NII] 6584Å filter (from Dufour, 1984). North is to the top and
East is to the left.
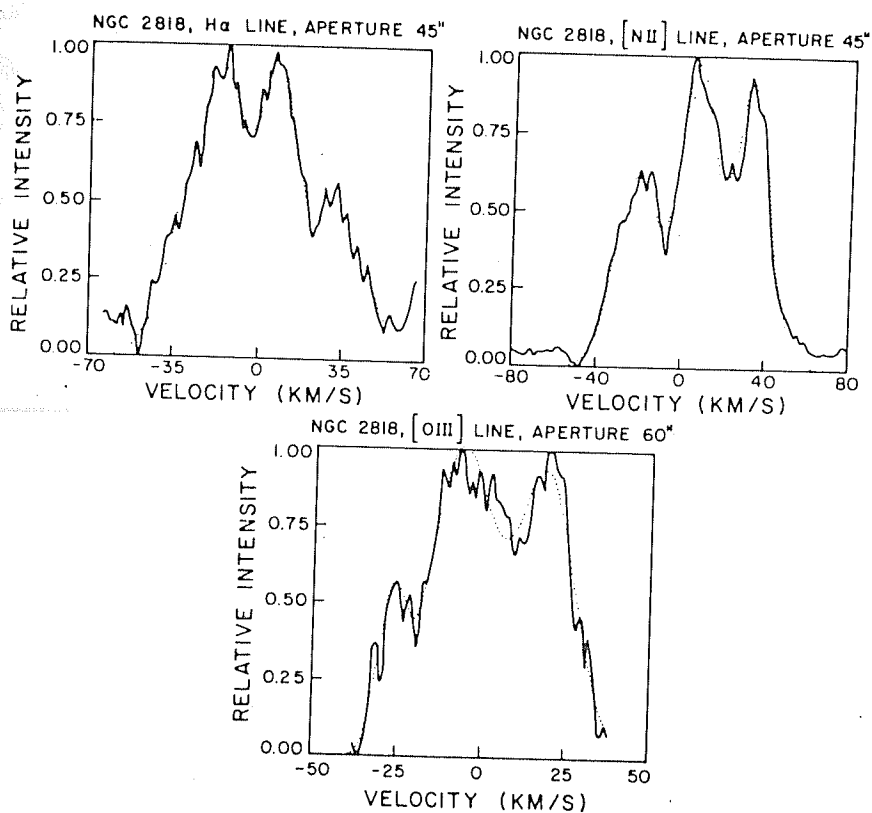
Fig.3.11:   The   [OIII]   5007Å,   Hα   6563Å   and   [NII]   6584Å   line
profiles in NGC 2818.Each of the observed profile (indicated by
the   continuous   lines)   has   been   fitted   by   a   three-component
Gaussian indicated by the dotted lines.

What is most interesting in the line profiles of Fig 3.11 is the triple structured profile obtained in each of the [OIII], Hα and [NII] lines. As mentioned earlier such a triple component profile is rare in PNe and has been observed only in NGC 650/1 (Taylor, 1979) and in IC 4593 (as discussed earlier). The expansion velocities quoted in the above table are between the outer two components of the profiles. Our central region expansion velocity values of 27 and 23 km/s in the [NII] and [OIII] linesrespectively are significantly smaller than those reported by Dufour and may be a consequence of the large aperture used by us (refer Table 3.1) for studying this object. Further, Dufour mentions that the echelle spectra show a complex velocity structure and it is not clear from his work whether the expansion velocities quoted by him are for the central region or averaged over the length of the slit. Our V_{exp} values, however, agree a little better with the (V_{exp})[OIII] $=40$ km/s measured by Meatheringham, Wood and Faulkner (as quoted in Weinberger, 1989). Since the details of the above work (Meatheringham et al) are not available as yet, a critical comparison between the results is, however, not possible.

Since our observations are restricted to the central region, only a possible qualitative explanation for the triple structure of the line profiles can be advanced. Bipolar PNe, which have been well mapped, indicate that the expansion velocities in the waist of such PNe are smaller than in the hour-glass lobes (Meaburn and Walsh 1980b for NGC 6302, Sabbadin, 1981 for NGC 650/1 and Icke, Preston and Balick, 1989 for NGC 2440;). Models for PNe formation of the hour-glass form, based on

the two-wind mechanism have been suggested by Kahn and West (1985) and Icke (1988). In Chapter V we also propose another mechanism for the formation of bipolar PNe of hour-glass morphology. In the two previously cited models and also in our case, the velocity structure in hour-glass PNe predicts a smaller expansion velocity in the waist of the nebula than in the lobes. With reference to NGC 2818, since the aperture sizes used cover both the waist and a significant part of the hour-glass lobes, it appears that the two outer components of the observed profiles correspond to the faster expanding lobes and the central component to a slower expanding waist. However, the intriguing velocity structure of NGC 2818 warrants a more extensive mapping to understand its kinematics better.

3.7.1 Nebular parameters of NGC 2818:

Because of the probable association of NGC 2818 with an open cluster a more accurate determination of the distance to the nebula can be made and hence more accurate estimates of nebular parameters like mass and electron density (whose estimation depends on an accurate knowledge of the distance) can be obtained.

3.7.1a Distance to the nebula:

The probability that NGC 2818 belongs to the associated star cluster seems very likely for reasons not only of spatial proximity, but of similar radial velocities (Tifft, Connolly and Webb, 1972) and of similar extinction (Dufour, 1984). The distance to the cluster has been determined to be 3.2 kpc by Tifft, Connolly and Webb (1972) by fitting the zero age main

sequence to the cluster color-magnitude diagram. We adopt this value of the distance to the nebula to calculate the other nebular parameters.

3.7.1b Filling factor and electron density:

The difference in electron densities derived from radio continuum measurements and from forbidden line ratios has given rise to the concept of a filling factor ε for a PN (e.g. Mallik and Peimbert, 1988). The filling factor is defined through the relation

$$\varepsilon = N_e^2 \text{ (rms)}/N_e^2 \text{ (FL)} \qquad (3.6)$$

where N_e (rms) is the root mean square electron density determined from a Balmer line flux or radio continuum flux and N_e(FL) is the electron density determined from forbidden line (FL) ratios. The filling factor represents the fraction of the nebula that contains relatively high density forbidden line emitting material.

The rms electron density can be obtained from the free-free radio emission of a radio source which is optically thin at 5 GHz and is given by (e.g., Gathier, 1987)

$$N_e\text{(rms)} = 4.96 \times 10^2 \ S^{1/2} \ T_e^{1/4} \ D^{-1/2} \ \theta^{-3/2} \left[\frac{1+y+3xy}{1+y+xy} \right]^{-1/2} \text{per } cm^3$$

$$(3.7)$$

where S is the 5 GHz flux density in mJy (1 milli Jansky = 10^{-26} erg cm^{-2} s^{-1} Hz^{-1}), T_e the electron temperature in ^0K, D the

distance in kpc, θ the angular radius of the source in arc seconds, y the helium abundance [i.e., N(He/H)] and x is a measure of the fraction of doubly ionized helium ie, $[x = 1+2 \, N(He^{2+}/He^{+})]$.

The radio continuum measurements of 397 PNe by Milne and Aller (1982) at 5 and 14.7 GHz using beam-widths of 4.5' and 2.1' respectively have shown that PNe are optically thin at the above frequencies. In particular for NGC 2818, the observed 0.033 and 0.036 Jy fluxes at 5 and 14.7 GHz respectively (Milne and Aller, 1975 and 1982) give a spectral index $\beta = +0.08$, where $S(\upsilon)$ is proportional to υ^{β}, and which is much closer to the optically thin limit index of -0.1 than the optically thick limit index $\beta = +2.0$.

In eqn. 3.7 the values of the different parameters that we use are S(5GHz) = 33mJy, D=3.2 kpc (Tifft, Connolly and Webb, 1972), T_e=12,000^0 K (Kaler, 1986 and references therein) and x and y equal to 2.5 and 0.16 respectively (Dufour, 1984). Attributing an angular radius to NGC 2818 is difficult due to its shape and therefore we assume a size of ~ 45" which is an average of the maximum and minimum extent of the object. Substitution of all these values in eqn. 3.7 yields for the rms electron density N_e(rms) $\simeq$ 45/cm^3.

The value of N_e(FL) from the[SII] line ratios has been measured in this nebula to be 430/cm^3 by Dufour (1984). Therefore using eqn. 3.6 the filling factor is found to be 0.01 in this nebula. This value is consistent with the small value of the average filling factor (ε = 0.05) found by Torres-Peimbert and Peimbert (1977) for 48 PNe.

The value of N_e(rms) can alternatively be

calculated by knowing the H(β) flux from the relationship (Pottasch, 1984: p.106)

$$N_e(rms) = 2.74 \times 10^4 \left[\frac{F(H\beta) \ T_e^{0.88}}{\theta^3 D} \right]^{1/2} \qquad (3.8)$$

Here F(Hβ) is the H(β) flux corrected for extinction and measured in units of 10^{-11} ergs $cm^{-2}s^{-1}$, T_e the temperature is measured in 10^4 ^0K and θ and D are as defined earlier. The measured H(β) flux in NGC 2818 is 5.01×10^{-12} ergs $cm^{-2}s^{-1}$ and for the reddening factor C(Hβ) = 0.35 (Dufour, 1984) the corrected H(β) flux is equal to 1.12×10^{-11} ergs $cm^{-2}s^{-1}$. From eqn. 3.8 therefore, using the aforementioned values of θ, D and T_e we obtain $N_e(rms) = 58/cm^3$ which is in good agreement with the value determined from radio fluxes.

3.7.1c Mass of the nebula :

The ionized mass of the nebula can be obtained from the relation given by Maciel and Pottasch (1980)

$$M_{ionized} = \frac{4\pi R^3}{3} \ \varepsilon \ m_H \ N_e \ (FL) \left[\frac{1+4y}{1+xy} \right] \qquad (3.9)$$

where R is the radius of the nebula, m_H is the mass of the hydrogen ion and the other terms are as defined before.

Adopting in eqn. 3.9 an average value of N_e(rms) = $50/cm^3$ and using previously mentioned values for the other parameters, we determine the ionized mass of the nebula to be 0.24 $M_\odot$. This is within the range of nebular ionized masses found for PNe ($\sim 10^{-3}$ to 0.4 $M_\odot$, Mallik and Peimbert, 1988), though on the higher side, thereby implying probably that most of the matter is ionized in NGC 2818. It should be noted that Mallick and Peimbert (1988) using a similar analysis have obtained for NGC 2818 a value of 0.20 $M_\odot$ for the ionized mass, N_e(rms) = $180/cm^3$ and ε = 0.130. The differences in the values of N_e(rms) and ε as calculated by the above authors and by us arise due to the different angular sizes considered for the object (Mallik and Peimbert have used a size of $20^{''}$ while our value is $45^{''}$).

3.8 NGC 6302:

NGC 6302 (PK number 349 $+10^0$ 1, R.A.(1950) = 17^h 10^m 21^s, Dec = -37^0 $02^{'}$ $38^{''}$) is a high excitation nebula showing a very complex morphology. No central star has yet been detected for this nebula. Photographs of this object (as shown in Fig.3.12) indicate an hour-glass morphology for NGC 6302. However, several bright condensations and filamentary structures are seen. A longer exposure photograph (Meaburn and Walsh, 1980b) shows an even more extended and complicated structure than is apparent in Fig. 3.12. The most interesting feature in this nebula is the shape of the [NeV] 3426Å line profile obtained by Meaburn and Walsh (1980a). Very broad wings with a total width of 1000 km/s are seen in the [NeV] profiles (but not in the [NII] or Hα lines)which has been
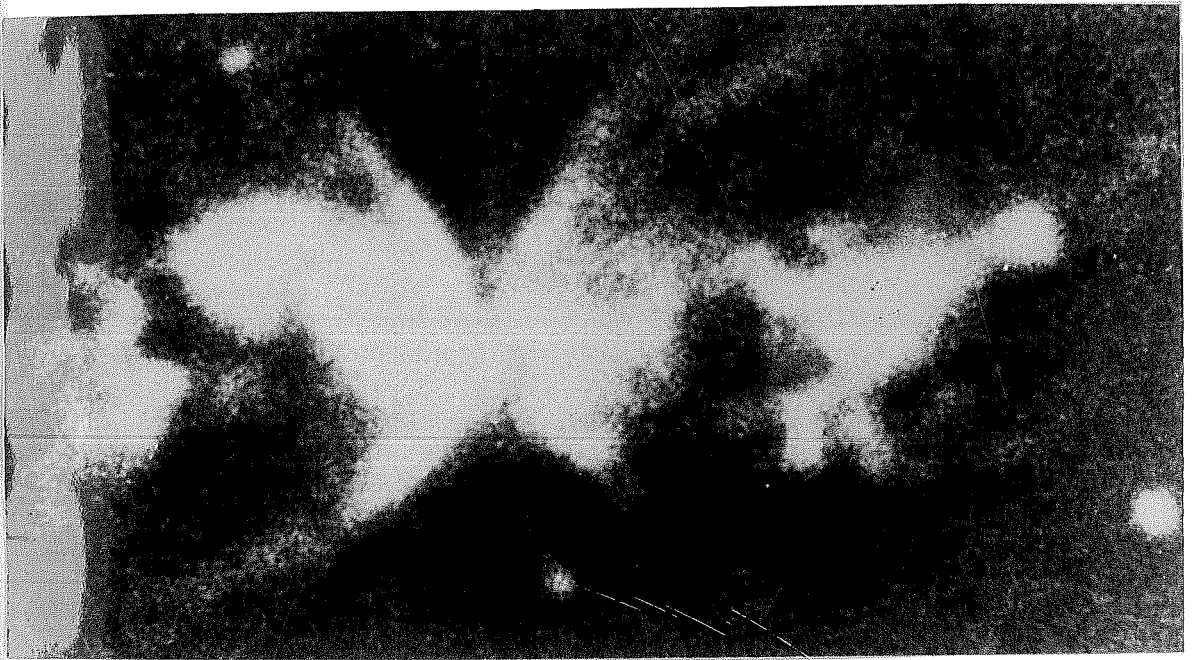
Fig.3.12:   A photograph of the planetary nebula NGC 6302 (from Pottasch, 1984).North is to the top and East is to the left.

attributed to emission from a radiatively ionized stellar wind. This is therefore one of the rare PNe in which evidence for a fast wind is being observed directly in the optical spectrum which has to be otherwise inferred from the P Cygni profiles of the UV lines. A few other cases where broad wings of ~ 1000 km/s are observed are the PNe IC 4997 and BD 30^0 3639 and in the symbiotic star/protoplanetary nebula candidate V1016 Cygni (Pottasch, 1984, p.150).

We show in Fig.3.13 the [NII] line profile obtained in NGC 6302. As may be seen, only a hint of a line-splitting is observed although a marked asymmetry near the peak of the profile is seen. This asymmetry was noticed in all the scans. In Fig.3.14 we present four orders of a single scan on NGC 6302 in which the above effect can be observed. From a double gaussian fit to the line profile of Fig.3.13, an expansion velocity of 12 km/s is inferred which is consistent with an average V_{exp} = 8 km/s measured by Acker (1976) in different ions. However it must be pointed out that a complex velocity field exists in this nebula (Meaburn and Walsh, 1980b) and that the expansion velocity varies significantly over the object. There also appears (from Fig.3.13) a conspicuous asymmetry in the redward wing of the [NII] profile which does not fit the model double gaussian profile indicating probably an additional velocity component.

We cannot deduce directly from our data whether there are broad wings in the [NII] line of the order of 1000 km/s as found in the [NeV] lines. This is so because the free spectral range of the FPS for the [NII] 6584Å line is 4.37Å, thereby permitting a maximum velocity range of 200 km/s to be studied

NGC 6302, [NII] LINE, APERTURE 30"
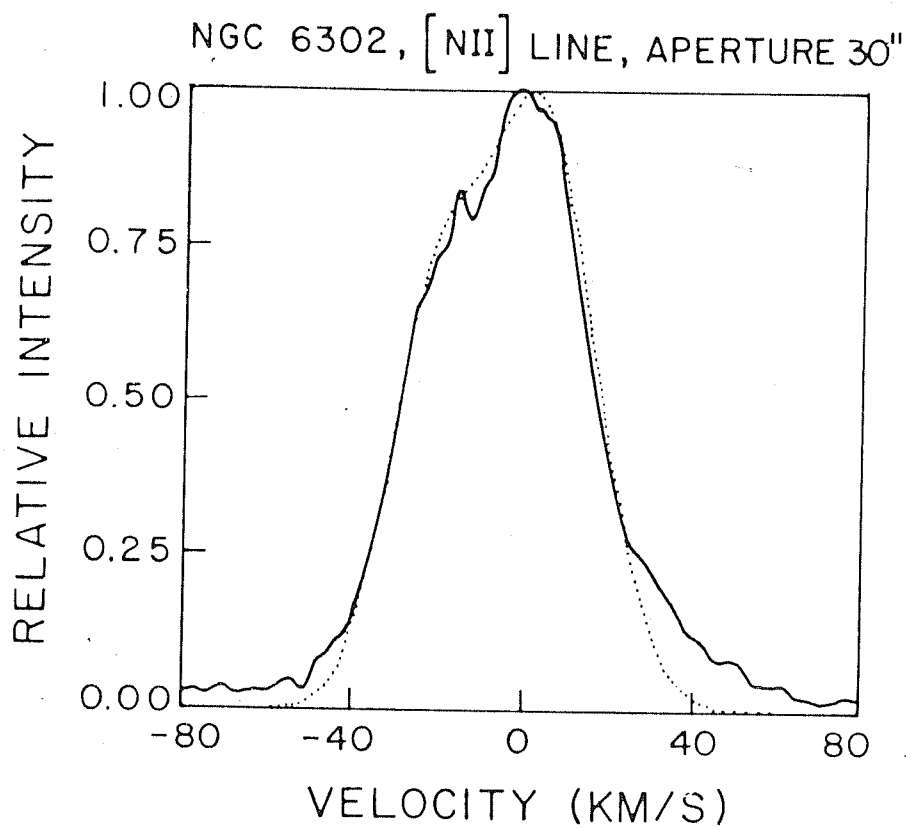
Fig.3.13:   The [NII] 6584Å line profile in NGC 6302. The observed profile (indicated by the continuous line) has been fitted by a double-component Gaussian indicated by the dotted line.
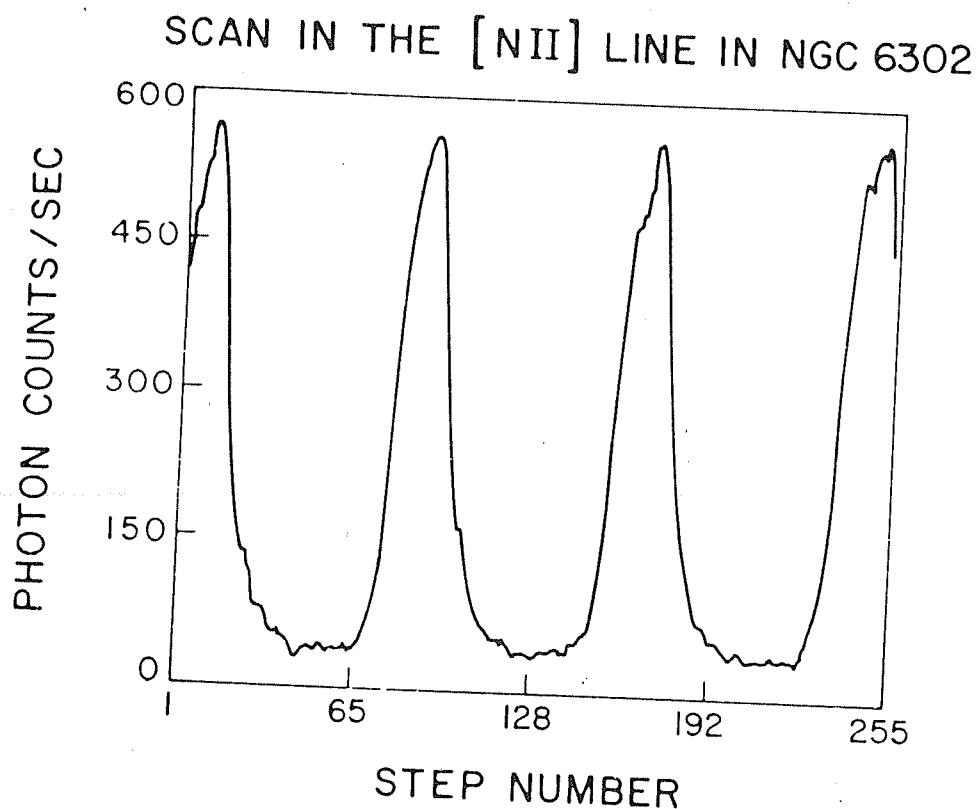
Fig.3.14:   Four orders of the line profile in the [NII] 6584A[0] line in NGC 6302. Step number varies linearly with etalon plate spacing or wavelength.

unambiguously. However, if broad wings which contain a sizeable amount of the line intensity (as in the [Ne V] line) are present, they would substantially raise the continuum level between orders of a scan. But as may be seen from Fig.3.14, where we have directly plotted the photon counts/sec versus the wavelength, the continuum level is very low and marginally above the dark count level of ~ 10 photon counts/sec. From here it may be inferred that large wing-broadening in the [NII] line is absent which is consistent with the observations of Meaburn and Walsh (1980a).

Before concluding this section it may be pointed out that the lack of wing-broadening in the Hα and [NII] lines is a puzzling feature. In the case of IC 4997, BD 30^0 3639 and V1016 Cygni the broad wings are found only in Hα and not in [NII]. A possible explanation for this is that the high velocities originate in regions of high densities and the forbidden lines are therefore quenched by collisional de-excitation (Pottasch, 1984). It is indeed known that IC 4997 and V1016 Cygni do show unusually large electron densities of 2.10^5 and 3.10^6 /cm^3 respectively. However, the case of NGC 6302, where the high velocities are found in the forbidden [NeV] lines appears to be different from the above mentioned PNe. The difference arises, perhaps, out of the fact that the collisional quenching may not be effective in NGC 6302 ($N_e = 7.10^3$ /cm^3) which could be a more evolved PN compared to younger objects like IC 4997. A possible explanation for the lack of broad wings in Hα and [NII] in NGC 6302 could be due to ionization effects. The ionization potential associated with the [NeV] ion (97.02 ev) is much larger than that for either H$^+$ or N$^+$. Hence it may be expected that in regions where [NeV] dominates,

only small amounts of low ionization species such as H^+ or N^+ should exist.

CHAPTER IV
SPATIO-KINEMATIC MODELS FOR THE OBSERVED PLANETARY NEBULAE

4.1 Introduction:

In this chapter we discuss five PNe in which relatively more extensive observations have been made vis-a-vis the PNe discussed in Chapter III. The PNe discussed here are NGC 650/1, 1535, 2346, 2440 and 5882. We present spatio-kinematic/morphological models for these PNe (except for NGC 650/1). As discussed in Chapter III (section 3.2) the aim behind the construction of such models is to infer from the observed velocity field in the nebula the physical processes and mechanisms which are responsible for both its kinematics and its morphology. Kinematic studies are therefore being used as a tool to understand the formative mechanisms of PNe, their evolution and their structural development. In the coming sections, we discuss the observed kinematics of the individual PNe, compare such results with the proposed models and also prepare a framework for the possible formation mechanisms of the PNe involved which are discussed subsequently in Chapter V.

4.2 NGC 2440 :

4.2.1 Morphology and physical properties:

NGC 2440 (PK number 234 $+2^0 1$, RA (1950) $= 7^h 39^m$ 41^S, Dec $= -18^0 05' 26''$) is a complex nebula morphologically. In

the words of Minkowski (1964) it is " an example of an object so complicated that it defies description". The complexity of the object is manifested in a sequence of photographs taken with different exposures by Louise and Pascoli (1985) or by Minkowski (1964). With short exposure, several knots and condensations are seen within a radius of 10" from the centre. We present in Fig. 4.1 a photograph of this rather complicated planetary nebula NGC 2440 taken with intermediate exposure by Minkowski (1964). The figure indicates the presence of a kind of an ellipsoidal shell with its major axis at an approximate position angle of 40^0 and having a maximum extent of ~ 60". At either end of the major axis two blobs or condensations may be seen. Superposed on this apparently ellipsoidal shell is an hour-glass structure with its axis of symmetry oriented almost in east-west direction and having a total extent of ~ 75". Filamentary structures are seen in the hour-glass lobes. In the longest exposure (Minkowski, 1964) the object shows an almost spherical morphology with a rather sharp circular boundary.

The spectrum of the nebula shows a wide range of excitation extending form the [OI] and [NI] lines to the [NeV] and [FeV.II] lines (Aller, Czyzak and Kaler, 1968; Aller and Walker, 1970). The first detection (in the visible spectrum) of the central star of NGC 2440 was reported only as recently as in 1986 by Atherton, Reay and Pottasch (1986). These authors have estimated the Hydrogen and Helium Zanstra temperatures of the central star to be 400,000 ^{0}K and 310,000 ^{0}K respectively. This high value of the temperature makes the central star of NGC 2440 one of the hottest PN nuclei detected till date. The central star
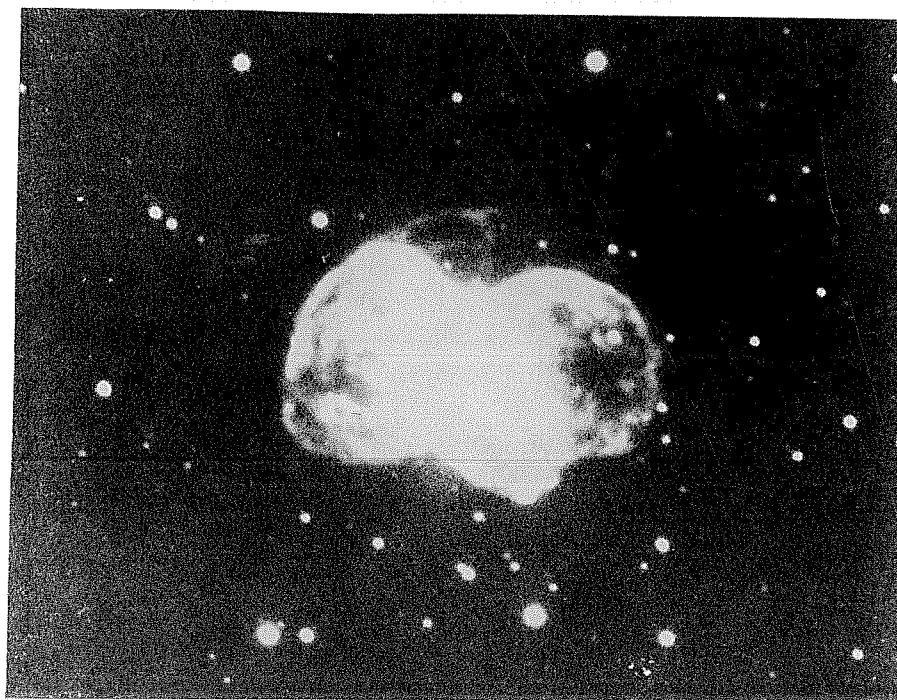
Fig.4.1: A photograph of the planetary nebula NGC 2440 in the light of Hα and [NII] (from Minkowki, 1964). North is to the top and East is to the left.

was also detected in the ultraviolet (through the spectra obtained by the International Ultraviolet Explorer) by Heap (1987) who has estimated the star temperature to be ~ 200,000 ^{0}K by using the Zanstra method as applied to the HeII line at 1640Å.

4.2.2 Previous kinematic studies of NGC 2440:

The kinematics of NGC 2440 has been studied by several observers. In spite of this, however, only one spatio-kinematic model has been proposed for NGC 2440 by Kaler and Aller (1974). Echelle slit spectrographs of the object have been obtained by Wilson (1950), Kaler and Aller (1974, hereafter KA), Bianchi, Grewing, Falcetta and Baessgen (1987, hereafter BGFB), Heathcote and Weller (1987, hereafter HW) and Icke, Preston and Balick (1989, hereafter IPB). Most of the information covered in the above studies, however, refers to the kinematics derived from the [NII] and H$_\alpha$ lines except for the [OIII] expansion velocity values of 23 km/s and 15 km/s reported by Wilson (1950) and KA(1974) respectively. In addition to the above mentioned observations, Louise and Pascoli (1985, hereafter LP) have made high resolution observations of the central region of NGC 2440 in the [NII] and Hα lines. As may be clear, the nebula has not been mapped extensively in [OIII].

Regarding spatio-kinematic models for NGC 2440, the proposed model of KA(1974) may be discussed in a little detail. KA have studied the nebula with the slit of the spectrograph positioned along the ellipsoidal shell (i.e. at position angle 44^0) and have concentrated on the kinematics of the four condensations present along the slit. Two of these condensations

(the outer ones) as mentioned before, lie at the ends of the major axis of theellipsoidal shell and the other two (the inner ones) lie within 10" of the centre. The measured radial velocities of these condensations indicate that the outer knots do not lie on a line with the inner ones. The above studies do not however cover the kinematics of the prominent hour-glass lobes of the nebula. HW (1987) have also suggested a spatio-kinematic model based on the observed slit spectra taken across the nebula. They find that the velocity field of the hour-glass lobes possess a high degree of symmetry. Spectra taken through the lobes show a characteristic shape of a flattened figure-of-eight, each lobe producing one loop of the eight. They therefore propose that the lobes represent two intersecting thin spheroidal shells, each having an expansion velocity of about 75 km/s. They further find that the elliptical disc exhibits chaotic but only low velocity motions. They have explained the morphology of NGC 2440 based on the two-wind mechanism. They propose that the elliptical disc represents the photoionized but dynamically undisturbed AGB wind. The bubble of intensely hot gas blown by the fast wind has broken out on opposite sides of the disc giving rise to the hour-glass lobes.

It may be relevant to quote here the values of the [NII] expansion velocity as measured by different observers so as to enable a comparison at a later stage with our results. From Wienberger's (1989) catalogue on PNe expansion velocities we find the different values of (V_{exp}) [NII] are 31 km/s (Wilson, 1950); 23 km/s (LP, 1985); 16 km/s (BGFB, 1987) and 19 km/s (Diesch et al as given in Wienberger, 1989).

4.2.3 Observations of NGC 2440 :

We have observed NGC 2440 in five different regions in the [NII] 6584Å line and also in five regions in the [OIII] 5007Å line. Some of the observed positions in [NII] and [OIII] are common. Observations in the Hα 6563Å line was restricted to the central region. The positions that have been studied are marked numerically from 1 to 7 on a sketch of NGC 2440 presented in Fig. 4.2 and which has been derived from the Hβ photograph of the object given in BGFB (1987).

The [OIII] line observations were taken at positions 1,4,5,6 and 7 respectively. The [NII] line observations were made at positions 1,2,3,4 and 5 respectively. The angular distances of the different positions from the central position (position 1) are 8" for position 2 and 3; 9" for position 4 and 5 and 10" for position 6 and 7 respectively. The line passing through positions 1,4, and 5 is oriented at a position angle of 135^0 while the line through 1,6,7 is at a position angle of 40^0.

In both [OIII] and [NII] an isolating aperture of 15" diameter has been used in all the corresponding positions observed. In Hα, a 30" aperture was used. For sake of convenience and a quick look up, the observational details described above along with other relevant information is summarized in Table 4.1.
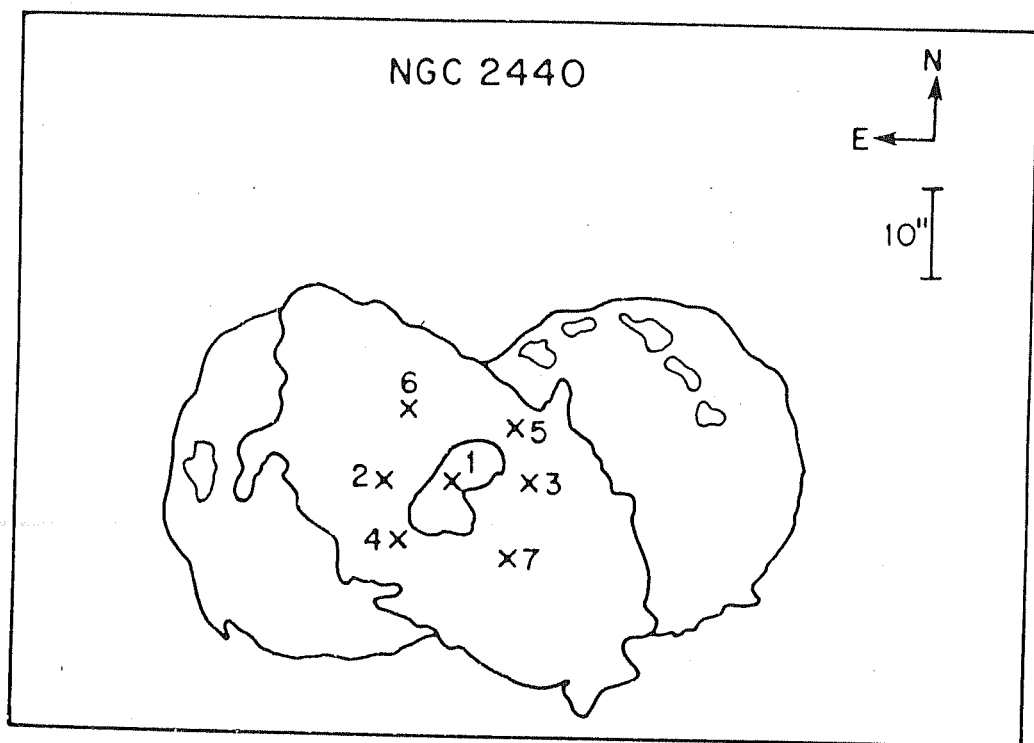
Fig.4.2: A sketch of NGC 2440 derived from the Hß photograph by Bianchi, Falcetta, Baessgen and Grewing (1987) on which are marked the different positions at which the present observations have been made.

Table 4.1

Details of observation in NGC 2440

Emission line	Position on nebula	Distance of position* from centre(arc sec)	Diameter of aperture (arc sec)	Number of line profiles	SNR
[OIII] 5007Å	1	-	15	8	15.0
	4	9	"	2	4.00
	5	9	"	4	14.0
	6	10	"	4	8.00
	7	10	"	4	13.0
[NII] 6584Å	1	-	"	2	21.0
	2	8	"	2	19.0
	3	8	"	2	5.00
	4	9	"	2	19.0
	5	9	"	2	12.0
Hα 6563Å	1	-	30	4	8.00

* refer text (this section) for details on the positions.

4.2.4 Kinematic results in NGC 2440 :

The line profiles obtained in NGC 2440 in the [OIII], [NII] and Hα lines are presented in Figs. 4.3, 4.4, and 4.5 respectively. As may be seen, most of the profiles in each of the lines show a clear line splitting into a blue and a red component. However, broad wings or additional components are noticed in the [OIII] profile at position 6 and in the [NII] profiles at positions 3 and 5. We have made a double gaussian fit to most of the line profiles to estimate the profile parameters like expansion velocity, widths of the individual components etc.
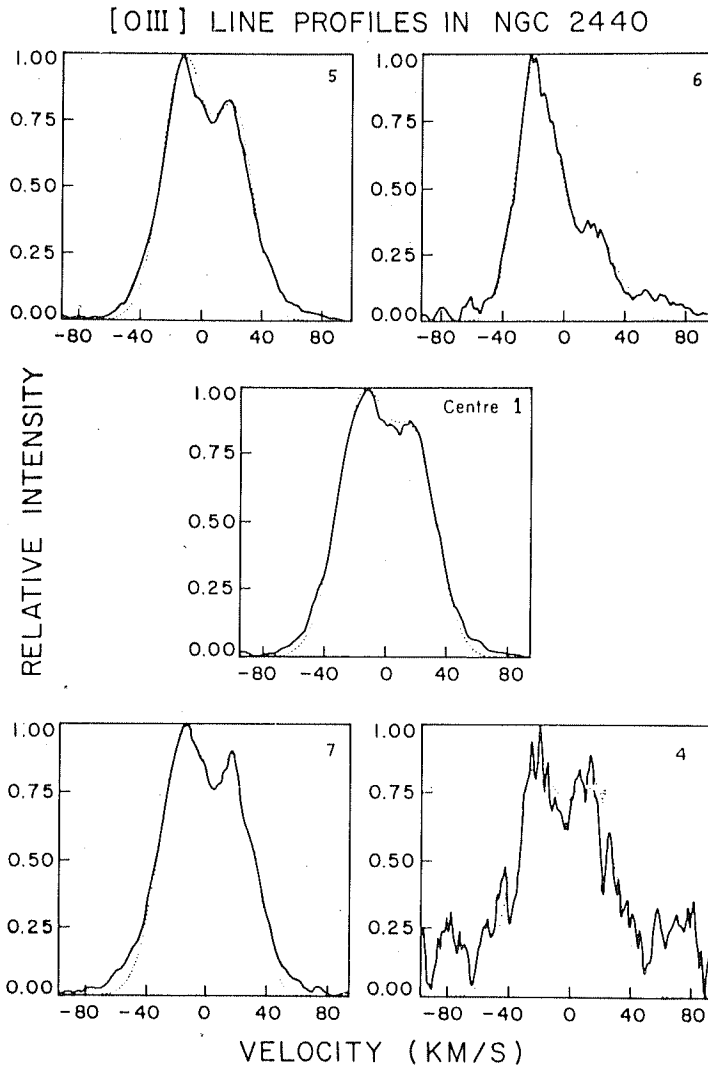
Fig.4.3:   The [OIII] 5007Å line profiles in NGC 2440. The observed profiles (indicated by the continuous lines) have been fitted by double-component Gaussians indicated by the dotted lines.The position on the nebula to which each line profile corresponds is also indicated.
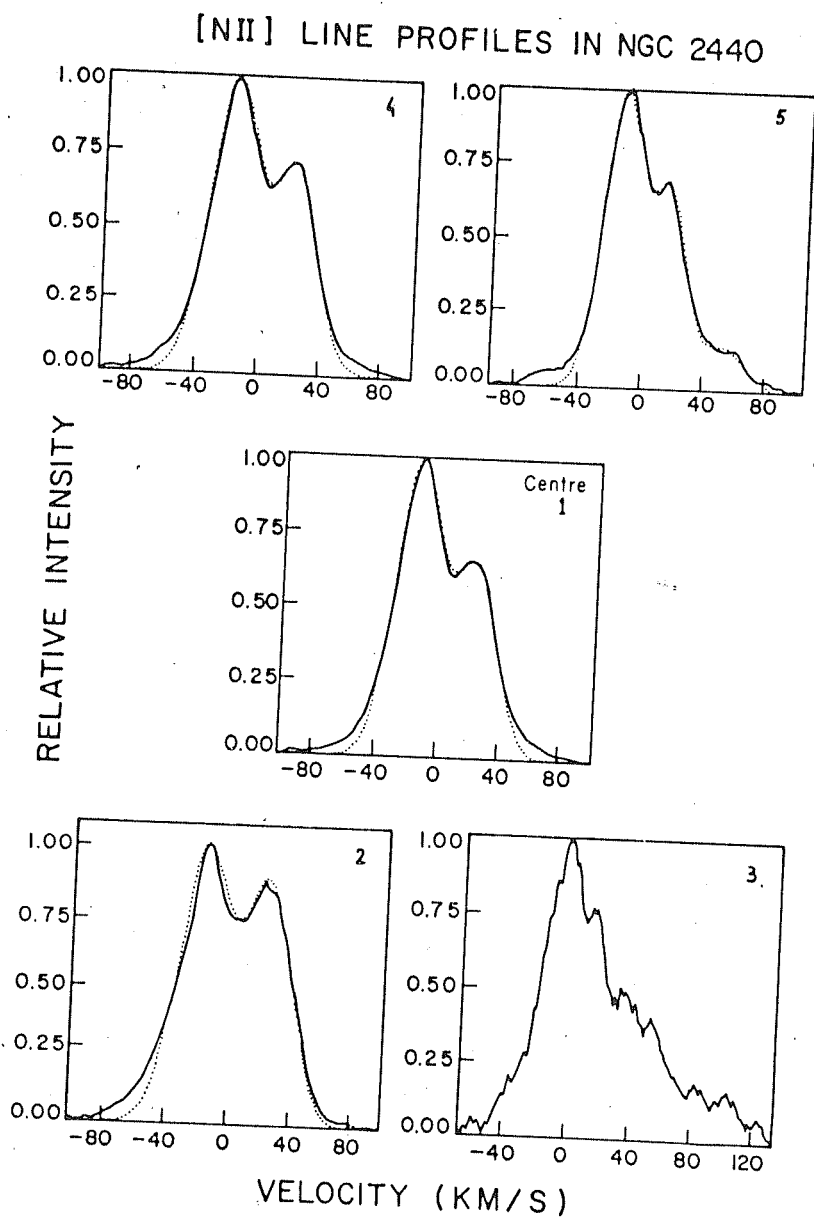
Fig.4.4: The [NII] 6584Å line profiles in NGC 2440.The observed profiles (indicated by the continuous lines) have been fitted by multi-component Gaussians (refer text) indicated by the dotted lines. The position on the nebula to which each line profile corresponds is also indicated.
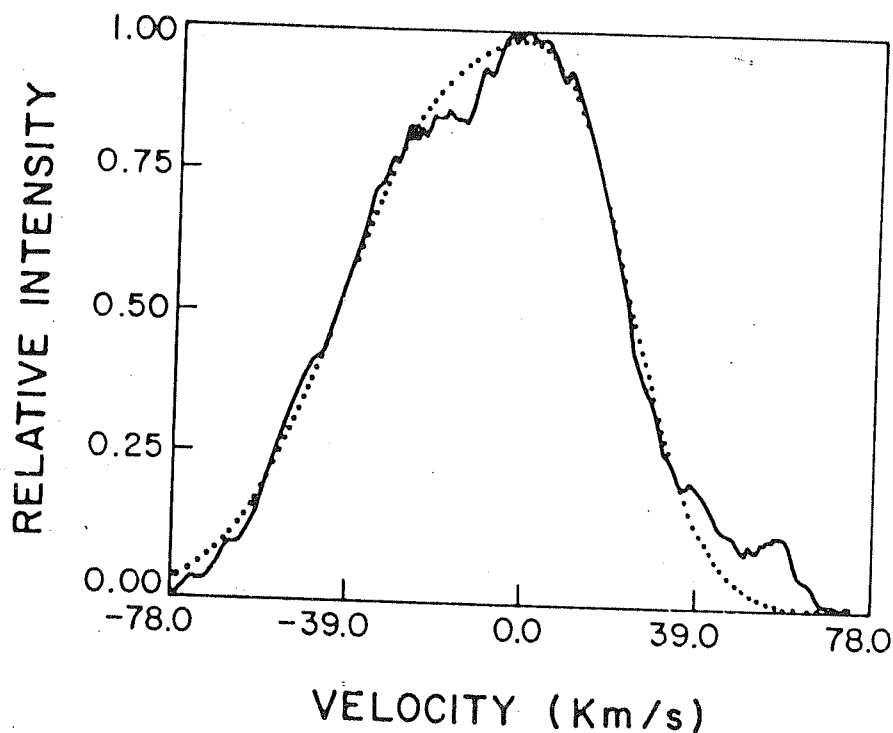
Fig.4.5: The Hα 6563Å line profile in the central region of NGC 2440. The observed profile (indicated by the continuous line) has been fitted by a double-component Gaussian indicated by the dotted line.

The exceptions are in the case of the [NII] profiles in the position 5 where three gaussians had to be fitted and in position 3 where we have not made any gaussian decomposition due to the rather complicated structure of the profile. We present in Table 4.2 the main results obtained from the analysis of the profiles.

Table 4.2

Emission line characteristics in NGC 2440

Emission Line	Position on nebula	Widths(W) and intensities(I) of individual components						V_{exp} (Km/s)
		W_1	W_2 (km/s)	W_3	I_1	I_2	I_3	
[OIII] 5007Å	1	38.8	34.0		0.95	0.73		17.5
	4	35.4	35.4		0.82	0.77		19.0
	5	33.6	29.2		0.97	0.74		17.0
	6	29.7	36.5		0.97	0.35		18.5
	7	36.0	29.1		0.98	0.80		17.5
[NII] 6584Å	1	33.4	32.1		0.97	0.61		19.0
	2	37.6	35.9		0.97	0.83		20.8
	4	37.4	31.9		0.97	0.66		20.3
	5	29.2	26.5	31.1	0.96	0.60	0.11	15.3*
Hα 6563Å	1	53.9	35.1		0.85	0.50		15.0

* Vexp has been measured between the two stronger components.

4.2.5 Discussion of the results :

The central region V_{exp} values in both [NII] and [OIII], indicated in section 4.2.2, agree reasonably well with those measured by other observers. The [NII] expansion velocity, is on an average, slightly larger than the [OIII] expansion velocity. This suggests that there is a stratification of the ionic species in this nebula. Further evidence for stratification may also be seen from a comparison of the [NII] and [OIII] profiles obtained for the same region of the nebula. The common positions are 1,4 and 5 although unfortunately the SNR in the [OIII] profile for position 4 is poor and a comparison with its corresponding [NII] profile is not very meaningful. However, a comparison in the remaining common positions 1 and 5 shows that the line shapes are significantly different and so are the ratios of the intensity of the blue and red components for the two lines. This suggests considerable stratification in the object. KA (1974) have also arrived at a similar conclusion based on the observation that the level of excitation varies considerably over a small extent of the nebula.

There also appears to be evidence for a tilt to the nebula based on the [NII] observations. The line profiles obtained in the eastern side of the nebula are marginally offset by ~ 2.0 and 1.5 km/s respectively with reference to the line profile in the central region. In comparison, the profile in position 3, obtained from the west side of the nebula shows a significant and noticeable shift towards the red with respect to the line profile in the central region. However, the profile in position 5,

although on the west side, is blue shifted by ~ 1 km/s with respect to the centre. One may therefore infer tentatively that along the NS direction (i.e. along the line joining positions 1,2 and 3), the two lobes of the nebula appear to be tilted. However, in the [OIII] profiles we did not find any tendency or indication showing that the two lobes of the hour-glass structure are tilted with respect to the line-of-sight. This difference in the kinematic behaviour of the [OIII] and [NII] ions again suggests stratification of ionic species in the nebula. Further as may be seen from the Table 4.2, there is not much of a variation of the expansion velocities in the different positions in both the [OIII] and [NII] lines. There is also a general indication showing that the expansion velocity of the outer regions tends to marginally increase vis-a-vis the expansion velocity of the central region. This is true in the majority of the positions observed. What is important is that a general decrease in expansion velocity, as would be expected in the case of a spherical shell, is not seen as one moves away from the centre of the nebula. The kinematic features discussed above along with the slit spectrographic images of the object obtained elsewhere provide a framework for constructing a spatio-kinematic model for NGC 2440. Such a model is discussed in the next section.

4.2.6 A spatio-kinematic model for NGC 2440 :

Evidence for the tilt of the hour-glass lobes, as tentatively found in our data, is clearly seen in the echelle spectrograph images of the object taken by IPB (1989). The above authors have obtained slit images of NGC 2440 in [NII] and Hα in

four positions. The slit positions are 6" South, 8" South and 4" North of the central star and one through it. In each of the above positions the slit was oriented in the east-west direction (it may be repeated that the hour-glass lobes are also oriented in the EW direction). We present in Fig. 4.6 the slit images of NGC 2440 as obtained by IPB (1989).

The most interesting and unusual feature is the flattened figure-of-eight appearance of the images. This kind of a line shape, as mentioned earlier, was also obtained by HW(1987). The second important feature that may be noticed is the backward slant or tilt of the slit image. The flattened figure-of-eight appearance coupled with the morphology of the nebula suggests that the hour-glass lobes of the nebula may reasonably be approximated by two intersecting spheroidal shells. The tilt of the slit image also suggests that the hour-glass lobes are tilted out of the plane of the sky i.e., the line passing through the centre of the two lobes and through the central star (which we henceforth call the axis of symmetry) does not lie in the plane of the sky.

In constructing a spatio-kinematic model we have made a simplifying assumption that the two intersecting hour-glass lobes are spherical in form. This assumption agrees reasonably well with the apparent shape of the lobes as seen in Fig. 4.1. We show in Fig. 4.7 a schematic representation of the geometry of the model chosen for the nebula. The origin of the reference axis has been chosen symmetrically between the centres of the two intersecting spherical lobes of the nebula which lie at "a" and "-a" respectively. The axis of symmetry (as defined earlier) has been taken along the Y-axis. The tilt angle of the nebula ϕ is
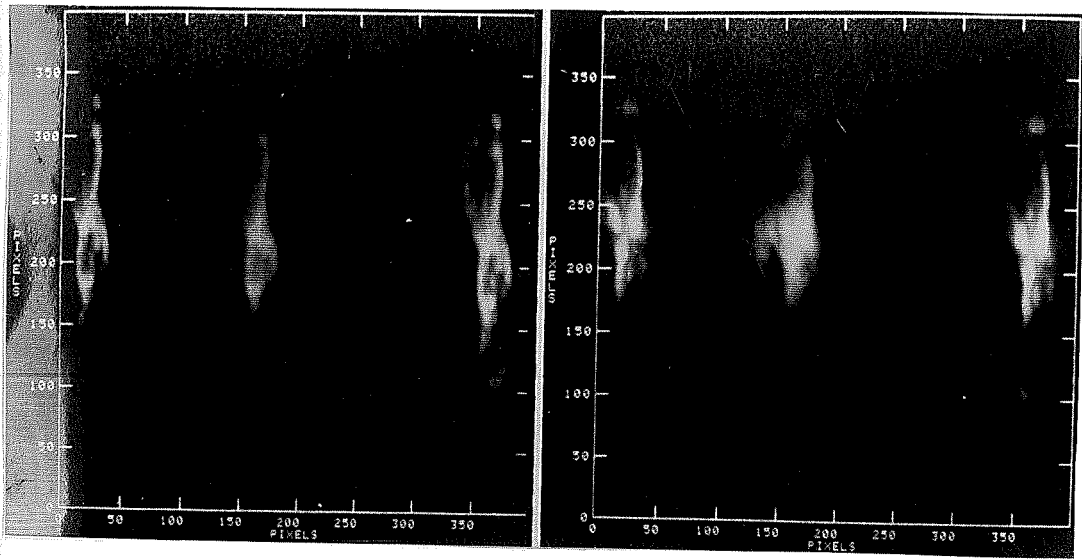
Fig.4.6:   The echelle slit spectra obtained in NGC 2440 by Icke,
Preston and Balick (1989) for two slit positions viz. through the
central   star   (corresponding   to   the   right   hand   diagram)   and   8″
South   of   the   central   star   (left   hand   diagram).   In   both   the
positions the slit is oriented along the East-West direction.
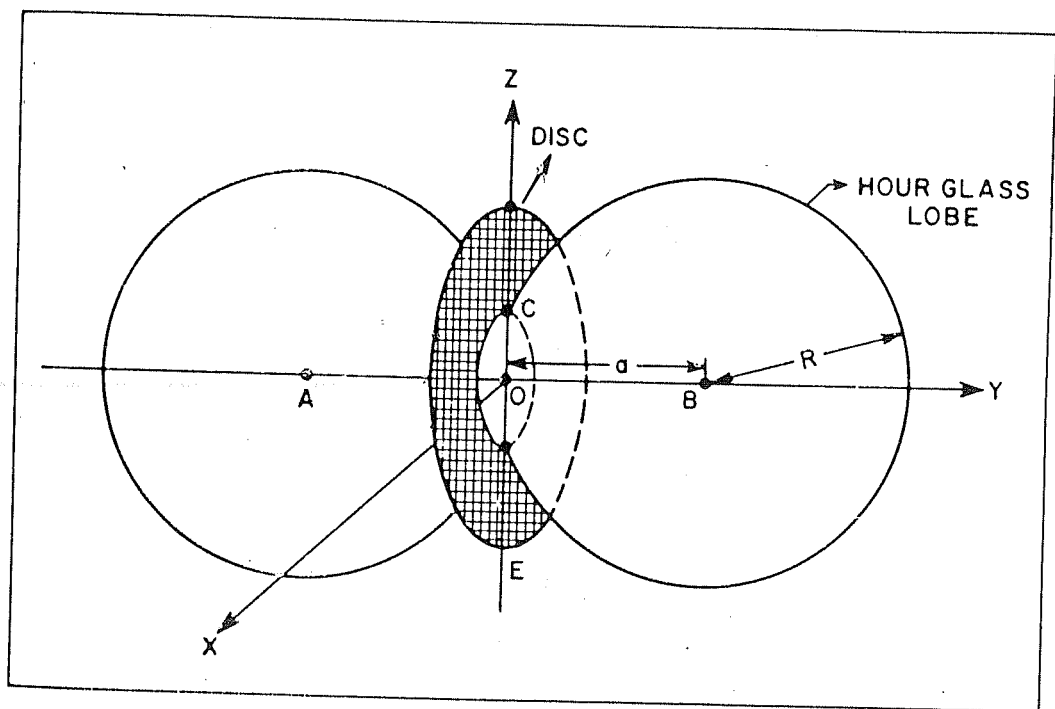
Fig. 4.7: The morphological model chosen for NGC 2440 for the purpose of deriving its spatio-kinematics.

described through $\phi = 90 - \theta$, where θ is the angle between the line-of-sight and the axis of symmetry. A tilt angle value of $\phi = 0^0$ means that the axis of symmetry lies in the plane of the sky. We have also shown in Fig.4.7 a circular disc of matter at the plane of intersection of the two hour-glass lobes. We will discuss this aspect in greater details later in this section. At present we consider only the hour-glass structure in our model.

With reference to the geometry described above the surface of the hour-glass structure is defined by the equation

$$x^2 + (y \pm a)^2 + z^2 = R^2 \tag{4.1}$$

where R is the radius of each lobe. The positive sign in eqn. 4.1 is to be taken for regions where $y < 0$ and the negative sign for regions where $y > 0$. In eqn. 4.1, $a < R$ since we assume that the lobes intersect. To measure the extent to which the waist of the nebula is pinched, we use a term a called axial ratio. This parameter is defined as the ratio of the radius of the nebular waist to the radius R of the individual lobes. From Fig. 4.7 we have

$$\text{Axial ratio} = \frac{\sqrt{R^2 - a^2}}{R} \tag{4.2}$$

For $R = a$ the two spherical lobes just touch and the axial ratio is zero.

The expected slit image for the hour-glass structure may then be constructed by the following method which is briefly outlined. Consider for example that the slit is positioned along the Y-axis i.e., it passes through the central star.

118

Consider further a line-of-sight passing through a particular point of the slit along the slit length. This line-of-sight, except at the extremities of the nebula, would intercept two points on the hour-glass form. These two points may lie on a single lobe or on different lobes depending on the tilt assumed for the nebula. For a zero tilt i.e., $\phi = 0^0$, the two points would always lie on the same lobe. For the given geometry defined in eqn. 4.1, and for an assumed value of ϕ the radial distance of the two intercepted points from the central star was determined. If it is assumed that every point of the nebula is expanding radially and the velocity of expansion is proportional to the distance i.e., $V = \alpha\ r$ then the expansion velocities of the two points under consideration can be calculated since the radial distances are known. The expansion velocities calculated in the above manner were then projected along the line-of-sight to give the expected observed expansion velocity. This procedure was then repeated for all lines-of-sight along the slit length thereby generating the slit image.

We show in Fig. 4.8 the slit images, generated by the above method, for two positions of the slit. The first image (left hand side diagram of Fig. 4.8) is for the slit positioned along the Y-axis. The second image is for the slit positioned parallel to the Y-axis but shifted upwards so that it passes through the point where the two shells intersect the Z-axis (denoted by point C in Fig. 4.7 and hereafter referred to as the 'cusp'). These two positions of the slit were chosen because the model images can be compared with IPB's (1989) observed slit
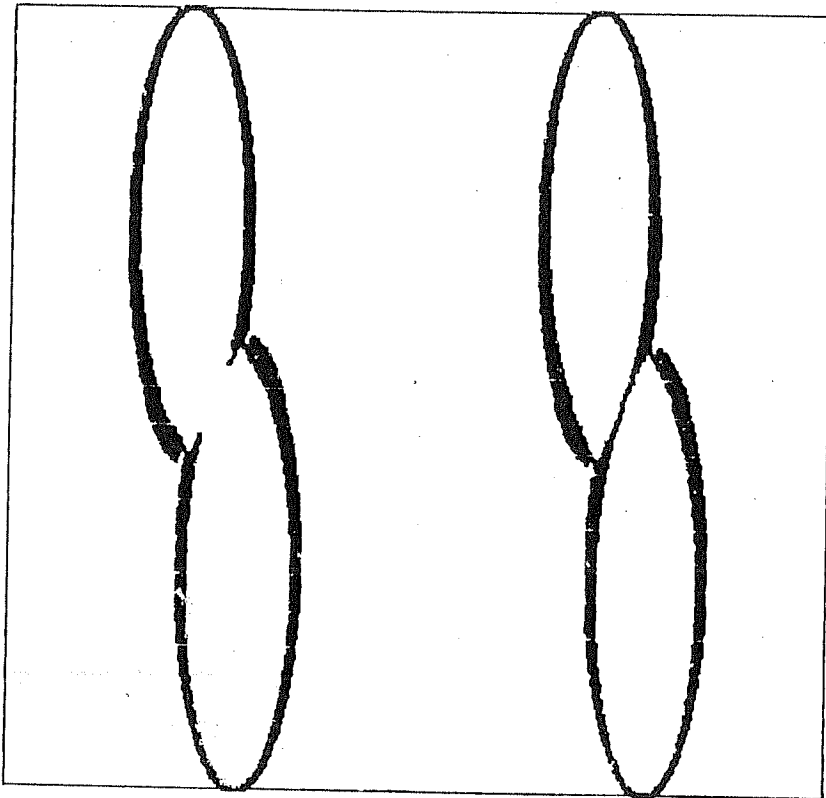
Fig. 4.8: The model slit spectra obtained for the hour-glass lobes of the geometrical form considered in Fig. 4.7. The left hand diagram is for the slit passing through the central star and oriented along the Y axis and the right hand diagram is for the slit positioned across the 'cusp' (refer text) and also oriented along the Y axis.

images which are available in similar positions. The images in Fig. 4.8 were computed for a tilt angle $\phi = 30^0$ and an axial ratio of 0.55 (R = 6 units, a = 5 units). This value of axial ratio was chosen since the shape of the nebula with this choice appears to match closely the morphological appearance of NGC 2440 (as can be judged from CCD / photographic images of the object). As may be seen, the model images (Fig. 4.8) compare well with the observed images (Fig. 4.6). The flattened and distorted figure-of-eight line shape (which is rather unusual in PNe) is reproduced successfully along with the backward slant of the entire image. It may be mentioned that these two features are not special to the particular choice of the axial ratio and of the tilt angle ϕ made here. The figure-of-eight appearance is reproduced for the other values of the axial ratio also but the backward slant always requires that ϕ be not equal to zero i.e., a tilt must be present. For the particular choice of the geometry for our model, we find that a choice of ϕ in the range 15^0 to 30^0 simulates the observed slit images well.

A few other points regarding the model slit images may be mentioned. A comparison between the model images on the left hand and the right hand side of Fig. 4.8 shows the appearance in the latter of a central slanting bar joining the two loops of the figure-of-eight. A hint of this bar is seen in the former model image. This bar actually gradually develops as the slit position is stepped upwards, across the face of the nebula (or downwards also in our model since the geometry is symmetric) and becomes a complete bar when the position of the 'cusp' is reached. A similar behaviour is seen in the observed slit images of Fig.

121

4.8. The slanting bar is missing in the images taken with the slit position through the central star but is prominent in the 8"S image. It should be mentioned here that the widths of the individual blue or red components in the model images of the Fig. 4.8 are a consequence of assuming a thickness for the shell which would have a spread in velocity governed by the $V = \alpha\ r$ relationship. In the slit images presented in Fig. 4.8 we have assumed a shell with a thickness of 0.13 R. We have not included the effect of thermal broadening or broadening due to turbulence if present in the shell and therefore the widths shown here will be on the smaller side than the true widths and are not realistic. However, our intention was primarily to see whether the simple model considered here can reproduce the shape and the tilt of the observed slit images. Another aspect which is seen from the model images is that the expansion velocity does not decrease rapidly along the slit length (as would be expected in a spherical PN for example). As may be seen the expansion velocity maintains an almost constant value over a rather large extent of the nebula. In fact we find that if the tilt angle is chosen to be smaller i.e., $\phi = 10$ to 15 ^{0}, then the expansion velocity can even increase as one moves away from the centre of the nebula. This behaviour of the expansion velocity is in line with our observed expansion velocities which also seem to indicate that V_{exp} does not decrease (and may even perhaps increase) in the outward regions of the nebula.

The model proposed above, however, is unable to reproduce the finer features of the observed slit images (given in Fig. 4.6) like some additional velocity components that may be

seen in the above Fig. 4.6. These components may be due to the condensations seen near the centre of the nebula. Alternatively they may be due to the elliptical disc seen across the face of NGC 2440. In the absence of kinematic data for this disc, it is difficult to establish whether it is truly elliptical or a tilted circular disc seen in projection. However, the orientation of the disc with respect to the hour-glass lobes suggests that it is approximated by the former geometrical form. We have attempted to incorporate the kinematics of the disc by assuming it, for simplicity, to be annular and circular in shape and also thin in extent compared to the dimension of the nebula. In Fig. 4.7 the disc lies in the XZ plane with its centre at the origin. The inner radius of the annular disc coincides with the waist of the hour-glass structure and the disc extends to its outer radius D. If the kinematics of the disc is governed by a similar $V = \alpha'r$ relationship as for the hour-glass shell then two additional components appear in the original slit image (refer Fig. 4.9). The position of the two velocity components depends on the value of α' (in the $V = \alpha'r$ relationship for the disc) compared to the value of α (in the $V = \alpha r$ relationship for the hour-glass lobes). In general the two components due to the disc start from the two cusps near the waist of the figure-of-eight (refer Fig. 4.9). They then extend up and down respectively but at a slightly inclined angle (which depends on the tilt assumed for the nebula). The extent of these two components depends on the radius D assumed for the disc. In Fig. 4.9, we have shown the positions of the disc components for values of $\alpha' = 0.2, 0.4,$ and o.8 times α. In each diagram of the above figure a value of $D = 7.0$ units was chosen.
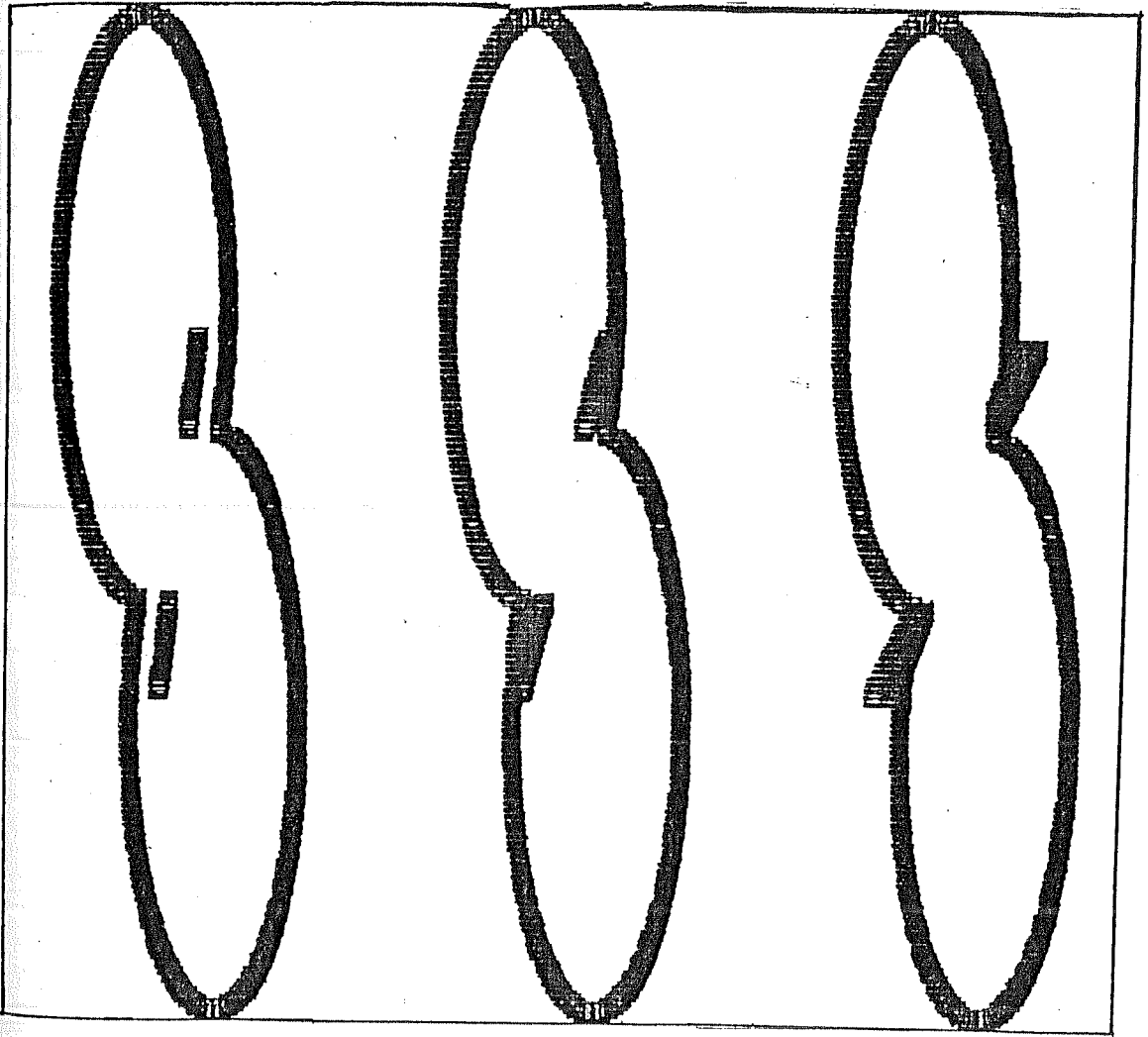
Fig. 4.9: The model slit spectra obtained for the geometrical form of Fig.4.7 by considering both the hour-glass lobes and the central circular disc. In each of the three model images shown, the slit is positioned through the central star and oriented along the Y axis. The geometrical parameters for the hour-glass lobes are the same as considered in Fig.4.8 ie. R=6.0 units and a=5.0 units. The disc diameter is equal to 7 units in each of the three diagrams. In going from left to right (in the 3 diagrams) the values of α' are 0.2, 0.4, and 0.8 times α respectively.

The parameters for the hour-glass lobes were as mentioned before i.e., $\phi = 30^0$, R = 6.0 units and a = 5.0 units. Fig. 4.9 may be compared with the observed slit images in NGC 2440 to see whether a better agreement has been obtained by including the kinematics of the disc. It appears to us that for values of α' small compared to α, a better agreement is obtained between the model and observed slit images. It may be quite reasonable to expect that the disc expands slower than the hour-glass lobes (i.e., $\alpha' < \alpha$). In fact as mentioned earlier, HW(1987) have found that the elliptical disc displays only low velocity motion compared to the hour-glass lobes. However, since the disc parameters (like thickness, size etc) cannot be estimated or ascertained with accuracy, the above exercise must be treated as a qualitative estimate of the kinematic contribution of the disc to the slit images. It may be mentioned that if the disc is assumed to be elliptical instead of circular as considered in our model, then a tentative exercise indicates that the model slit images are grossly similar to those reproduced in Fig.4.9.

4.2.7 Conclusions regarding the kinematics of NGC 2440 :

Based on our observations and the proposed spatio-kinematic model for NGC 2440, the following important conclusions may be drawn:

(i) Our observations indicate that there is a velocity gradient in the nebula with the outer regions (i.e., regions more distant from the central star) expanding faster than the inner regions. This behaviour of the velocity field is also evident in the echelle slit spectra of the object obtained by other observers.

(ii) There is an indication from our observations that the two hour-glass lobes of the nebula do not lie in the plane of the sky but are tilted with respect to the line-of-sight.

(iii) The spatio-kinematics of NGC 2440 may be quite successfully explained by a model proposed here for the nebula. In the model, the geometrical form chosen for the nebula consists of a circular disc of ionized matter located at the plane of intersection of two spherical shells - a configuration which is in reasonable agreement with the morphological appearance of NGC 2440. The observed velocity field in the nebula is reproduced well in the model by assuming that the nebula is tilted out of the plane of the sky by an angle which cannot be determined precisely but is in the range of 15^0 to 30^0 and also that the velocity field in the nebula follows a $V = \alpha r$ relationship. The model also predicts a steeper $V = \alpha r$ relationship for the lobes than for the disc.

4.2.8 Formation mechanism for NGC 2440 :

The rather complicated morphology of NGC 2440 and its remarkable kinematics need to be fitted into a general mechanism for PNe formaton. Some of the questions that may be raised are whether a single mechanism can satisfactorily produce both the hour-glass lobes as well as the elliptical disc that comprise the global morphology of NGC 2440. Also how successfully does the above mechanism reproduce the observed kinematics of NGC 2440. We defer discussions on these aspects for the present moment and consider them later in Chapter V.

4.3 NGC 2346 :

4.3.1 Introduction:

NGC 2346 (Perek and Kohoutek number 215 + $3^0$1, R.A. (1950) =7^h 06^m 49^s, Dec = -0^0 $43'$ $29''$) is another complex PN which has not been well studied. Morphologically it has a bipolar hour-glass structure with a total extent of $\sim$ $70''$ (Cohen and Barlow, 1975) oriented approximately in the North-South direction with a narrow waist oriented along East-West. We present a photograph of the object in Fig.4.10. In CCD images of the object given in Balick (1987) the central waist appears as a tilted ring of approximately $15''$ radius surrounding the central star. Bright condensations and knots are also seen along the waist. Molecular hydrogen emission at 2.122 μm from the v = 1 → 0 S(1) vibrational transition has been detected in this PN (Zuckerman and Gatley, 1988) and shown to follow the distribution of the ionized gas. Evidence has also been found by these authors for a dense torus of molecular Hydrogen surrounding the central star of the PN and lying in a direction perpendicular to the orientation of the optical bipolar lobes. Similar evidence for a dense torus has also been found in the CO emission from the nebula by Healy and Huggins (1988).

The detectable central star has been found to be of type A 0III by Kohoutek and Senkbeil (1973) and of type A5V by Mendez (1978). To account for the high excitation spectrum of NGC 2346 it was first suggested by Kohoutek and Senkbeil (1973) that
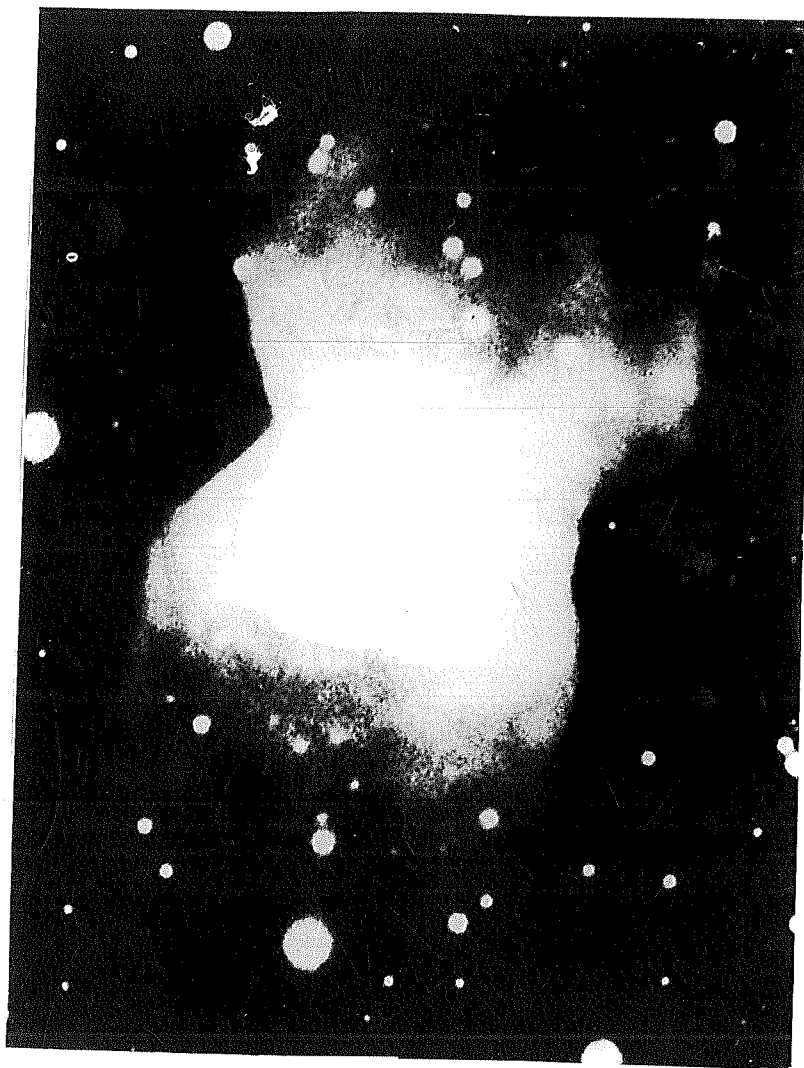
Fig. 4.10: An image of NGC 2346 by Kohoutek and Lausten as reproduced in the Proceedings of IAU.Symp.76, 1978,"Planetary Nebulae", ed. Y. Terzian, p.329. North is to the top and East is to the left.

the A type central star must have a hot subdwarf companion. Observations of the central star have confirmed that it is a single lined spectroscopic binary with a period of sixteen days (Mendez and Niemala, 1981). Since 1981, photometric observations of the central star have revealed periodic variations in the light curve (Mendez et al 1982, Kohoutek 1983, Roth et al 1984, Schaeffer 1985) and subsequent observations (Acker and Jacniewicz, 1985; Jacniewicz and Acker, 1986) have further shown a dephasing of the light curve. The photometric variations and the subsequent dephasing of the light curve have been explained to be due to the passage of a clumpy dust cloud(ejected by the hot sub-dwarf companion) across the orbit of the central A type star (Mendez et al 1982; Jacniewicz and Acker, 1986)

4.3.2 Previous kinematic studies of NGC 2346:

At the commencement of this work the only existing kinematic observations of this PN were by Walsh (1983). Walsh has observed the nebula using a slit spectrograph orienting the slit along the North-South direction and has obtained [NII] and Hα line profiles along three parallel directions separated by 15" from each other. He has determined a central region expansion velocity of 14 km/s in the [NII] line. His radial velocity measurements also show the presence of secondary structures and wings in the line profiles. Recently Icke, Preston and Balick (1989) have also obtained slit spectra of NGC 2346 in the [NII] and Hα lines. As may be noted, no [OIII] observations had previously been made on this object.

4.3.3 Observations and results:

Observations in the Hα 6563Å and the [NII] 6584Å lines were made using a field aperture of 30" centred on the object. In the [OIII] 5007Å line the object was studied in three different positions. In each position an aperture of 15" was used. The positions observed are as follows: (i) the central region of the nebula designated as position 1; (ii) Position 2 in the northern lobe of the nebula placed 10" away from the centre and at a position angle of 15° and; (iii) Position 3 placed symmetrically opposite to position 2 at a distance of 10" from the centre and in the southern lobe. These positions are shown in Fig. 4.11 along with the slit positions of Walsh's observations which are required for discussions at a later stage.

In the central region, 8 scans in [OIII], 4 in [NII] and 3 scans in Hα were obtained. Co-adding of the scans was done to improve the signal-to-noise ratio which ranged typically between 5 to 7 at the peak of the profiles. In position 2 of the [OIII] line two scans were obtained which were co-added. In position 3 although two scans were taken, the data obtained were not reliable due to fluctuating sky conditions and hence they are not presented here.

4.3.4 Kinematic results in NGC 2346:

The resultant profiles in the central region for the [OIII], [NII] and Hα lines are shown in Fig. 4.12(a), 4.12(b) and 4.12(c) respectively. The [OIII] profile in position 2 is shown in Fig. 4.13. The [OIII] profiles showed a well-defined separation between the blue and red components associated with an
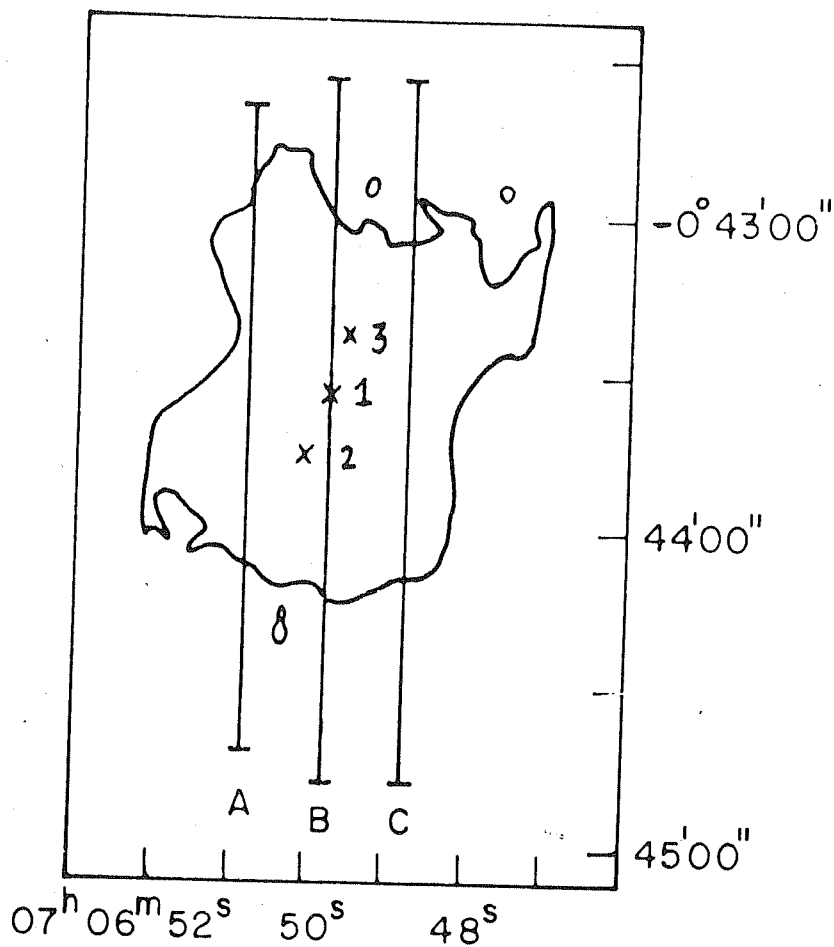
Fig. 4.11: A sketch of NGC 2346 (from Walsh,1983) indicating the positions where the present observations were made (marked 1,2,3). The signal-to-noise ratio at position 3 was inadequate for analysis. Also indicated are the slit positions A, B, C along which Walsh's (1983) observations were made.
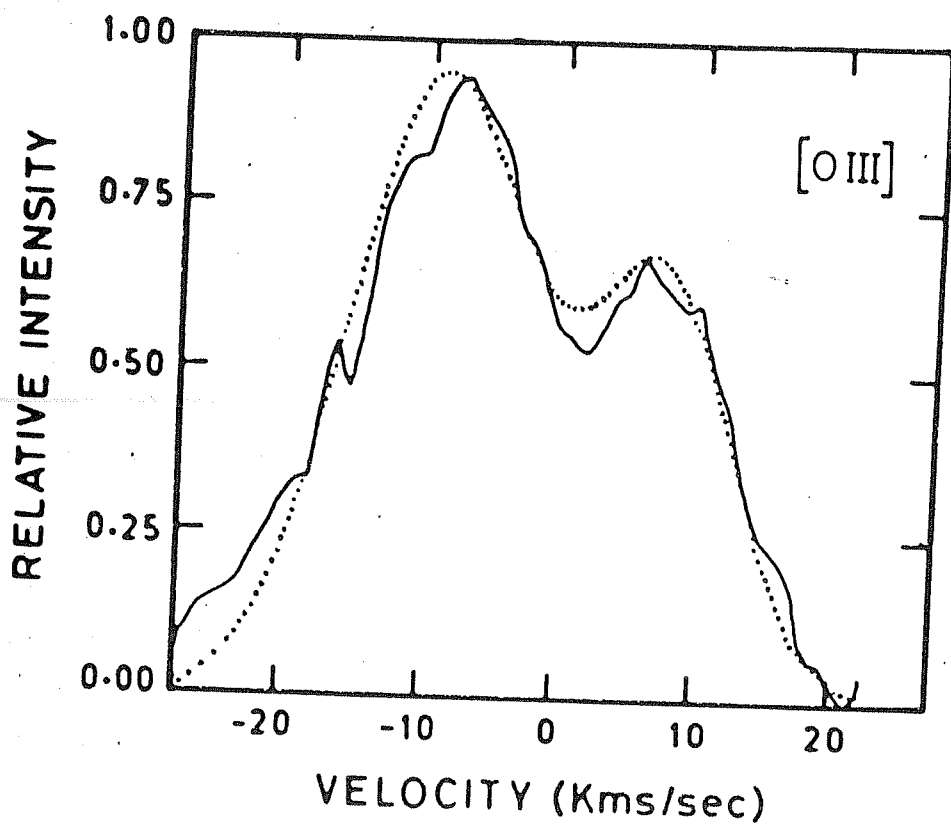
Fig. 4.12(a): The [OIII] 5007Å line profile in the central region of NGC 2346. The observed profile (indicated by the continuous line) has been fitted by a double-component Gaussian indicated by the dotted line.
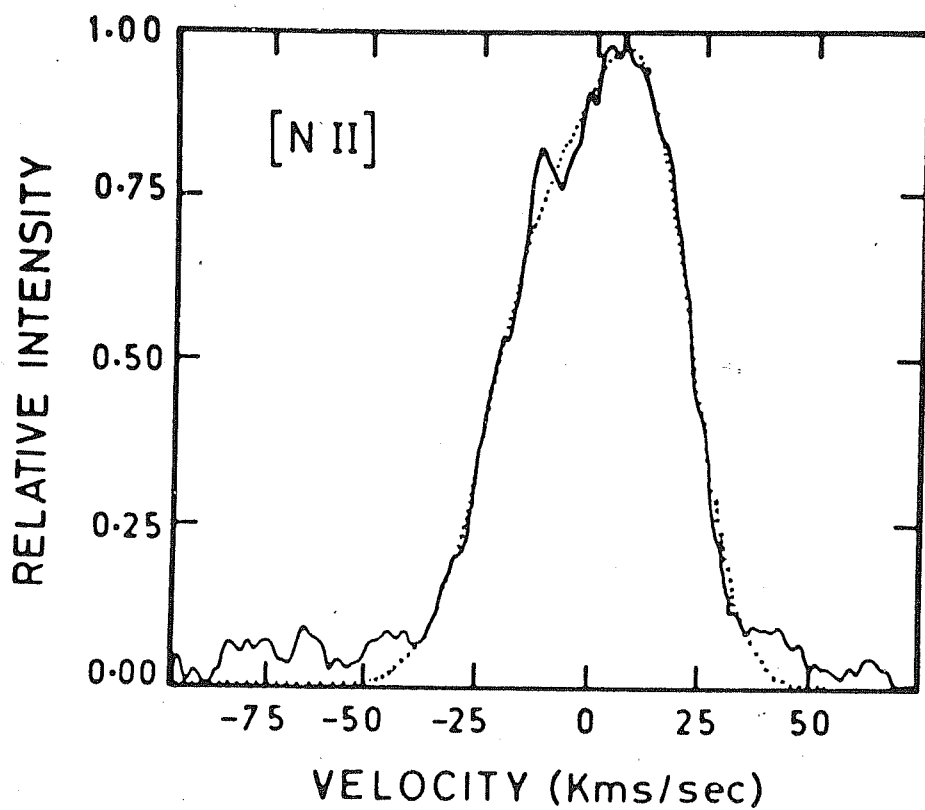
Fig. 4.12(b): The [NII] 6584Å line profile in the central region of NGC 2346. The observed profile (indicated by the continuous line) has been fitted by a double-component Gaussian indicated by the dotted line.
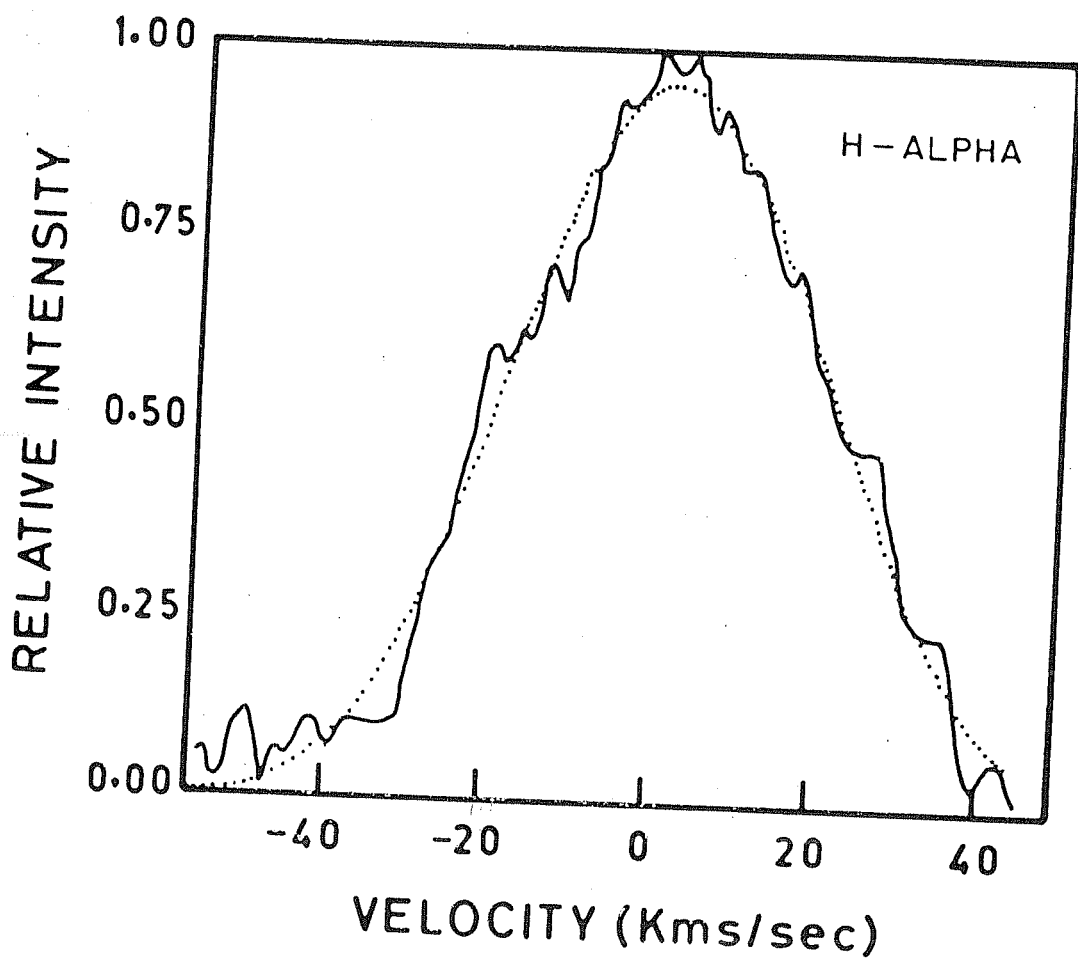
Fig. 4.12(c): The Hα 6563Å line profile in the central region of NGC 2346. The observed profile (indicated by the continuous line) has been fitted by a double-component Gaussian indicated by the dotted line.

expanding shell. In the case of the [NII] profiles, although a well resolved split is not clearly indicated, a pronounced suggestion of a split (at the point of inflection at ~ -7.0 km/s) was obvious in all the scans. Due to a larger thermal broadening than the other two species, the profiles of Hα did not show any split. All these profiles are fitted by a two-component gaussian. In table 4.3, we give the profile parameters obtained in the central region of NGC 2346 in the different lines from the Gaussian decomposition. The [OIII] line profile in position 2 could not be simulated by a double gaussian fit specially at the wings and had to be fitted by a four component gaussian. This profile shows the presence of two weak components in the wings separated by 53 km/s and two stronger central components separated by 15 km/s.

Table 4.3

Emission line parameters in NGC 2346

Emission line	Width of first gaussian (km/s)	Relative intensity of first gaussian	Width of second gaussian (km/s)	Relative intensity of second gaussian	Vexp (km/s)
[OIII] 5007Å	15.70	1.00	11.70	0.66	8.00
Hα 6563Å	34.70	0.82	36.40	1.00	10.0
[NII] 6584Å	29.00	0.77	26.00	1.00	11.0
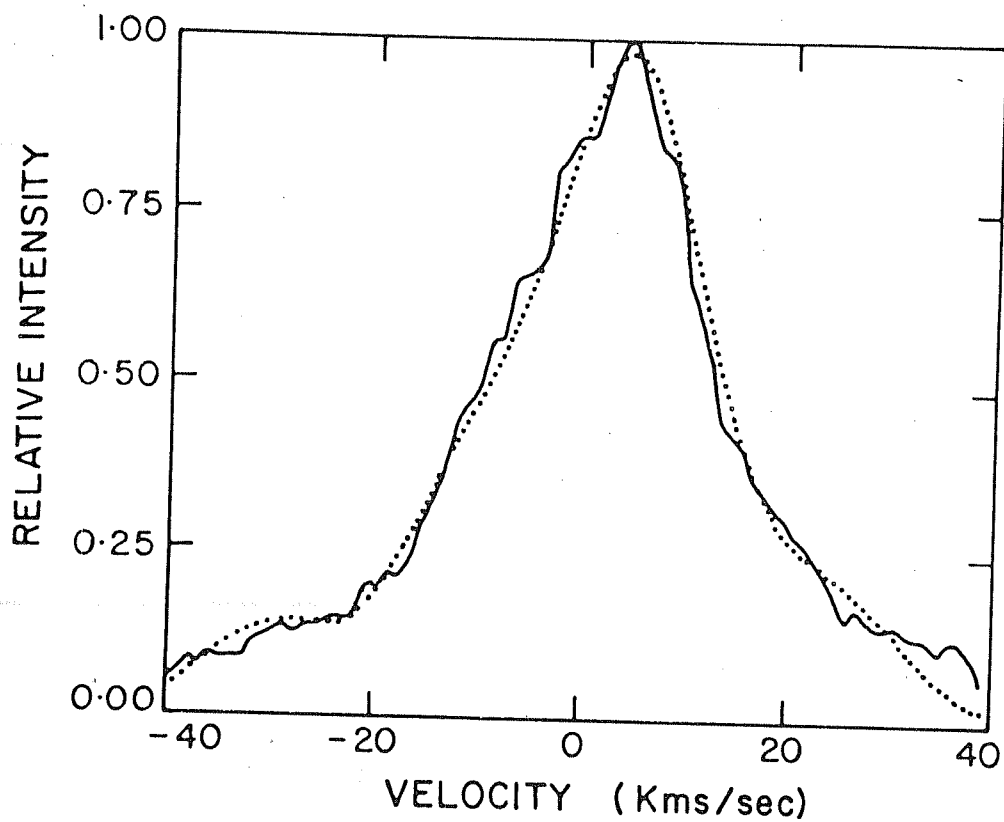
Fig. 4.13: The [OIII] 5007Å line profile in position 2 (refer Fig. 4.11) in NGC 2346. The observed profile (indicated by the continuous line) has been fitted by a four-component Gaussian indicated by the dotted line.

The [NII] expansion velocity obtained by us in the central region tallies well with (V_{exp})[NII] = 14 ± 4 km/s measured by Walsh(1983). Assuming that the [NII] line arises from the outer regions of the nebula and the [OIII] line from the inner regions, the difference found from our observations in the expansion velocities in these two lines would imply an outward gradient in V_{exp}. We have estimated the ion temperature following the method suggested by Courtes, Louise and Monnet(1968) which has been outlined in Chapter III (section 3.5). We have obtained an ion temperature(averaged for the red and blue components) of T= 10650 ± 2950 ^{0}K. The error indicated represents the uncertainty in determining the widths of the profiles by the gaussian-fitting procedure. The turbulent velocities turn out to be almost the same for the blue and red components, the average value being 16 ± 2 km/s. It may be noted here that Sabbadin(1976) had evaluated the electron temperature to be 14200^{0}K from the [NII] line ratios.

4.3.5 Spatio-kinematics and intensity distribution in NGC 2346:

The radial velocity measurements in the [NII] line by Walsh (1983) reveal three interesting features in NGC 2346:(i) The profiles are split into distinct red and blue components only south of the central star for slit position A and only north of the central star for slit position C (refer Fig. 4.11). At slit position B, splitting of the line occurs almost symmetrically about the central star position; (ii) There is an abrupt changeover in the relative intensities of the blue and red components around the nebular waist in the middle of which the

central star is located. In slit position A, the red component is brighter than the blue and the reverse occurs along slit-length C. At slit position B, the red component is more intense south of the waist. Above it a reversal occurs with the blue component being stronger than the red and; (iii) there is a tilt to the velocities which can also be seen in the slit image given by Icke, Preston and Balick (1989).

The morphological similarity between NGC 2346 and NGC 2440 (both being hour-glass figures) as well as the common feature of a tilt being present in both their radial velocity profiles, suggest that a model for NGC 2346 should be along similar lines as the one constructed for NGC 2440. We propose a morphological model of this type for NGC 2346 and indicate how it may account for the features (which were mentioned in the preceding paragraph) of Walsh's observations.

4.3.6 A morphological model for NGC 2346

The splitting of the [NII] radial velocities all along the length of the nebula in the N-S direction has been explained by Walsh by assuming the nebula to be in the shape of an elongated cavity or tube. The changeover in brightness of the positive and negative [NII] components north and south of the waist has been attributed to a difference in density of the nebular matter along the line-of-sight(since $I \propto N_e^2$ for forbidden and recombination lines). However, the observed features may be adequately explained without taking recourse to density variations by assuming the nebula to be of an hour-glass form(as its appearance suggests) rather than tubular and by also invoking a

particular line-of-sight geometry.

In Fig 4.14 a morphological model of the nebula is presented. A biconical form for the nebula has been depicted, but in essence one can imagine the ends of the shell on each side of the biconical structure to curve around and meet so that an hour-glass form would be produced - similar to the geometrical form considered for NGC 2440. For the purpose of the followig discussion however, the biconical form shown in Fig. 4.14 is sufficient to demonstrate how the observed features in NGC 2346 may arise. Based on the observed tilt to the velocities, it is assumed that the polar axis of the nebula is oriented by an angle θ to the plane of the sky (Fig. 4.14). We also assume that the nebular matter is uniformly distributed in the outwardly expanding and uniformly thick walls of the biconical structure. Then it can be shown that the volume elements of the approaching and receding shells intercepted along the line-of-sight per unit solid angle are related by

$$\frac{V_1}{V_2} = \frac{r_b \cos^2(\phi + \theta)}{r_r \cos^2(\phi - \theta)} \tag{4.3}$$

where r_b and r_r are the distances from the approaching and receding shells to the observer respectively and ϕ is the semi-vertical angle of the conical nebular shell. The intensity of a forbidden line may be written as(see for example Pottasch, 1984)

$$I_{ul} = h\nu_{ul}A_{ul} \int n_u dV \tag{4.4}$$
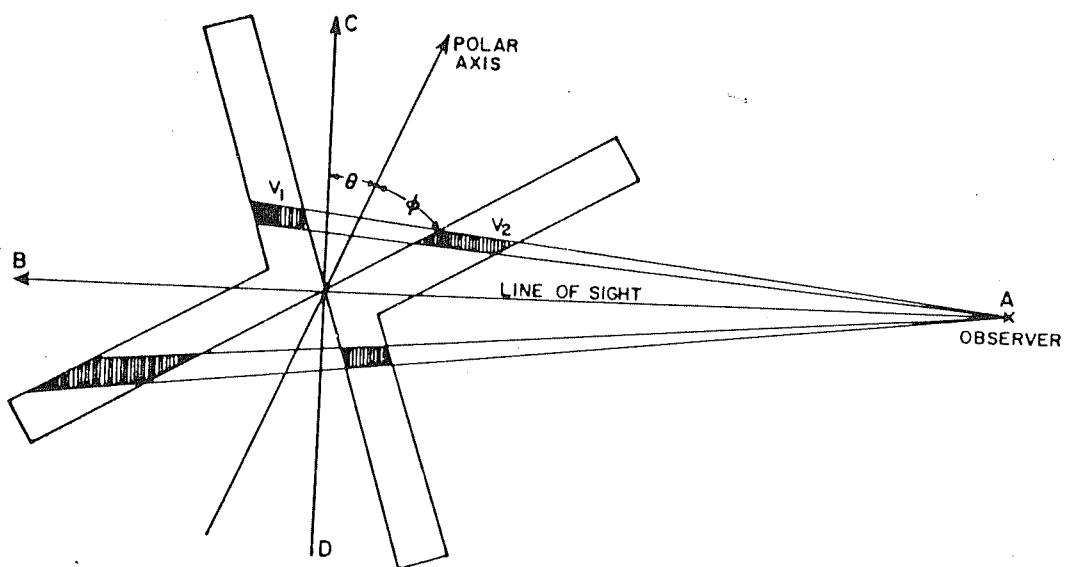
A MORPHOLOGICAL MODEL OF NGC 2346

Fig. 4.14: A schematic representation of NGC 2346 which is assumed to be biconical in structure (with a semi-vertical angle φ) and having its polar axis tilted, by an angle θ, towards the observer.

where A_{ul} is the rate of radiative transitions from an upper level u to a lower level l of an ion whose density is n_u in a volume element dV. It can be seen from eqn. 4.4 that for the same density but different volume elements the observed intensity would be different. By setting $r_r = r_b$ and $\phi = 45^0$ and using eqn. 4.3 it can be seen that the relative intensities of the blue and red components can vary from 2 to 10 for orientations of the polar axis varying from $\theta = 10^0$ to 25^0. For $\phi = 30^0$, we find that the ratio of intensities of the blue and red components vary between 2 and 4 by changing θ from 15^0 to 30^0. A tilt of $\theta = 15^0$ for $\phi = 45^0$ or $\theta = 25^0$ for $\phi = 30^0$ is required to produce the typical ratio of 3 observed by Walsh.

Further, since the polar axis is tilted towards the observer, it can be seen from Fig. 4.14 that for the northern cone the volume element contributing to the intensity is greater for the blue-shifted component than for the red-shifted one. In the southern cone the reverse is true with the volume element of the red component being larger than for the blue component. Thus a switchover of intensity should be found at the waist for slit position B as the observations of Walsh indicate. Also, as the above geometry demands, along slit length A the red component should be brighter in the southern part of the nebula whereas in slit position C the blue component should be brighter than the red as was observed by Walsh. The absence of a secondary component above the waist in position A and below it in position C can be attributed to the tilt of the nebula in the plane of the sky(refer Fig. 4.11) and the positioning of the slit across the nebula. If

the flow is radially outward in the biconical structure, then it can be seen that the northern half of slit length A and the southern half of slit length C are quite close to the edges of the expanding shell. Hence the expansion velocity components would be small along the line-of-sight and be manifested in the absence of line-splitting in these regions. Thus it can be seen that the differences in the relative strengths of the approaching and receding components observed in NGC 2346 may very well be explained by the way in which the nebula is oriented with respect to the line-of-sight.

We end this discussion on NGC 2346 by summarizing the main results and conclusions that have been arrived at.

4.3.7 Conclusions:

(i) Expansion velocities of 8 km/s in the [OIII] line and 11 km/s in the [NII]line are observed in the central region of NGC 2346. An expansion velocity of 7.5 km/s is observed in the [OIII] line in a position $10''$ away from the centre and in the northern lobe. The [OIII] measurements are new for this PN.

(ii) An ion temperature of $10650 \pm 2950^0 K$ and a turbulent velocity of 16 ± 2 km/s are derived from the widths of the $H\alpha$ and [NII] emission lines.

(iii) A morphological model of the nebula is proposed to understand the spatial variations of the relative intensities of the blue and red components observed by Walsh(1983). According to the model, the observed features can be explained by assuming the

nebula to be of an hour-glass shape and tilted towards the line-of-sight.

4.4 NGC 1535:

4.4.1 Morphology and physical properties:

NGC 1535 is a well known planetary nebula (PK number 206 -40^{0}1; R.A.(1950) = 4^h 11^m 57^s; Dec = -12^0 51$'$ 42$''$), having been photographed as far back as in 1918 by Curtis (1918). The nebula consists of a bright inner annular ring, of diameter 20"×17" surrounded by a much fainter outer oval disc of size 48"×42" which is attached to the inner ring. Both these shells are very slightly elliptical with the major axis of the inner ring oriented approximately at position angle 35^0. A photograph of the object is shown in Fig.4.15. This nebula has been classified in the category of PNe with bright double envelopes by Kaler (1974). Chu, Jacoby and Arendt (1987), in their detailed study of multiple shell PNe (MSPNe), have described NGC 1535 as a type IIa MSPN in which the outer shell is " complete and uniform and attached to the inner one". However the classification of NGC 1535 as just a double shell nebula was found to be incomplete and inadequate when Clayton (1988) showed the presence in NGC 1535 of a dense ring of material constricting the inner shell. Detailed spectroscopic observations show a high excitation spectrum for the inner shell (Peimbert and Torres-Peimbert, 1971; Aller and Czyzak, 1979) but the high excitation lines are not prominent in the spectra of the outer shell (Minkowski and Aller, 1956). The IUE spectra of NGC
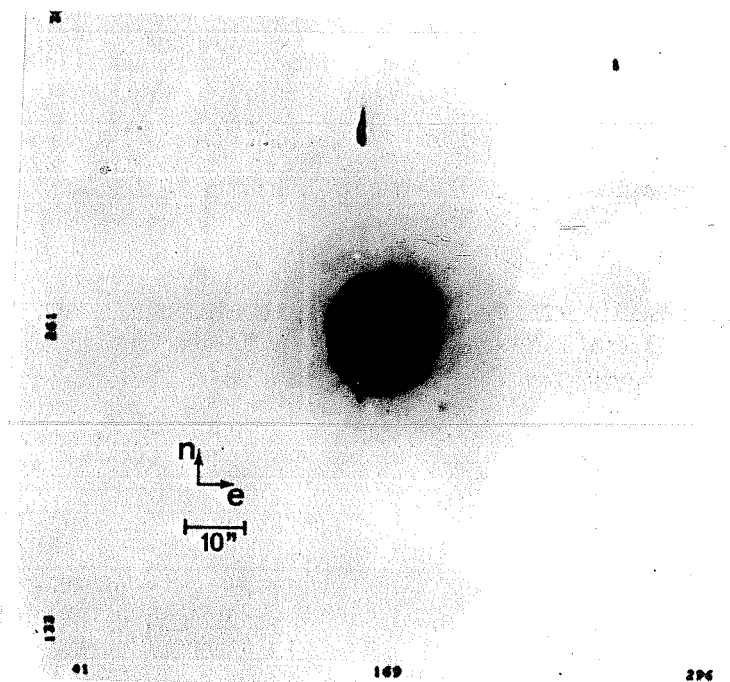
Fig. 4.15:   A CCD image of the multiple shell planetary nebula NGC 1535 in the light of Hα 6563Å (from Louise and Pascoli, 1985).

1535 exhibits prominent P Cygni profiles (Cerruti-Sola and Perinotto, 1985) indicative of mass loss by a fast stellar wind from the central star.

4.4.2 Previous kinematic studies of NGC 1535:

The [OIII] and Hα expansion velocity fields in this nebula have been studied by Sabbadin, Bianchini and Hamzaoglu (1984) using an echelle spectrograph with the slit along position angles of 35^0 and 125^0 respectively. They measure an expansion velocity of 39 Km/s in [OIII] for the central region of the nebula. From the observed velocity field the authors conclude that NGC 1535 consists of two coaxial prolate spheroids of moderate ellipticity with the outer shell expanding marginally slower than the inner one. It may be mentioned here that a prolate spheroid is an ellipsoid of revolution obtained by rotating an ellipse about its major axis whereas an oblate spheroid is generated by rotating the ellipse about the minor axis. Further, these authors also conclude that the angle between the line-of-sight and the major axis of either of the shell is close to 90^0.

Louise and Pascoli (1985) have obtained CCD images of the object and also a high resolution Hα profile of the central region of NGC 1535 which yields an expansion velocity of 38 Km/s. They have proposed a spatio-kinematic model for NGC 1535 in which they show that it is difficult to conclude between a prolate spheroidal (as argued by Sabbadin, Bianchini and Hamzaoglu, 1984, in their model) or oblate spheroidal geometry for the two shells. They infer that the nebula may at best be approximately represented by three-axis ellipsoids. It may be noted that both

the models for NGC 1535, proposed by Sabbadin, Bianchini and Hamzaoglu (1984) and Louise and Pascoli (1985), consider NGC 1535 to be a double shell PN.

However, a detailed study of the kinematics of the inner shell in the [OIII] and Hα lines has recently been carried out by Clayton (1988) using an echelle spectrometer coupled to a two dimensional photon-counting detector system. His investigations indicate a bipolar expansion in the inner shell of NGC 1535 which appears to originate due to the constriction of the inner expanding shell by a torus of dense material. The above results indicate that NGC 1535 cannot be considered as having only two expanding shells.

The expansion velocity in the central region of the nebula is measured consistently to be $\simeq$ 20 Km/s by all observers. From Weinberger's (1989) catalogue on expansion velocities, the different $2V_{exp}$ values measured in NGC 1535 are 40 Km/s in [OIII] (Wilson, 1950), 38 Km/s in different ions (Acker, 1976), 40 Km/s in Hα (Welty, 1983), 40 Km/s in Hα and [OIII] (Clayton, 1988), and 38 Km/s in Hα (Mendez et al 1988; Christiani et al 1989; and Bianchi et al 1989). The V_{exp} values of Sabbadin et al (1984) and Louise and Pascoli (1985) have already been mentioned.

In spite of considerable work done on this object, there was a need to study the object further. At the commencement of this work, the [OIII] velocity information on this nebula was restricted to Sabbadin et al's (1984) results. These authors, as mentioned earlier, have obtained velocity information only for regions of the nebula along position angles of 35^0 and 125^0. In view of the existing disagreement regarding the structure of the

inner shell and the nebula as a whole, it was thought that additional velocity information from regions of the nebula which had not been studied earlier would prove useful in drawing firmer conclusions regarding the structure and kinematics of NGC 1535.

4.4.3 Observations on NGC 1535:

Observations in the [OIII] 5007Å line were made at four positions of the nebula. The positions studied have been marked by the numbers 1 to 4 in Fig.4.16 which gives an approximate schematic representation of NGC 1535. We have, for convenience, shown both the shells to be spherical. Based on the work of Clayton(1988), the approximate position and orientation of the torus constricting the inner shell is also shown (more details on this toroidal ring are given in section 4.4.4).

4.4.4. Model emission line profiles in NGC 1535:

In this section we describe model emission line profiles constructed for NGC 1535 and compare these model profiles with the observed data. The construction and comparison of such line profiles with those observed serve the purpose of checking the validity of the assumptions regarding the physical conditions and the geometrical parameters that have been made in generating the line profiles. To see how a line profile may be constructed, a single line-of-sight passing through the nebula may be considered. Such a line-of-sight passes through a series of regions in the shell. In any one such region, between radial distances r to r+dr measured from the central star to the points in the nebula intercepted by the line-of-sight, the ions would not have a unique
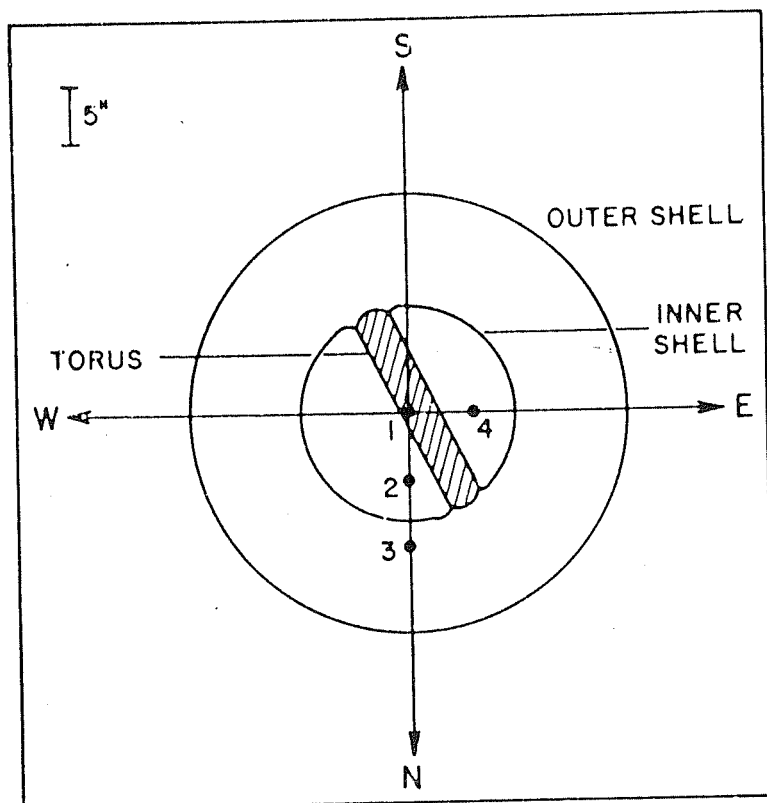
Fig. 4.16: A schematic representation of the multiple shell planetary nebula NGC 1535 on which are marked the different positions where the present observations in [OIII] 5007Å were made. The approximate position of the torus of dense matter constricting the inner shell (as found by Clayton, 1988) is also indicated.

velocity but rather a velocity distribution which is a consequence of thermal broadening and turbulence in that region. We assume that the broadening due to turbulence is gaussian in nature and is characterised by the most probable velocity V_T. Then, if the region under consideration has a bulk velocity $v(r)$, the intensity of emission as a function of the velocity v may be given by (for eg. Foukal, 1969; Lang, 1974)

$$I(v) = I(r) \, \exp \left\{ \frac{-[\,v - v(r)\,]^2}{\frac{2kT}{M} + V_T^2} \right\} \tag{4.5}$$

where k is the Boltzmann constant and M is the mass of ionic species. $I(r)$ is the intensity of the emission from the region being considered and which in the case of a forbidden line is proportional to $n_e^2 (r)$ (Osterbrock, Miller and Weedman, 1966). In addition, ions with the same velocity v, but situated in other regions along the line-of-sight, would also contribute to $I(v)$ of eqn.4.5. Thus the intensity at a particular velocity v and for a particular line-of-sight can be represented by the integral

$$I(v) = \text{const.} \int_{-\infty}^{\infty} n_e^2(r) \, \exp \left\{ \frac{-[\,v - v(r)\,]^2}{\frac{2kT}{M} + V_T^2} \right\} \, dr \tag{4.6}$$

The effect on $I(v)$ due to a finite aperture is obtained by evaluating the integral of eqn. 4.6 for all lines-of-sight included in the aperture and therefore eqn. 4.6 becomes a triple integral in r, θ, ϕ (if spherical coordinates

149

are chosen). Here θ and ϕ are the angles defining the orientation of the line-of-sight (to any point on the nebula) with the radius vector from the central star to that point. The limits of integration for r, θ, ϕ are decided by the size of the aperture subtended at the nebula and by the geometrical form chosen for the nebula. The triple integrals for I(v) were numerically evaluated using a gaussian quadrature routine (Press et al 1986). The final instrument-broadened emisssion profile is obtained by convolving I(v) with the instrument function F(v) i.e

$$I_{final}(v)= \int_{-\infty}^{\infty} F(v'-v)I(v')dv' \qquad (4.7)$$

In evaluating the integral of eqn 4.6 for NGC 1535 we have made the following assumptions (i) The dependence of the electron density with distance behaves as $n_e(r) \alpha r^{-n}$ and (ii) The nebula is isothermal i.e., T is constant (as indicated by the results of Louise and Pascoli, 1985). The geometry of the inner shell has been assumed spherical (with diameter 20") based on the almost spherical appearance of the inner shell. The shell thickness has been taken as 0.2 times the nebular radius which is in reasonably good agreement with the thickness of the shell as can be judged from the velocity images of the object (Clayton, 1988).

Initially I(v) was evaluated for the central region assuming that the bulk velocity v(r) is linearly proportional to r and by assuming a value of V_T small compared to 2kT/M [2kT/M =14.73 km^2/ s^2 for the [OIII] ion for an adopted [OIII]

temperature of $11,700^0$ K in NGC 1535 (Kaler, 1986)] However this was not able to reproduce the line profile even for different values of the index $n = 1,2,3$ in the relation $n_e(r) \propto r^{-n}$. Although the proper value for the expansion velocity could be obtained, a certain degree of disagreement was found to occur in the width of the blue and red components of the model line profile in that they were seen to be narrow compared to the observed profile. Thus the final profile, which is a superposition of the red and blue components, was found to have a low intensity level between the peaks of the red and blue components which did not match the relatively high intensity level between the peaks of the observed data. A qualitative explanation as to why the widths are found to be small may be advanced. First it may be noted that one of the broadening factors of the profile arises from the relation $v(r) = \alpha\ r$. However, this relation cannot produce much velocity dispersion across the shell if its thickness is small compared to the radius of the nebula. This is because of the following reason: from the $v(r)$ relation we see that $v_{out} = (r_{out}/r_{in})v_{in}$ where r_{in}, r_{out}, v_{in}, v_{out}, refer to the inner and outer radii and the inner and outer bulk expansion velocities respectively. Thus, if $r_{in} = 0.8\ r_{out}$ (as assumed in NGC 1535), the expansion velocites at the outer edge of the nebula would be only 1.25 times those at the inner edge. If the ions at the outer edge could emit with the same intensity as the ions at the inner edge of the shell some broadening of the profile may be expected. However, the ions in the outer region contribute negligibly to the intensity since the intensity is proportional to $n_e^2(r)$ and n_e decreases with distance. Thus the bulk of the intensity would be from regions

151

where the electron density is high i.e., from the regions close to the inner edge of the nebula. The peak intensity would therefore be centered approximately at v_{in} and the profile would have a width approximatel. equal to that caused by thermal broadening (since the dispersion in velocity does not cause much broadening as we have argued).

To circumvent the above situation, we have therefore used an increased value of the turbulence velocity V_T =7.5 km/s. For the dependence of electron density on radius we have used $n_e(r) \alpha\ r^{-3}$ which seems to fit well the observed n_e versus r behaviour in PNe (Schmidt-Voigt and Köppen, 1987b). We have dropped the assumption that $v(r)= \alpha\ r$ and held $v(r)$ constant across the nebular shell since the former assumption was found to create marginal difference to the line profile especially for the choice of $n_e\ (r) \alpha\ r^{-3}$ and for the assumed shell thickness. This constant value of the radial expansion velocity was adopted to be 21.0 km/s in line with the measured expansion velocity in the nebula (as discussed in section 4.4.2). Line profiles generated with the above assumptions and choice of parameters were found to give a good agreement with the observed data.

However, a prominent velocity structure at $\sim$ -9 km/s in the line profile obtained in position 1 (central region) with an 8" aperture could not be fitted. This structure, it may be noted, is not prominent in the 15" aperture line profile obtained in the same position. This is most likely due to its smoothening out by the use of a larger aperture. But its presence may still be inferred from the asymmetry seen in the slope of the profile between the peaks. It is possible that the above mentioned

velocity structure or component may be due to emission from the outer shell. Accordingly the line profile for the outer shell was constructed and superposed on the line profile for the inner shell. An expansion velocity of 20 km/s was adopted for the outer shell based on observations and which is found to be marginally less than the v_{exp} of the inner shell (Sabbadin, Bianchini and Hamzaoglu, 1984; Chu, 1989). The expansion velocities of both the shells being almost same, the component peaks of the outer and inner shell were found to coincide and thereby a distinct velocity component (like the structure at -9 km/s) could not be reproduced. Furthermore, and more significantly, since the surface brightness of the outer shell is only 0.15 times that of the inner shell (Chu, Jacoby and Arendt, 1987) the contribution of the outer shell to the line profile was found to be negligible for the line profiles in the centre of the nebula.

A possible explanation for the above mentioned velocity component at ~ -9 km/s could be that it represents emission from some additional material along the line-of-sight which is expanding with a different velocity than the inner shell. The above possibility finds support from the detailed spatio-kinematic study of the inner shell of NGC 1535 by Clayton (1988). Clayton's results show that there is distinct evidence for the presence of a torus of material in NGC 1535 which is constricting the inner shell. The approximate position and orientation of the toroidal belt of matter is shown in Fig 4.16. This ring or torus is found to be oriented almost edge-on and from the radial velocity data of Clayton (1988) its expansion velocity can be inferred to be in the range 13-15 km/s.

Based on the results of Clayton, we have attempted to see whether the inclusion of the kinematics of the torus into the model can reproduce the additional structure at -9 km/s that we have mentioned. We adopted an expansion velocity of 14 km/s for the toroidal ring (based on Clayton's results). The temperature of the emitting gas in the torus was assumed equal to the inner shell temperature. The same form of the functional dependence of n_e on r was assumed as in the inner shell. A smaller value of the turbulent velocity equal to 3 km/s had to be considered for the torus to get a good fit to the observed data. The geometry of the torus was assumed to be ring-shaped with a diameter equal to the inner shell diameter and oriented edge-on to the line-of-sight. The line profile i.e., I(v) was then calculated for such a ring and was superposed on the line profile of the spherical inner shell yielding the final profiles.

It must be mentioned that the kinematics of the torus has been included only in the central region line profiles obtained with both 8" and 15" apertures. This is so because in position 2 and 3 of the nebula, the isolating aperture does not cover significant parts of the torus. This can best be seen from Fig 2 of Clayton's work. The inclusion of the torus for the central region profiles could produce the observed velocity component at -9 km/s which can be interpreted as corresponding to the blue shifted component of the expanding torus. However, the red shifted component of the torus gave an identical component at +9 km/s which was at variance with the observed data. We had to suppress this unwanted component by assuming that the red component of the torus was about three times weaker than the blue.

There appears to be some support for this assumption. A careful inspection of the radial velocity images given in Fig.1 of Clayton (1988) does seem to indicate that the blue shifted component is brighter than the red. We propose that this could possibly be due to dust confined to the toroidal ring which would then cause larger obscuration for the red component than the blue one. Such a toroidal disc of dust has been detected for instance in the bipolar PN NGC 6302 (Lester and Dinerstein, 1984).

4.4.5 Results from the model:

A comparison of the final line profiles, constructed on the basis of the detailed discussions of the last section, with the observed profiles can be made from Fig.4.17. The line profile at position 4 could not be modelled since the SNR was inadequate at that position. The profile in this position is shown separately in Fig. 4.18. The parameters and characteristics of the observed and model profiles are summarized in table 4.4.

[OIII] 5007 Å LINE PROFILES IN NGC 1535
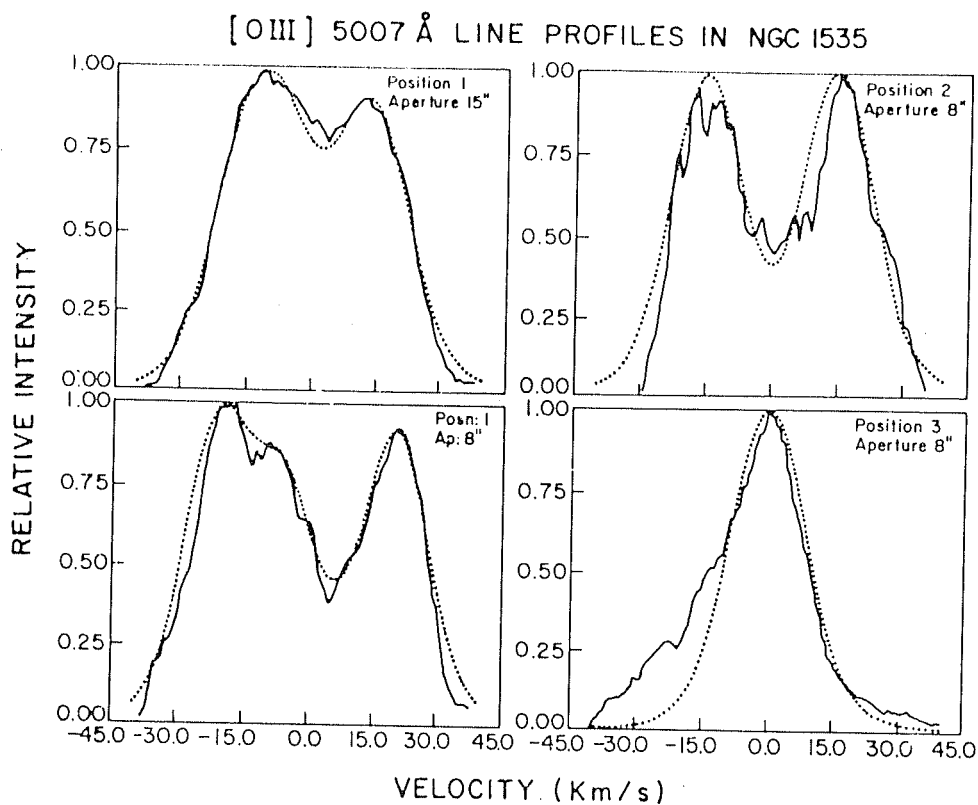
Fig. 4.17: The observed line profiles in NGC 1535 (indicated by the continuous lines) in the [OIII] 5007Å line obtained at different positions of the nebula. The computed model emission line profiles are indicated by the dotted lines.
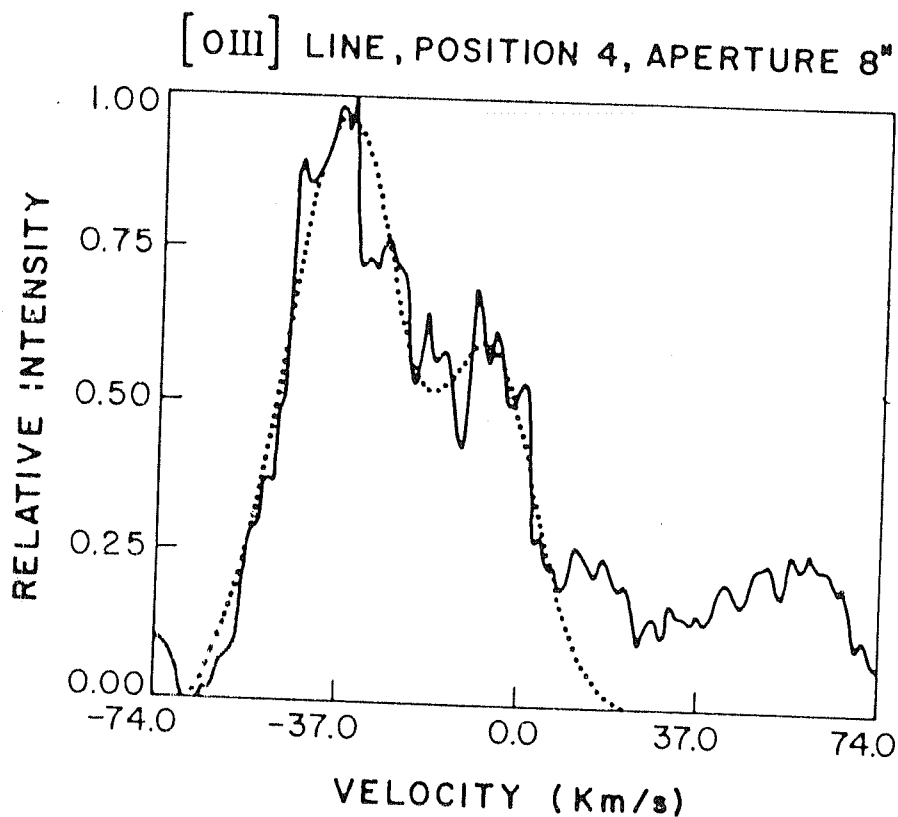
Fig. 4.18: The [OIII] 5007Å line profile in position 4 (refer Fig. 4.16) in NGC 1535. A good signal-to-noise ratio was not obtained in this position. The observed profile (indicated by the continuous line) has been fitted by a double-component Gaussian indicated by the dotted line.

Table 4.4

Characteristics of observed and model line profiles

Position on the nebula	Aperture diameter (arc sec)	SNR	Observed expansion velocity (km/s)	Model expansion velocity (km/s)
1	8	10	19.5	20.0
1	15	19	12.0	11.5
2	8	8	16.0	15.0
3	8	10	no line splitting	no line splitting
4	8	4	15.0	not modelled

From Table 4.4 it may be seen that there is a good agreement between the observed and model expansion velocities. The model successfully produces the requisite change in expansion velocity for different aperture sizes centred on the same position of the nebula. This is seen from the expansion velocity results for position 1 of the nebula which has been studied with both 8" and 15" apertures. The model also reproduces the observed decrease of v_{exp} at position 2 with respect to the centre. In position 3 no line splitting is seen in the observed data. The model fit also does not show any line splitting in this position and appears like a single gaussian. However, there are actually two components in this model fit corresponding to the blue and red shifted parts of the shell but with a small inter-peak separation i.e., a small

expansion velocity. Their superposition therefore gives the appearance of a single curve. It may be noted that a small line-of-sight expansion velocity is expected in this position because the aperture in this position isolates a region of the nebula which is expanding almost perpendicular to the line-of-sight.

A puzzling feature of the profile in position 3 is the broadening on the blueward side. This broadening may be attributed to emission from the approaching half of the outer shell for the following reasons. The isolating aperture in this covers only a part of the rim of the inner shell and a large portion of the outer shell. Hence although the outer shell is much fainter than the inner one, it can contribute significantly to the intensity in this position. Secondly, from the echelle slit images of NGC 1535 by Chu (1989), it can be seen that the slit image of the outer shell is tilted bluewards with respect to the inner one. A tilt of this kind implies that for a given line-of-sight the radial velocity of the outer shell is shifted bluewards of the radial velocity of the inner shell. Since Chu (1989) does not mention the orientation of the slit with respect to the nebula, we cannot directly assume that the slit was oriented N-S and passed through position 3. However, if such a tilt be present in position 3 the emission from the outer shell would be radially offset towards the blueside with respect to the line profile of the inner shell thereby leading to the excess of intensity in the blueward side of the observed profile. The nature of the slit images of Chu (1989) also gives some indication of the morphology of the outer shell. The observed tilt obviously precludes a spherical form and

suggests a spheroidal morphology for the outer shell.

4.4.6 Conclusions on the kinematics and morphology of NGC 1535:

The main conclusions that can be drawn from the model regarding the morphology and kinematics of NGC 1535 are as follows:

(i) The kinematics of NGC 1535 may be explained by assuming the inner shell to be of a spherical form with the added presence of a torus of material constricting the inner shell. The observed line profiles in the PN may be explained based on the assumptions of a constant expansion velocity in the [OIII] line emitting region of 21 km/s for the inner shell, a $n_e(r) \propto r^{-3}$ relation for the dependence of electron density on distance and the presence of turbulence in the main shell characterized by a most probable velocity of 7.5 km/s.

(ii) There is evidence based on the kinematic observations and on the model that the outer shell of NGC 1535 is spheroidal in form.

4.4.7 Formation mechanism of NGC 1535:

Certain conclusions may be drawn, based on the morphological structure and observed kinematics, regarding the mechanism involved in the formation and structural development of NGC 1535. We however defer this discussion at present and discuss it at a later stage in Chapter V.

4.5 NGC 5882 :

NGC 5882 is a southern PN (PK number 327 +10°1; R.A.(1950) = 15^h 13^m 25^s; Dec = -45° 27′ 56″) which appears as a spherical blob of radius 7.5″ (Perek and Kohoutek, 1967). High resolution slit spectra of this PN have been obtained by Ortolani and Sabbadin (1985). Their results give expansion velocities of 16.5 km/s and 23.5 km/s in the [NII] and Hβ lines respectively and also indicate that the emission from the blue component is less than that from the red. Measurements of [OIII] which could throw light on the motions of the inner regions of the nebula are not available for the object.

NGC 5882 was observed in the Hβ 4861Å line with an aperture of 30″ and in the [OIII] 5007Å line with three different aperture sizes of 8″, 15″ and 30″ respectively with an aim to see the effect of increasing aperture size on the expansion velocity. All observations were made with the aperture centred on the nebula. High SNR scans were obtained in this object. A representative scan of two orders in [OIII] using an aperture of 15″ is shown in Fig.4.19. The individual line profiles in the central region of NGC 5882, with the aperture size and the emission line indicated, are given in Fig 4.20. Each line profile has been fitted by two gaussians. The profiles indicate an expanding shell with V_{exp}= 12.5 km/s, the relative intensities of the receding and approaching velocity components being consistent with the findings of Ortolani and Sabbadin (1985). In Table 4.5 we give the line profile parameters in NGC 5882.
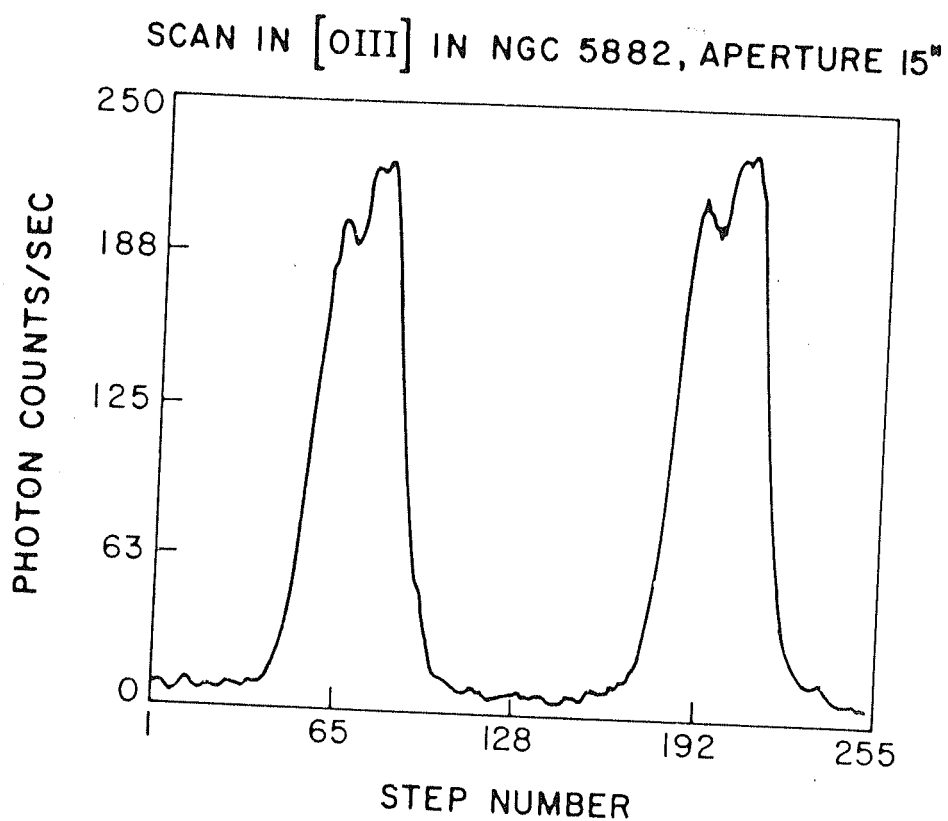
Fig. 4.19: A representative scan of two orders in the central region of NGC 5882 in the [OIII] 5007Å line using an aperture of 15″. Step number varies linearly with etalon spacing or wavelength.

EMISSION LINE PROFILES IN NGC 5882
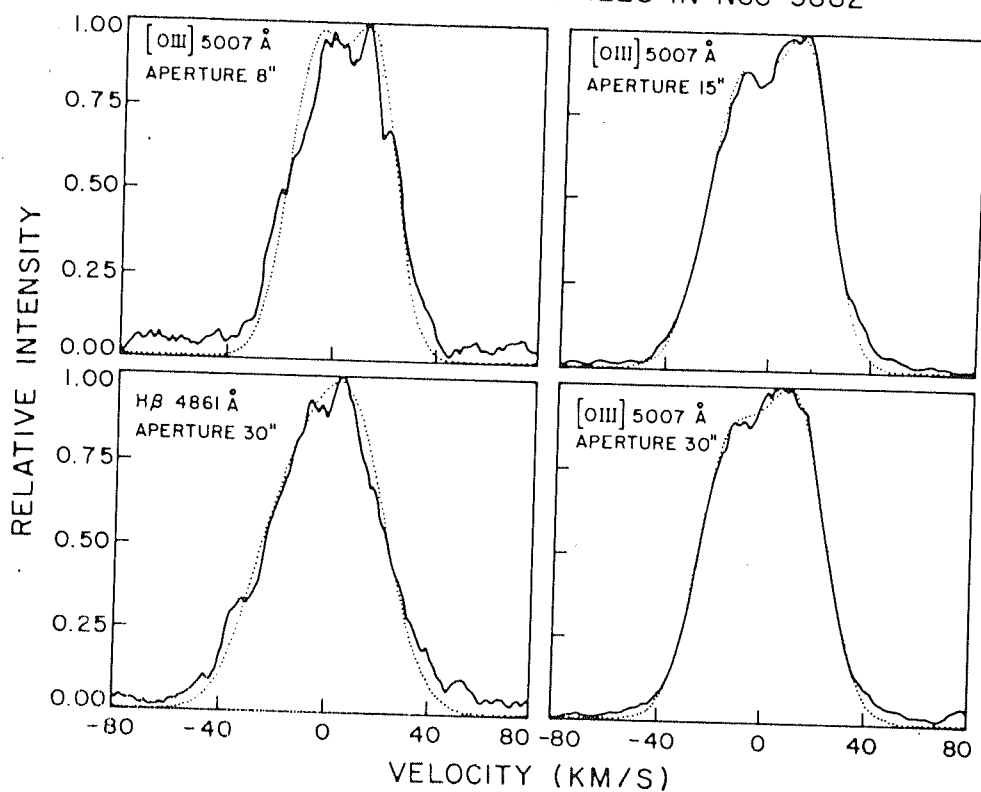
Fig.4.20: The observed line profiles (indicated by continuous lines) in NGC 5882 in the [OIII] 5007Å and Hβ 4861Å lines. The aperture that has been used is also indicated. Each observed profile has been fitted by a double-component gaussian indicated by the broken line.

Table 4.5

Emission line parameters in NGC 5882

Emission line	Aperture diameter (arc sec)	SNR[*]	Widths (W) and Relative intensities (I) of individual components				Vexp (km/s)
			W_1 (km/s)	W_2	I_1	I_2	
[OIII] 5007Å	8	5	24.0	22.5	0.88	0.86	11.0
"	15	15	26.5	25.0	0.83	0.89	12.0
"	30	15	27.0	27.5	0.72	0.90	12.0
Hβ 4861Å	30	8	31.2	35.0	0.50	0.89	13.0

[*] Signal to noise ratio at the peak of a single profile.

A few points may be noted from Table 4.5 and also from the line profiles of Fig.4.20 viz: (1) The expansion velocity in the nebula does not decrease when the aperture is increased from 8" to 15". In fact it remains constant and shows a tendency to increase marginally but close to the errors of observation which may not be realistic. One can however state definitely that there are no indications for a decrease; (2) The widths of the individual components show a marginal increase (again close to the limits of the the errors) as one goes from 8" to 15" aperture sizes; (3) Comparison of the line profiles obtained with aperture sizes of 15" and 30" shows close similarity in shape, line widths and expansion velocities. Further no change in the level of the signal was obtained between these two apertures (15" and 30").

From this it may be concluded that the bulk of the emission is from a 15$"$ region which coincides with the spatial extension of NGC 5882.

However for a spherically symmetric nebula, as in the case of NGC 5882, it is expected that the expansion velocity should decrease when the aperture size is increased. This is because if the shell is expanding radially with velocity V_{exp}, then for any line-of-sight, the observed expansion velocity would be $V_{exp}\cos\theta$ where θ is the angle between the line-of-sight and a radius vector drawn from the star to the point of intersection of the line-of-sight with the shell. For a infinitesimally small aperture passing through the centre of the shell the true V_{exp} would be observed, but for a larger aperture, smaller line-of-sight velocity components would also be included thereby giving a smaller observed expansion velocity than the actual value of V_{exp}. The expected decrease in line-splitting has been worked out in a model by Robinson, Reay and Atherton (1982) and is given by an equation similar to eqn.3.2 of Chapter III. The concerned equation is however valid only for values of the projected aperture size less than 0.5 times the nebular radius.

In general the line profile expected from the nebula for any aperture size can be obtained by generating the profiles in the same manner as was done for NGC 1535 and which is described in details in the last section. We have evaluated the emission profile by the above procedure for a spherical shell and an oblate spheroidal shell. The reason for the choice of the second geometrical form is twofold viz. (i) such a form would appear spherical (like NGC 5882) when projected in the sky with

the minor axis along the line-of-sight and (ii) if it is assumed that v is proportional to r in the nebula then increasing aperture sizes should take in elements of the shell at larger values of r (the radial distance from the central star to the shell) and therefore having higher velocities. However these higher velocity components when projected along the line-of-sight would be diminished by corresponding greater amounts since the projection angle increases for the components. Since it is difficult to conclude apriori which of these two factors could be dominant, it is worthwhile to verify whether an oblate spheroidal form would yield constant or increasing expansion velocities with increasing aperture sizes.

In constructing the line profiles we have assumed a shell thickness small compared to the dimensions of the nebula. We have also assumed the electron density behaves as $n_e \propto r^{-n}$ (as in the case of NGC 1535). Different values of the index n = 0, 1, 2, and 3 in the above relation were tried. We find from the study that for both spherical and oblate spheroidal shells, the expansion velocity decreases with increasing aperture size. This is true even when extreme values of eccentricity were chosen for the geometry of the oblate spheroidal shell. Further in the above model, the total width at half intensity of the profile is found to decrease with increasing aperture size. For the sake of comparison, we note for a spherical shell that the decrease in the line-splitting due to an aperture subtending 25 percent of the nebular diameter is about 3 percent in the Robinson, Reay and Atherton (1982) model and about 4 percent in our study. From the above work it is seen that the observed kinematic field in NGC

166
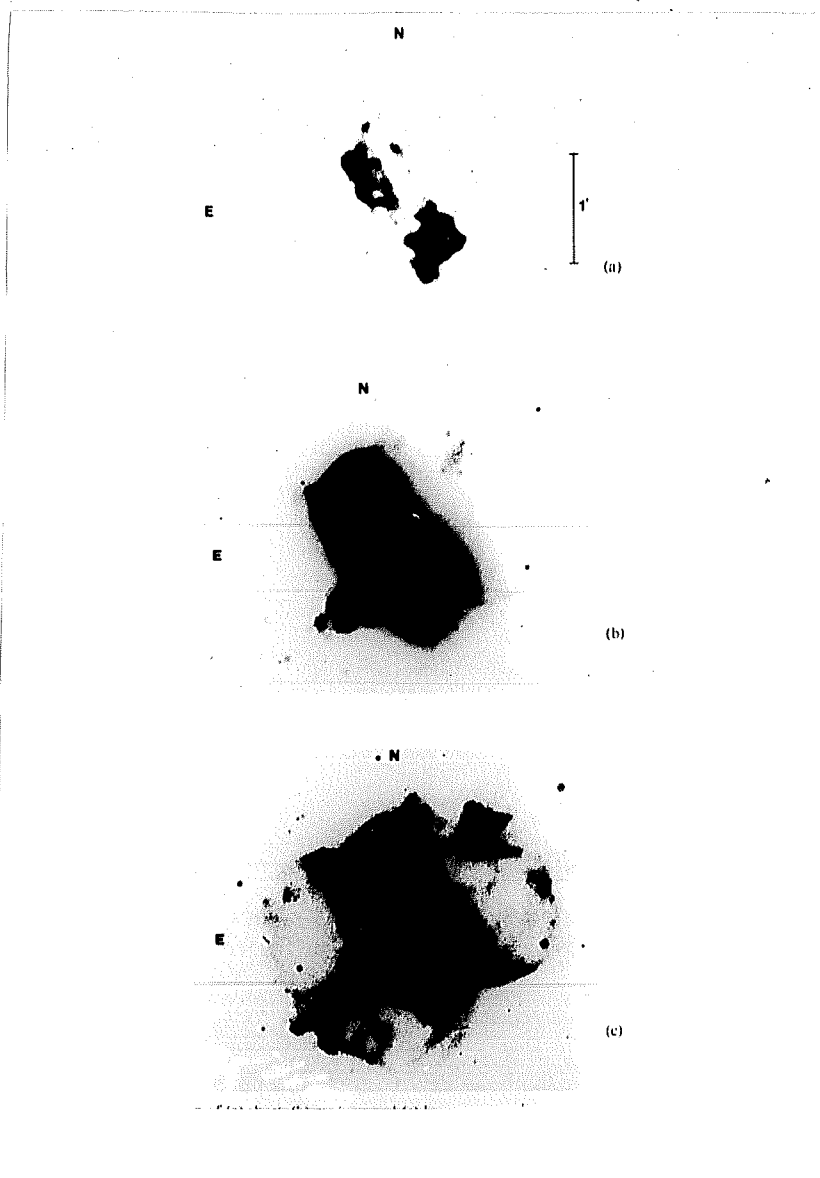
Fig.4.21: Images of NGC 650/1 (from Sabbadin and Hamzaoglu,1981) obtained in the Hα and [NII] lines with short, medium and long exposures.

the northeast (NE) and southwest (SW) ends of the bright 'rectangle'. The only existing study in [OIII] is by Sabbadin and Hamzaoglu (1982, hereafter SH82) who have obtained echelle slit spectra of the object with the slit oriented at position angles of 45^0 and 135^0 respectively. Our [OIII] observations are restricted to three positions on the object, viz. the central region and two other positions symmetrically opposite in the NE and SW directions and 20" away from the central star along the bright central bar. An aperture of 30" was used in each position. The regions we have observed are in a sense analogous to Taylor's since his observations are also in 2 positions (in the NE and SW ends of the central bar) except that the 40" aperture used by him gives slightly less spatial resolution and the positions studied by him are 25" away from the central star though in the same direction.

We present in Fig. 4.22 the line profiles obtained in NGC 650/1 in the three different positions-each of the curves has been fitted by two gaussians. We also present in Table 4.6 the line profile parameters in NGC 650/1, along with other observational details.
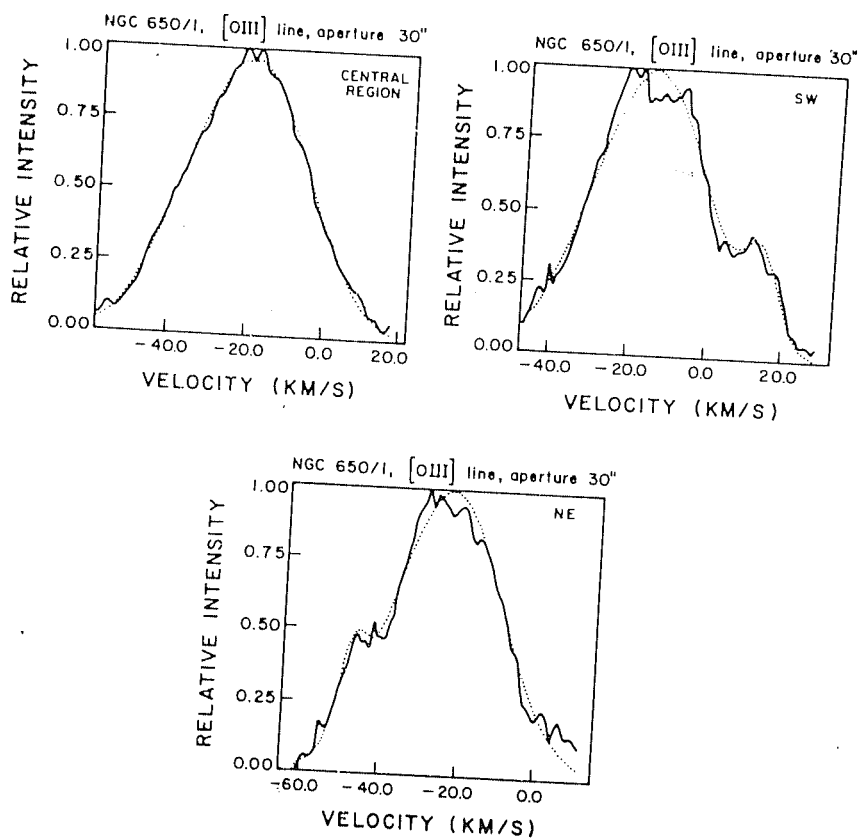
Fig.4.22: The [OIII] 5007Å line profiles at three different positions in NGC 650/1. Apart from the central region, the other two positions indicated by NE and SW are situated along position angles 45^0 and 225^0 respectively and at a distance of 20 away from the central star. The dotted lines represent a double-gaussian fit to the observed data which is shown by the continuous line. A systemic velocity of -20km/s for the central region has been adopted as per the work of RCP and SH81 (see text).

Table 4.6

[OIII] line characteristics in NGC 650/1

Position on nebula	Aperture diameter (arc sec)	SNR[*]	Widths (W) & relative intensities(I) of the profile components				Vexp (km/s)
			W_1	W_2	I_1	I_2	
centre	30	8	28.0	29.0	0.46	0.70	8.0
SW	30	10	8.0	32.0	0.25	0.96	12.0
NE	30	10	34.0	10.6	0.98	0.30	15.0

* signal to noise ratio at the peak of a single profile

Some important features that may be seen from the profiles of Fig. 4.22 are that the NE position of the central bar is slightly blue shifted by 5 ± 2 km/s and the SW postion is redshifted by 6 ± 2 km/s with respect to the velocity of the central region. Such a tilt as found in the [OIII] velocities is also found in the [NII] observations of T, RCP and SH81. This has been interpreted by SH81 to imply that the central bar is actually an elliptical ring in projection. We also note that the profiles of Fig. 4.22 in the NE and SW positions are not too well fitted near the peak of the profile by two gaussians implying that there may be more velocity components in the line-of-sight. This fact is supported by T's observations which show a triple structured profile in both the NE and SW ends of the central bar and also the rather complex velocity structure found in this object by RCP and SH81. It is also seen that the profile in the central region does

not show any line-splitting. This absence of line-splitting was seen in each of the six line profiles obtained in this position. Further the V_{exp} value (deduced from the double gaussian-fit) in the central region is found to be 8 km/s which is much smaller than the value V_{exp} = 38 km/s quoted by SH82. Even a mean V_{exp} = 12 km/s obtained by averaging expansion velocities over the three positions of our observations still falls short of SH82's value.

It is difficult to critically compare our [OIII] expansion velocities with SH82's values as extensive details regarding the latter are not available. It is also important to note that the free-spectral range of the pressure-scanning F.P.S used by us for the observations of NGC 650/1 is 76 km/s. If the expansion velocity in the central region is really ~ 38 km/s as reported by SH82, then the profiles obtained by us should be contaminated by overlapping orders. But a close inspection of the raw profiles obtained by us reveals that the base-level counts between the orders is ~ 15 counts/s which is marginally above the dark level of ~ 10 counts/s. This proves, along with the fact that the observed profiles are narrow, that overlapping of orders did not occur and that in the central region the expansion velocity may not be very different from what we report here. Further the instrument performance was checked several times during the observations and V_{exp} measurements of other objects during the same night give consistent results. However, the above dichotomy in the expansion results indicates that more extensive mapping in [OIII] is required in this nebula.

4.6.1 Spatio-kinematics and formation mechanism for NGC 650/1 :

Based solely on our observations of three regions in NGC 650/1, it is difficult to propose a spatio-kinematic model for this PN. However we discuss the different kinematic models proposed for this nebula and analyse how they fit into the proposed general mechanisms for PNe formation described in Chapter I. The physical appearance of NGC 650/1 has invoked different explanations for its morphology. Curtis (1918) has suggested that the bright rectangular bar might be a ring of matter seen edge on. Minkowski (1964) has suggested that the bar may be of a toroidal structure which is optically thick to the ionizing radiation. The indication for the optical thickness of the nebula is that the V-shaped notch on the southwest side of NGC 650/1 displays sharp edges which may be interpreted to be the rim of the ionized region. Gurzadyan (1970) has suggested the presence of a magnetic field which may be responsible for shaping the nebula.

Based on the observed kinematics, spatio-kinematic models have been proposed by T, RCP and SH81 respectively. Two possible geometrical configurations have been ascribed to NGC 650/1 by Taylor viz. a double coaxial toroid and a distorted double coaxial toroid formed on the surface of a cone. The shortcoming of the above models is that they do not explain the kinematics of the hour-glass lobes. Further it appears to us that the models do not fit into a simple framework for PN formation and shell development which can produce the rather complicated geometrical forms assumed by T. SH81 have suggested that the bright rectangle may be an elliptical ring, seen edge on, with the major axis of the ellipse oriented at $\sim 65^0$ to the line-of-sight.

Such a geometry explains well the observed tilt to the velocities seen along the bright central bar in both [OIII] and [NII]. However as pointed out by RCP (1984), the above assumed geometry, would not be able to explain the significant triple component profiles obtained by Taylor (1979) at both the ends of the 'rectangle'. This is because for the aperture used by Taylor and for the assumed geometry of SH81 the line profiles at the ends of the 'rectangle' should possibly be either single and wide or double rather than triple-structured. SH81 have also suggested that the shaping of NGC 650/1 may be the result of the mechanism suggested by Phillips and Reay (1977) described in Chapter I. However as pointed out earlier the above mechanism (Phillips and Reay, 1977) does not produce three-dimensional hour-glass structures like the shape of NGC 650/1.

Finally RCP (1984) have invoked the presence of a magnetic field in NGC 650/1 to account for the observed kinematics. In the model proposed by them, matter from the star is ejected in diametrically opposite directions from active spots along magnetic fields associated with them. The symmetrical location of the active spots produces a dipole field. The ejected matter then follows the frozen-in magnetic lines of force giving rise to the observed morphology of NGC 650/1. It may be relevant to ask however, whether it is possible to explain the morphology and kinematics of NGC 650/1 through a general mechanism for PNe formation.

In this context, the two-wind mechanism for PNe formation can be considered. PNe of hour-glass form can be produced by the above mechanism as per the models suggested by

Kahn and West (1985) and Icke (1988). It however appears to us that there may be a lacuna in considering NGC 650/1 to have been shaped solely by the mechanisms proposed by Kahn and West (1985)and Icke (1988). The reason for this is that the hour-glass shaped PNe formed by the above mechanism should have a waist of circular cross section. However the tilt in velocities observed over the bar (which represents the waist of the hour-glass structure) indicates that its kinematics is not compatible with that of an expanding circular ring of matter but rather suggests an elliptical shape as proposed by SH81. In conclusion it may therefore be said that the kinematics of NGC 650/1 does not appear to exactly agree with the models for the formation of bipolar PNe based on the two-wind interaction mechanism.

CHAPTER V

A PHYSICAL MECHANISM FOR THE STRUCTURAL DEVELOPMENT OF PLANETARY NEBULAE ENVELOPES

5.1 Introduction :

The occurance of various morphological forms of PNe viz. spherical, ellipsoidal, hour-glass, multiple shell etc. raises the important question . as to what are the physical processes which can lead to such diverse shapes. It will be pertinent to see if all the commonly observed structural forms can be accounted for by a single general mechanism for PNe formation. The aim of this chapter therefore, is to address this important aspect. We first discuss here some of the viable physical mechanisms that have been put forward by different authors to explain the formation and shaping of PNe. We then propose a possible model, which may be able to produce some of the commonly observed morphological forms of PNe. As can be seen from the preceding chapters and as will be discussed in the following sections there appears to be a scope to develop such a model since certain aspects relating either to the morphology or to the observed kinematic field in PNe do not perhaps fit straight into the framework of existing mechanisms for PNe formation and shaping. It may be mentioned that some of the contents of the initial parts of this chapter have already been discussed in Chapter I though in lesser details and the repetition has primarily been made for the sake of continuity .

5.2 Mechanisms for the ejection and morphological evolution of PNe envelopes:

We briefly consider here, some of the important mechanisms that have been proposed for the formation of planetary nebulae and also describe the corresponding morphologies that can be obtained from such mechanisms.

5.2.1 The effect of double shell flashes on PNe formation:

Tuchman, Sack and Barkat (1979, hereafter TSB) have proposed a mechanism (described in Chapter I) in which it has been shown that the development of pulsational instabilities in the envelope of the evolving AGB star can lead to ejection of the nebular shell over a period of ~ 1000 years.

In the mechanism of TSB, the onset of the mass loss i.e., shell ejection begins when the luminosity of the star becomes larger than a certain mass dependent value $l_p(m)$. However the appearance of nuclear double shell flashes (DSF's) or thermal pulses which are believed to occur at just the same luminosity range can have an important bearing on PNe formation as shown by Tuchman and Barkat (1980, hereafter TB). We describe the work of TB in a little more detail. If the preflash or quiet luminosity of the star before the onset of DSF is less than $l_p(m)$ then the star would not have entered a shell ejection phase due to the onset of pulsational instability as described in the mechanism of TSB. However the appearance of a DSF which can push the luminosity beyond $l_p(m)$ may initiate mass loss. If the DSF raises the peak luminosity of the star to exceed $l_p(m)$ then TB assume that mass

loss could occur in a similar manner as described in the TSB mechanism i.e., the envelope would be ejected in a semi regular manner every λ years ($\lambda \leq 30$) with $\sim 3\%$ of the envelope mass being removed in each ejection. However a necessary condition for ejection to commence is that not only should the peak luminosity of the star (after the shell flash) be raised above $l_p(m)$ but it should also exceed $l_p(m)$ for more than λ years. Once mass loss begins it can continue as long as the luminosity of the star is above $l_p(m)$ (which by itself decreases every time an ejection takes place since it is mass dependent). Without describing the detailed mathematics given by TB, it may be stated that their end results indicate that it is possible that only a fraction of the envelope is ejected due to a DSF (which is capable of producing mass loss) and that the remaining portion of the envelope can be ejected due to subsequent DSF's. This would then lead to a multiple shell PN, in which the shells are separated by the interflash time t_F between the DSF's. It may be pointed out that it is also possible that the entire envelope may be lost during the first DSF (which is capable of producing mass loss) thereby leading to a single shell PN.

In their model, TB show that the number of shells depends on the stellar mass. The essence, then, of the above mechanism is that the appearance of DSF (prior to the quiet luminosity of the star reaching $l_p(m)$ at which stage the onset of pulsational instabilities removes the entire envelope) can lead to the formation of multiple (or single) shell PNe.

5.2.2 Effect of stellar rotation on the evolution of PNe shells:

Considering a rapid single shell ejection, models have been proposed for the structural development of PNe shells. Louise (1973) has shown that ejection of matter from a spherical rotating star would lead to oblate spheroidal forms of the PN shell. In a detailed paper, Phillips and Reay (1977, hereafter PR) have shown that ejection from a star, with a figure of oblation determined by its rotational velocity, can lead to a variety of nebular forms under the influence of stellar rotation, gravitational braking and radiation pressure.

PR have considered that the star which ejects the shell is rotating with an angular velocity ω. The effect of such a rotation is to distort the shape of the star such that its figure of rotation is given by

$$R_*(\theta) = R_*(0) \left[1 - \omega^2 R^3_*(0) \sin^2\theta / 2GM \right] \qquad (5.1)$$

here $R_*(\theta)$ is the radius of the star at any latitude θ, $R_*(0)$ is the radius at the equator, M is the mass of the star and G is the universal gravitational constant. Eqn. 5.1 is valid for bodies with low oblation i.e., where $\omega^2 R_*^2 / V^2_{esc} \ll 1$, which is the case for red giants (V_{esc} is the escape velocity from the star). PR have then considered the motion of the ejected shell of matter from such a rotating star under the effects of gravitational braking and Lyman continuum radiation. Several morphological forms of PNe are produced by this method including spherical, ellipsoidal and toroidal shapes of PNe. However, it appears that the mechanism of PR does not produce three

dimensional hour-glass structures -a point that has also been made by Clayton (1988). Some of the shapes produced do appear like hour-glass structures but only when viewed cross sectionally. The true three dimensional forms are more similar to toroidal structures. This was one of the principal points which has prompted us to look for a method for producing hour-glass PNe in addition to the other forms obtained by PR in so far as the multiple shell ejection process is concerned.

5.2.3   Shaping of PNe envelopes by the interacting winds mechanism:

The essential mechanism in this model of PNe formation is that a fast tenuous wind (V ~ 1000 to 2000 km/s) from the hot PN nucleus interacts with the dense, slow wind (V ~ 10 km/s) from the progenitor AGB star (Kwok, Purton and Fitzgerald, 1978; Kwok, 1982; Volk and Kwok, 1985). The factor that determines the particular type of morphology that results from the two-wind interaction is the "density contrast", i.e., the ratio of the equatorial to polar density of the AGB wind. If the density contrast is moderate then elliptical morphologies result, if it is high then hour-glass PNe are formed (Balick, Icke and Preston, 1989; Balick, 1987). If there is no density contrast then a spherical shape results. Therefore, "the essential ingredient in the production of the different morphologies is the existence of an initial density contrast between the equatorial and polar direction of the AGB wind" (Bond and Livio, 1990).

We now examine some of the factors that can cause such a density contrast. Emphasizing that the cause of the

anisotropy is still a conjecture, Balick (1987) has suggested that one possible factor is due to stellar stellar rotation as outlined in the work of Friend and Abbott(1986) and Poe and Friend (1986). These authors have investigated the fast rotating O and Be stars with velocities in the range 100-600 km/s and showed that it is possible to produce a wind of velocity 2000-4000 km/s which is denser at the equator than at the poles. However, it is to be seen whether a density contrast can still be produced by scaling down the results of these authors to the case of AGB stars which are supposed to be slow rotators with wind velocities of ~ 10 km/s.

A second reason for the density contrast can be due to the binary nature of the PN nuclei. Soker and Livio (1988) and Bond and Livio (1990) have considered the ejection of the shell from a PN with a close binary nucleus. Their results indicate that ejection of matter from the common envelope of the binary system results in an enhanced equatorial density excess compared to the poles. In the case of such PNe, subsequent shaping by a fast wind should lead to ellipsoidal and hour-glass morphologies. Bond and Livio (1990) have studied thirteen PNe which are known or suspected to have close binary nuclei. They find that approximately half of these PNe show either ellipsoidal (A41, A65 LoTr 1) or hour-glass (HtTr 4, NGC 2346) morphologies which is what they expect for a moderate to high density contrast produced by binary ejection, followed by shaping by a fast wind. However, several of the PNe in their sample show peculiar morphologies (A46, HFG 1 and A35) while another PN Sp1 is spherical. In the case of Sp1, Bond and Livio (1990) suggest that it may actually be a toroidal structure seen pole-on. In conclusion it may be said

that although ejection from a binary nucleus can provide the density contrast required in the interacting-winds model, it is not well known whether all hour-glass or ellipsoidal PNe have binary nuclei and that their morphologies are consequently an outcome of the mechanism described above.

5.3 Mechanisms vs Observations - a case for a new model:

The interacting-winds mechanism, by far the most popular one, explains successfully the morphology and kinematics of ellipsoidal and hour-glass PNe. However, an aspect which does not fit easily into the prediction of the interacting-winds mechanism is the observed kinematic field of multiple shell PNe (MSPNe)(Chu, Jacoby and Arendt, 1987- hereafter CJA; Chu, 1989).

Based just on the morphologies, CJA point out that the gap between the shells in a type 1 MSPN, with detached inner and outer shells, is in discordance with the two-wind origin. Further information is obtained from the kinematic study of 28 MSPNe through long slit observations by Chu and Jacoby (1987) and Chu (1989)which indicates that the kinematic behaviour of MSPNe can be broadly categorized into the following classes. TypeI MSPNe are characterized by the inner shell expanding supersonically (20-30 km/s) into the faint outer shell which expands subsonically or mildly supersonically (< 10 km/s). Type II MSPNe are characterized by both inner shell and outer shells expanding supersonically (20-33 km/s) and with almost similar velocities i.e., the two shells seem to be co-expanding or coasting along. Apart from this, there are some type II and peculiar MSPNe in which the outer and inner shells expand supersonically and

independent of each other. Finally there are a few PNe in which the outer shell expands faster than the inner one. It is the observed kinematics of this last group of MSPNe and also the kinematics of the type II MSPNe which are not easily reconcilable with the interacting-winds mechanism for PNe formation which predict a significantly higher velocity for the inner shell vis-a-vis the outer shell (Kwok, Purton and Fitzgerald, 1978). However as mentioned in Chapter III (while discussing IC 4593) such kinematic behaviour may be explained by the effect of radiation pressure on dust present in the outer shell or the thermal diffusion of matter into the vacuum-like interstellar medium which can preferentially accelerate the outer shell.

On the other hand, it may be seen that the rapid multiple shell mechanism (TB) explains, in principle, the formation of spherically symmetric MSPNe. However, this mechanism as such fails to produce ellipsoidal and hour-glass structures. The mechanism proposed by PR which considers stellar rotation and rapid single shell ejection can give ellipsoidal and toroidal forms but not hour-glass shapes or MSPNe.

In view of this discussion we propose a mechanism based on the rapid multiple shell ejection to explain the formation and structural development of bipolar PNe and MSPNe. In order to achieve this goal, we first consider the rapid ejection of a single shell in the presence of stellar rotation and show the formation of various structural forms(as in PR). However, we further consider a second rapid ejection in order to produce the most commonly observed structural forms viz. the bipolar PNe and multiple shell PNe.

5.4 A model for the structural development of PNe envelopes:

We assume in our model that the ejection of the envelopes of PNe occurs along the lines of the mechanism proposed by TB wherein both single shell or multiple shell PNe can be formed. To study in general, the motion of an ejected shell, we have proceeded along similar lines as the PR mechanism in as much as we also consider the effects of stellar rotation on and gravitational retardation of a single shell.

We show in Fig. 5.1 a schematic diagram of the geometry of the rotating star. If one assumes the progenitor AGB star to be represented by a homogeneous gaseous mass in uniform rotation then the star would assume a spheroidal configuration i.e., the spheroid of Maclaurin. This assumption of homogeniety i.e., uniform density within the star is not a realistic one but has been made since the density stratifications within are not too well known. For a Maclaurin spheroid, the equation of its surface in a Cartesian coordinate system is given by

$$\frac{x^2+y^2}{a^2} + \frac{z^2}{c^2} = 1 \qquad\qquad ..(5.2)$$

where a and c are the semi major and minor axes respectively. For a given eccentricity e the angular velocity ω of the spheroid is given by(Chandrasekhar, 1969)

$$\omega^2 = 2\pi\rho G\, e^{-3} (1 - e^2)^{1/2} [(3 - 2e^2)\sin^{-1} e - 3e(1 - e^2)^{1/2}\,] \qquad\qquad ....(5.3)$$

184
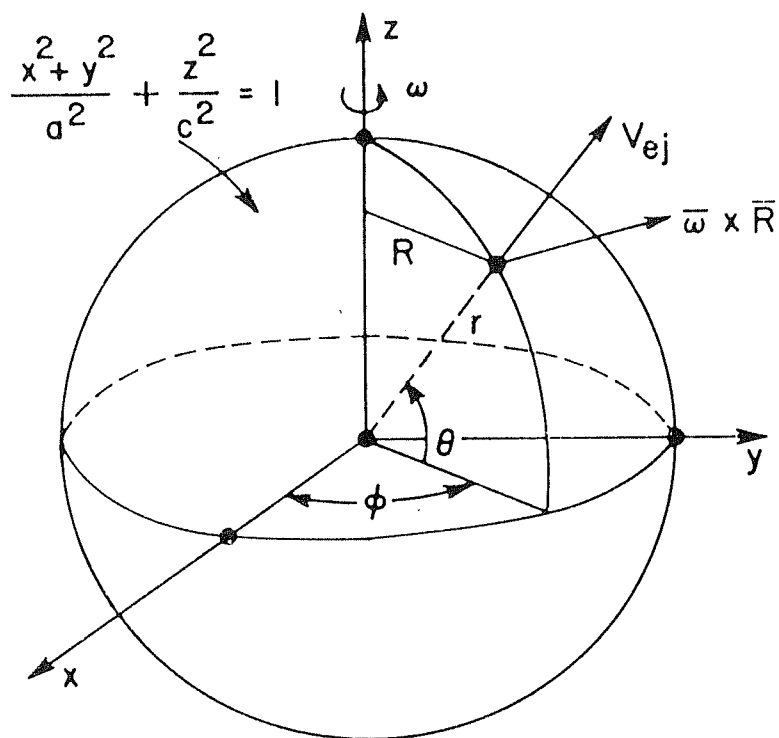
Fig.5.1: Schematic diagram showing the geometry of the rotating star and the system of coordinates used in the model.

The gravitational potential of such a spheroid is given by (Chandrasekhar 1969),

$$L(x,y,z) = \pi G \rho a^2 c \, [\, A_1 - A_2 (x^2 + y^2) - A_3 z^2 \,] \qquad ....(5.4)$$

where

$$A_1 = \int_0^\infty \frac{du}{(a^2 + u)(c^2 + u)^{1/2}} = \frac{2\sin^{-1}e}{a\,e}$$

$$A_2 = \int_0^\infty \frac{du}{(a^2 + u)^2(c^2 + u)^{1/2}} = \frac{\sin^{-1}e - e(1-e^2)^{1/2}}{(a\,e)^3}$$

$$A_3 = \int_0^\infty \frac{du}{(a^2 + u)(c^2 + u)^{3/2}} = \frac{2[e(1 - e^2)^{-1/2} - \sin^{-1}e]}{(a\,e)^3}$$

where $e = (a^2 - c^2)^{1/2}/ a$ and ρ is the density.

In polar coordinates (Fig.5.1) the radius vector to any point on the surface at a latitude θ is given by

$$r_*^2(\theta) = \frac{c^2}{1 - e^2\cos^2\theta} \qquad ...(5.5)$$

substituting

$$\text{mass } M = \frac{4\pi\rho a^2 c}{3} \;;\quad x^2 + y^2 = \frac{a^2 (1-e^2)\cos^2\theta}{1-e^2\cos^2\theta} \;;\quad z^2 = \frac{a^2 (1-e^2)\sin^2\theta}{1-e^2\cos^2\theta}$$

186

we get

$$L(\theta) = \frac{3\,G\,M}{4\,c}\left[A_1 a - \frac{A_2(1-e^2)a^3\cos^2\theta}{1-e^2\cos^2\theta} - \frac{A_3 a^3(1-e^2)\sin^2\theta}{1-e^2\cos^2\theta}\right]$$

$$..(5.6)$$

It can be seen that the potential is independent of the azimuthal angle ϕ since a Maclaurin spheroid is a surface of revolution. Further, since the quantity in brackets in eqn. (5.6) depends on the variables e and θ, we can write simply

$$L(\theta) = \frac{3\,G\,M\,f(e,\theta)}{4\,c} \qquad \qquad ....(5.7)$$

We assume that matter from the surface of the star is ejected radially with a constant ejection velocity V_{ej}. Hence the velocity of a mass element ejected from any latitude θ is given by

$$V^2(\theta) = V^2_{ej} + \omega^2 r_*^2(\theta)\cos^2\theta \qquad ....(5.8)$$

If the mass element has enough kinetic energy to overcome the gravitational field of the ejecting star it would escape. For a spherical star, the mass element would trace a hyperbolic orbit in the plane containing the radius and rotation velocity vectors. Therefore the terminal angle of a mass element ejected from latitude θ would remain the same at infinity. However, rotation of the star causes a slight deviation from sphericity and makes it oblate. The motion of a body around such a near-spherical object (for e.g. the earth) has been worked out

(for e.g. Geyling and Westerman, 1971). For bound orbits, it is shown that to the first order, the size, eccentricity and inclination of the orbit do not change between cycles of revolution. In this vein we will consider in our model only small values of rotation which cause slight deviations from sphericity. It may then be justified in assuming (following PR) that the motion of the ejected matter would still approximate hyperbolic orbits just as in the case of a spherical mass distribution.

At infinity, the mass element which is gravitationally free, would have an excess kinetic energy (determined by its terminal velocity V_T) which is given by

$$V_T^2(\theta) = V_{ej}^2 + r_*^2(\theta)\omega^2 \cos^2\theta - 2 L(\theta) \qquad ...(5.9)$$

If we define V_P(a quantity which approximates the escape velocity at the poles) as

$$V_P^2 = 2 G M / c$$

then we obtain for the terminal velocity

$$V_T^2 = V_{ej}^2 + \frac{a^2\omega^2\cos^2\theta(1- e^2)}{1 - e^2\cos^2(\theta)} - \frac{3f(e,\theta)V_p^2}{4} \qquad ...(5.10)$$

where $a\omega$ is the equatorial rotational velocity.

The above equation defines a terminal velocity surface. If there are no further accelerative mechanisms acting on the envelope, then it can also help define the terminal shape of

the PN. Here the terminal velocity can be assumed to be reached at a distance much smaller than the typical size of a PN (~ 0.1 pc or ~ $4 \times 10^6 R_\odot$). It is useful to see the behaviour of the terminal velocity as a function of θ for given values of V_{ej} and $a\omega$. In Table 5.1 we show (refer columns 1 to 4) the contribution of the three terms in eqn. 5.10 and the resultant terminal velocity. The other columns also indicate the dependence of terminal velocity on V_{ej} and $a\omega$ but have special reference to the ejection of a partial toroidal shell which is dealt with shortly. In Table 5.1, $\Omega(\theta)$ corresponds to the second term and $2L(\theta)$ corresponds to the third term of eqn. 5.10.

From Table 5.1 we see that the gravitational energy at the pole is more than that at the equator. This, coupled to the fact that the rotational energy behaves in the opposite sense, leads to a decrease in the terminal velocity when moving polewards. For any given ejection velocity which is close to the escape velocity at any point, the terminal velocity obtained from eqn. 5.10 is comparable to the generally observed expansion velocities in PNe. In Figs. 5.2, 5.3 and 5.4 we present the effect of increasing stellar rotation and ejection velocities on terminal shapes of PNe. It can be seen that as the ejection velocities are increased, the axial ratio, defined as the ratio between the polar and equatorial extensions of the terminal shape, increases and approaches unity making it spherical. All the contours in Figs. 5.2, 5.3 and 5.4 it must be noted, are cross-sectional views and the true PN surface could be generated by rotating the contours about the spin axis which (in Figs 5.2, 5.3 and 5.4) lies on the plane of the paper and runs from top to bottom or vice versa. If

Table 5.1

Dependence of Terminal Velocity on rotation and ejection velocity

θ (°)	$V_{ej}=38.0$ $a\omega=6.33$			$V_{ej}=34.75$ $a\omega=3.95$			$V_{ej}=34.75$ $a\omega=3.14$		
	$\Omega(\theta)$	$2L(\theta)$	$V_T(\theta)$	$\Omega(\theta)$	$2L(\theta)$	$V_T(\theta)$	$\Omega(\theta)$	$2L(\theta)$	$V_T(\theta)$
0	40.09	1141.7	18.50	15.45	1193.6	5.42	9.86	1205.1	3.51
10	38.66	1143.1	18.43	14.95	1194.1	5.32	9.55	1205.4	3.42
20	34.63	1147.1	18.21	13.54	1195.5	5.05	8.66	1206.3	3.15
30	28.70	1153.0	17.88	11.40	1197.7	4.61	7.32	1207.6	2.69
40	21.81	1159.9	17.49	8.82	1200.2	4.00	5.69	1209.2	1.99
50	14.90	1166.8	17.09	6.14	1202.9	3.28	3.98	1210.9	0.74
60	8.77	1173.0	16.73	3.68	1205.4	2.41	2.39	1212.5	–
70	4.01	1177.7	16.44	1.71	1207.4	1.36	1.11	1213.8	–
80	1.02	1180.7	16.25	0.44	1208.7	–	0.29	1214.6	–
90	0.00	1181.7	16.19	0.00	1209.1	–	0.00	1214.9	–

A value of $V_p^2 = \dfrac{2GM}{C} = 35.0$ km/sec has been taken.

$L(\theta)$ and $\Omega(\theta)$ are in km^2/sec^2; V_{ej}, $a\omega$ and V_T are in km/sec.
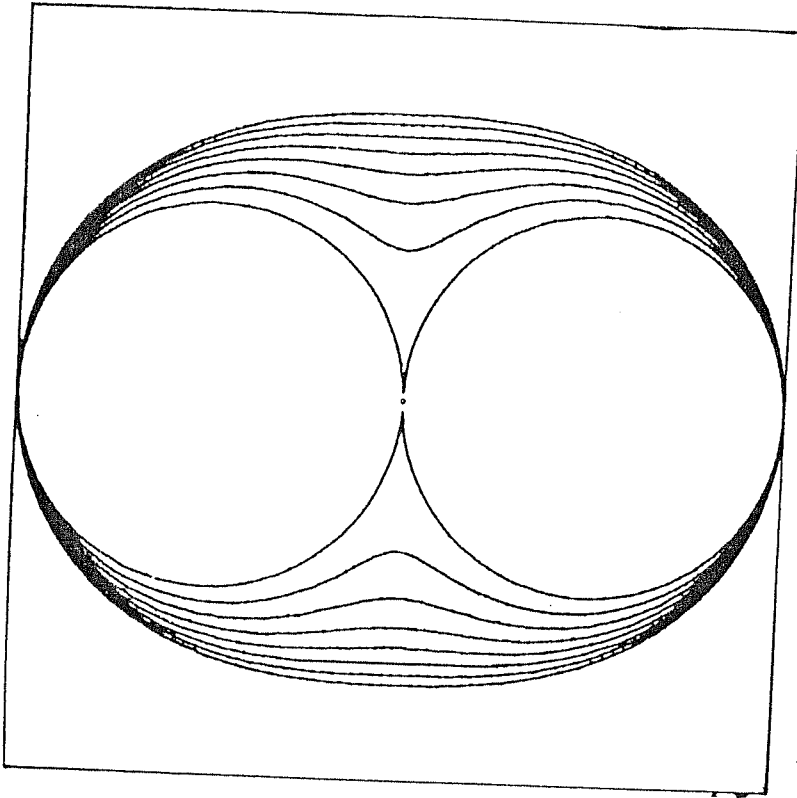
Fig.5.2: The effect of increasing V_{ej} on the terminal shapes of the nebular shell formed under the effects of stellar rotation and gravitational braking are shown. The different terminal shapes have been obtained by considering the same values of $a\omega = 3.15$ km/s and $V_p = 35.0$ km/s for each configuration but by varying V_{ej} from 34.9 to 35.3 km/s in going from the innermost contour to the outermost one.
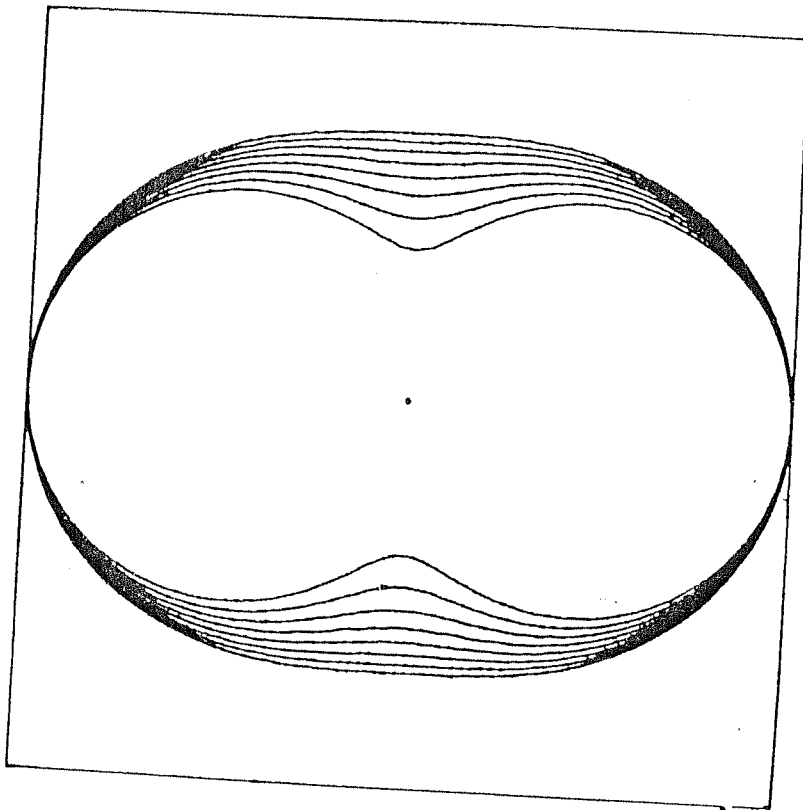
Fig.5.3: Terminal shapes of the nebular shell, similar to those shown in Fig.5.2, but for an increased value of $a\omega = 3.95$ km/s. The values of V_p and V_{ej} used here are the same as those considered for the configurations in Fig.5.2.
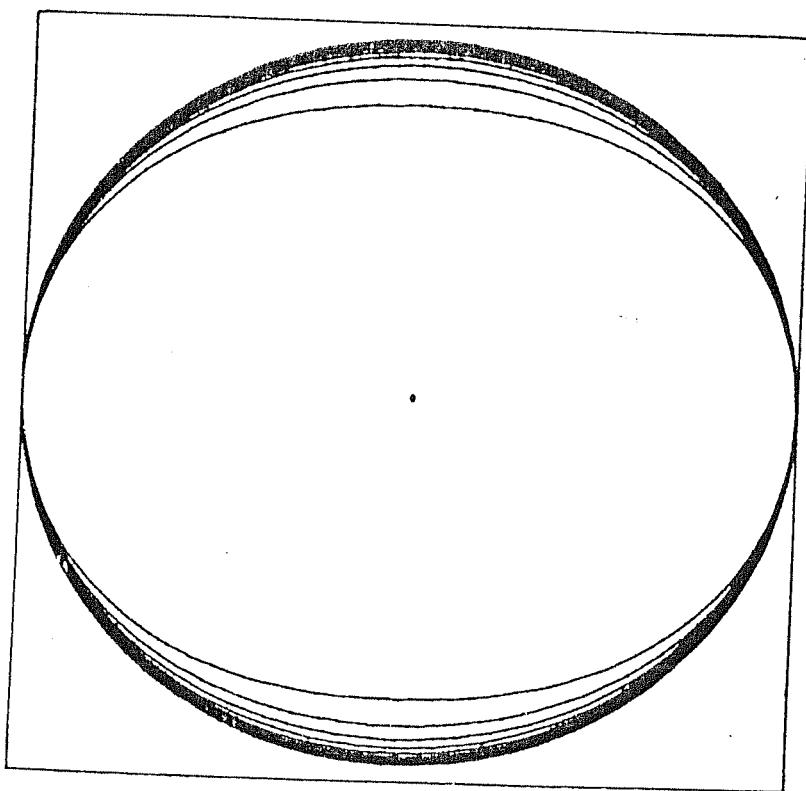
Fig.5.4: This figure shows the effect of a further increase in V_{ej} on the terminal shapes of Fig.5.2. Here also values of $a\omega$ = 3.15 km/s and V_p = 35km/s have been considered for each terminal shape but V_{ej} varies from 35.3 to 38.0 km/s in going from the innermost contour to the outermost one. As may be seen the effect of increasing V_{ej} tends to make the shells more spherical.

the three dimensional figures obtained after such a rotation about the spin axis are envisaged, it may be seen that the commonly observed spherical and spheroidal shapes of PNe can be obtained but not the figure-of-eight or hour-glass structures. In the PR model also, under the effect of gravitational retardation, similar terminal shapes are obtained as in Figs.5.2, 5.3 and 5.4. It may therefore be inferred that hour-glass shapes do not result in the PR model.

The terminal velocities and shapes obtained so far in our model under the effect of gravitational braking are very similar to those obtained in the PR model. The marginal difference in the calculated terminal velocities (for a given $a\omega$ and V_{ej}) between the two models arises primarily because of the different figures of rotation that have been considered.

We now consider an interesting aspect common to both the PR and our model viz. the ejection of a partial toroidal shell from the star. From earlier discussions and also from Table 5.1, it may be seen that the probability of the ejected matter escaping from the star is maximum at the equator and decreases in the poleward direction. This is because not only is the available rotational kinetic energy maximum at the equator but also because the gravitational field is weakest at the equator. For a given value of ω and an appropriate V_{ej}, we see that the right hand side of eqn. 5.10 can be positive from the equator ($\theta = 0^0$) to a critical latitude θ_c and negative from θ_c to the pole ($\theta = 90^0$). The negative values indicate that in the domain $\theta_c < \theta < 90^0$, the ejected matter does not possess enough energy to overcome the gravitational field of the star and escape. The angle θ_c (for a

particular choice of V_{ej} and $a\omega$) can be obtained from eqn. 5.10 by setting the right hand side of the equation to zero. Hence the critical latitude is defined through the equation

$$\frac{a^2\omega^2(1-e^2)\cos^2\theta_c}{1-e^2\cos^2\theta_c} = \frac{3f(e,\theta_c)V_p^2}{4} - V_{ej}^2$$

$$..(5.11)$$

For $\theta > \theta_c$ there is no ejection and hence the shell matter would be confined to a region between the equator and latitude θ_c, thereby forming an equatorial torus.

The above point is clearly illustrated in Table 5.1. With reference to the above table, if one considers for e.g. the case where $V_{ej} = 34.75$ km/s and $a\omega = 3.14$ km/s it can be seen that upto $\theta = 50^0$ the value of $V_{ej}^2 - \Omega(\theta) - 2L(\theta)$ is positive whereas at $\theta = 60^0$ it is negative and hence has not been indicated in Table 5.1. This means that θ_c lies in between 50^0 to 60^0. In fact the exact value of $\theta_c = 51.6^0$. A second illustration for the partial ejection of a shell is seen in the above table for $V_{ej} = 34.75$ km/s and $a\omega = 3.95$ km/s in which case $\theta_c = 76.6^0$.

5.4.1. Formation of hour-glass PNe :

We have seen in the preceding section that hour-glass PNe are not produced in our model or in the PR mechanism by considering the ejection of only a single shell. We therefore consider whether the ejection of two shells can lead to the formation of these PNe. To effect this, we propose that the initial step leading to the formation of an hour-glass PN is the

ejection of a first shell in the form of a partial toroidal shell as discussed earlier. Subsequent to the ejection of this toroidal belt if a second shell be now ejected with a suitably higher velocity than the first, it would collide with the first after a certain time. It can then be envisaged that the ensuing final structural form would comprise of a slowly expanding toroidal belt trying to constrict a faster expanding nebular shell. Therefore a figure-of-eight or hour-glass structure would result. This is in essence the mechanism that we propose for the formation of hour-glass PNe.

Before constructing a simple model along the above lines we first decide on the choice of the numerical values of the different parameters that are being used such that they may be realistic. The escape velocity V_p for AGB stars can be estimated to be in the range 20-40 km/s (PR, 1977; Tuchman and Barkat, 1979; Zuckerman and Gatley, 1988). Since direct measurements of the surface rotation rates of AGB stars are not available it is difficult to estimate the value of $a\omega$. For red giants the mean observed equatorial rotation velocity has been found to be < 12 km/s (Allen, 1973). For AGB stars, Zuckerman and Gatley (1988) have argued by assuming the conservation of angular momentum, that the surface rotational velocity should be ~ 1 km/s. They state that if the progenitor of the AGB star is a massive main sequence star which can have high rotational velocities of ~ 200 km/s (Calvert and Peimbert, 1983) then on expanding to the AGB phase (wherein its radius has been assumed to be $1000R_\odot$) its surface velocity would be of the order of ~ 1 km/s. We feel that this figure of 1 km/s should be taken as indicative that AGB stars have

low surface rotational velocities. If slightly higher rotational velocities (~ 300-350 km/s) are assumed for the main sequence star (refer the maximum rotational velocities measured in certain A and B type stars given in Allen, 1973) and a smaller final AGB radius of a few times $100 R_\odot$ is considered (TB, 1979; Iben 1985) then the conservation of angular momentum yields a value of $a\omega \sim 3$ to 4 km/s. It may therefore be realistic to assume small rotational velocities of this order as has been done in our model.

To calculate the final velocity configurations attained after the collision of the two shells (one toroidal and the complete shell) we proceed as follows. Let the terminal velocities of the two shells (determined from eqn. 5.10) be V_{T1} and V_{T2}. The inter-flash time t_f i.e., the time between two ejections, may be obtained from the relation given by Paczynski (1975),

$$\text{Log } t_f = 4.5 \, (1.68 - m_c)$$

For the core mass m_c varying between 0.75-0.90 $M_\odot$, t_f varies between 1.5×10^4 to 3000 years. The time elapsed between the collision of the two shells is

$$t_0 \sim \frac{V_{T2} t_f}{V_{T2} - V_{T1}} \tag{5.12}$$

It may be seen from Table 5.1, that for the small assumed values of $a\omega$, the maximum values of V_{T1} are small and ~ 3-5 km/s. For a value of V_{T2} in the range 15 to 20 km/s and a moderate value of t_f, we note from eqn. 5.12 that the collision

between the two shells may take place well within the PN lifetime which ranges between 10^4 to 10^5 years. If the collision is considered to be purely inelastic then from considerations of conservation of momentum, the velocity of an element of matter after collision ($V_{coll}(\theta)$) can be determined by

$$(\rho_1 l_1 + \rho_2 l_2) V_{coll}(\theta) = \rho_1 l_1 \int_{\theta}^{\theta+d\theta} V_{T1}(\theta)d\theta + \rho_2 l_2 \int_{\theta}^{\theta+d\theta} V_{T2}(\theta)d\theta$$
$$(\theta \leq \theta_c)$$

...(5.13)

where ρ_1, ρ_2, l_1, l_2 are the densities and thicknesses of the two shells respectively. Eqn. 5.13 may therefore be used to determine the terminal velocity configuration of the nebula. Using the known forms of $V_{T1}(\theta)$ and $V_{T2}(\theta)$ as given in eqn. 5.10 the above equation was numerically integrated using a Gaussian quadrature algorithm. In Fig. 5.5 we show a sample of the different terminal velocity configurations that may result. For all the terminal configurations shown in Fig. 5.5 we have assumed shells of equal thickness but considered that ρ_1 and ρ_2 may be different. Further both ρ_1 and ρ_2 have been assumed constant within the individual shells i.e., ρ_1 and ρ_2 do not depend on θ. In Fig.5.6 we show the effect of the variation of the density ratio ρ_1/ρ_2 of the two shells on the velocity structure (ρ_1 and ρ_2 assumed constant). As can be seen changes in this ratio can significantly change the axial ratio of the bipolar nebulae.

However it must be pointed out that the TB mechanism predicts that the outer shell should have a significantly smaller mass than the inner one. The exact difference in the masses of the
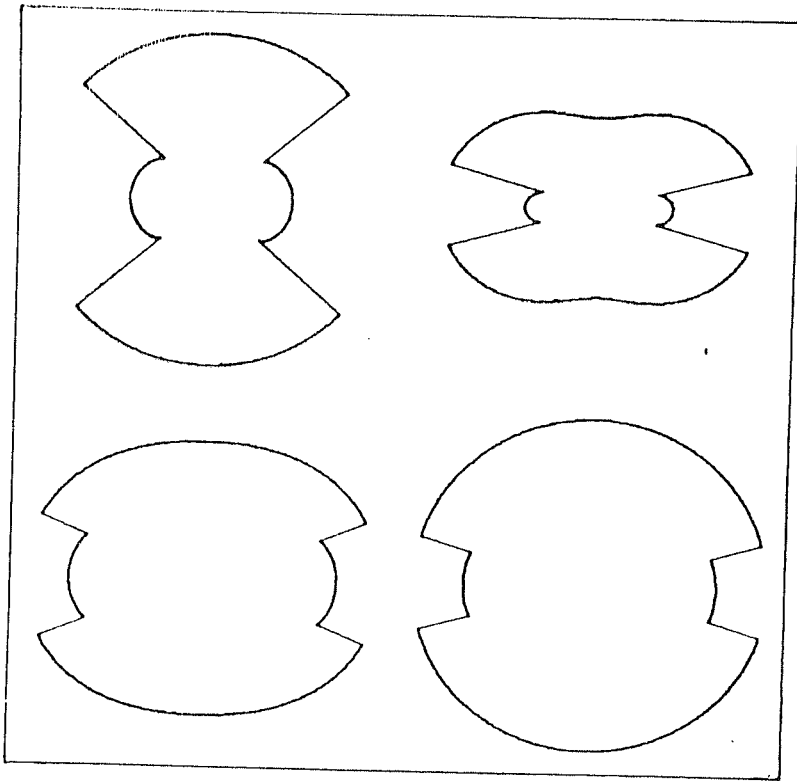
Fig.5.5: Some of the terminal velocity configurations that are possible in bipolar PNe. The velocity configurations have been obtained by considering different values of the ejection velocities of the two shells and the density ratio ρ_1/ρ_2 (see text). In each configuration $a\omega = 3.15$ km/s and $V_p = 35.0$ km/s.
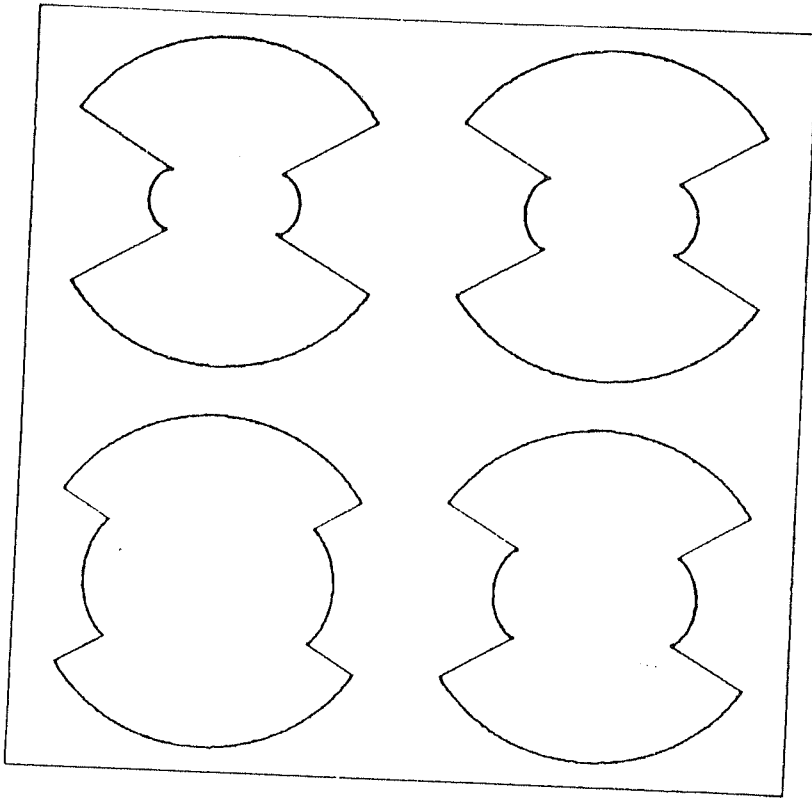
Fig.5.6: The effect of changes in the density ratio ρ_1/ρ_2 (see text) on the terminal velocity configuration of the shell is shown here. Starting from the top left corner and moving in a clock-wise direction, ρ_1/ρ_2 has the values of 2.0, 1.5, 1.0 and 0.5 respectively. In each of the configuratons, ρ_1 and ρ_2 have been assumed to be independent of θ.

two shells depends on the choice of certain parameters in their model. Since TB do not talk about a partial shell ejection it is not clear apriori that in the case of hour-glass PNe also whether the mass of the second shell should be larger than the mass of the toroidal shell. If this is so, then some of the velocity configurations given in Figs. 5.5 and 5.6 may not be admissible.

In all the configurations of Fig.5.5 and 5.6 the velocity of expansion at any point on a particular contour is proportional to the length of the radius vector to that point. Therefore as may be seen from the diagrams, our model predicts that hour-glass PNe should have a lower expansion velocity (V_{exp}) in the toroidal waist and a higher V_{exp} in the bipolar lobes. It must be pointed out here that for each of the configurations in Fig. 5.5 the maximum terminal velocity of shell 1 (outer shell)before collision is of the order of $\leq$ 4 km/s. At the critical angle θ_c it goes to 0 . For shell 2 (inner shell), the terminal velocity before collision may have any value depending on V_{ej} and ω. However if the final expansion velocity in the nebula is to be in the same range as that of PNe expansion velocities then V_{T2} must also be of the same magnitude.

The terminal shape of the nebula would depend on the epoch of observation and on the inter-shell ejection time. As has been shown (eqn. 5.12), for small or moderate inter-flash times the two shells would collide within or less than 1000 years (collision epoch). If the epoch of observation is long after the collision epoch then the terminal shape would closely resemble the terminal velocity configuration (Fig. 5.5). Therefore an hour-glass structure could result with a relatively low value of

the axial ratio. For an observational period soon after the collision epoch the bipolar lobes would appear to lie closer to the toroidal belt.

Finally we see that for suitable values of V_{ej} the first shell may be ejected as a complete shell instead of a toroidal belt. A second ejection following this would lead to a multiple shell PN. TB have not indicated the expected relative velocities of the multiple shells with respect to each other. Therefore it is not known whether it is possible, in the case of a double shell PN, that the outer shell has a larger velocity than the inner shell or viceversa. Thus our model is unable to put constraints on the kinematics of the two shells though a scope for both types of PNe exists in our model viz., in the first, the outer shell has a higher expansion velocity than the inner one and vice versa in the second case. In the case of the inner shell moving faster than the outer shell ($V_{T2} > V_{T1}$) it is possible that the two shells may not have caught up with each other if the inter-shell ejection time is large. This may be the reason for the gap between the shells in the type 1 MSPNe of CJA. CJA also point out that kinematics of the type 2 MSPNe (in which the inner shell rarely expands much faster than the outer shell) contradicts the multiple shell ejection mechanism of TB. Although CJA have not elaborated on this point, we infer from their work that their objection arises for the following reason. Since the inter shell ejection time in the TB mechanism is of the order of a few times 10^3 to a few times 10^4 years, the two ejected shells may not be able to catch up in the typical life time of a PN. However as may be seen from eqn. 5.12, if $V_{T1} \sim 20$ km/s and $V_{T2} \sim 25$ km/s, then

t$_0$ can be within a typical PN lifetime (which lies in the range 10^4 to 10^5 years) provided intermediate values of the inter-shell ejection time t$_f$ is chosen. The above example is given only to indicate that there is a possibility of the two shells catching up in spite of having a small expansion velocity difference.

A feature in our model, regarding the formation of hour-glass PNe, should be mentioned here. We find that the value of θ_c is quite sensitive to the choice of the ejection velocity V_{ej}. For example we may compute θ_c for a fixed value of aω = 3.14 km/s but for different values of V_{ej} (in this context please refer the last 3 columns of Table 5.1). We then find that V_{ej} = 34.58 km/s if matter is to escape from only the equator and from no where else i.e, θ_c = 0^0. On the other hand the minimum ejection velocity required for θ_c = 90^0 is V_{ej} = 34.86 km/s (i.e., matter escapes from all over the star with the matter from the poles just barely managing to escape). Therefore a maximum difference of only 0.28 km/s in V_{ej} (which we call ΔV_{ej}) is required between the ejection of a partial toroidal shell or a complete shell. Similarly for aω = 3.95 km/s (refer columns 4,5 and 6 of Table 5.1) we find that ΔV_{ej} = 0.45 km/s. It may be asked whether such small differences in ΔV_{ej} $\simeq$ 0.3-0.5 km/s around a mean V_{ej} $\simeq$ 35 km/s can be discriminated by the shell ejecting star. We feel the answer to this may be in the affirmative based on the following line of reasoning. If the final expansion velocity of the shell is to be equal to the observed V_{exp} values in PNe then V_{ej} cannot be much higher than the escape velocity from the star. This is because V_{exp} is equal to (V^2_{ej} - V^2_{esc})$^{1/2}$. For the typical value of V_{esc} = 35 km/s (as considered here) we note that V_{ej} is

35.35, 36.4 and 40.3 km/s for V_{exp} values of 5,10 and 20 km/s respectively. If one considers a slightly higher value of $V_{esc} = 40$ km/s then V_{ej} is found to be 40.31, 41.23, and 44.72 km/s respectively for the V_{exp} values mentioned above. We therefore see that at least in some cases, only a fraction of a km/s difference between the ejected velocities is required to produce significantly different V_{exp} values and also that V_{ej} may be very marginally close to V_{esc}.

5.5 Discussions :

We have presented so far a simple model for producing some of the commonly observed forms of PNe by taking into account gravitational braking and stellar rotation. By this means we find that in the case of a single shell ejection the spherical and ellipsoidal forms of PNe may be produced. Further we find, in the case of more than one shell ejection, that hour-glass and multiple shell PNe may be formed. It should be noted that the model requires a more rigorous treatment of certain aspects and therefore it is by no means complete. As such it does not predict directly a density contrast but rather suggests it through the fact that the ejection, under certain conditions, could be partial leading to a toroidal shell around the equator. Therefore for simplicity, the density of the shells have been assumed to be constant while considering the formation of bipolar PNe. Further more, a fuller treatment of the hydro-dynamical aspects of the interaction between the shells, while considering the bipolar PNe, is required.

In the model we have not included the effects of some other accelerative mechanisms. One of these in the radiation pressure exerted on the shell by the Lyman continuum (Lyc) emission from the central star. A detailed analysis of this effect has been made by PR who have indicated the changes that Lyc pressure can cause on the structural development of an ejected shell. The gist of their study may be given here. They find that the terminal shapes of those shells which are optically thick to Lyc radiation, do not change due to Lyc pressure but retain the same terminal shape that they had under the effect of gravitational braking (these terminal shapes in the PR model are very similar to the terminal shapes obtained in our model and which are shown in Figs. 5.2, 5.3 and 5.4). The important difference is that the expansion velocities of these shells are increased due to Lyc pressure and the final velocity, taking into account both the effects of gravitational braking and radiation pressure, is given by

$$V^2_{final}(\theta) = V^2_T(\theta) + (2\ E_{Lyc}\ r\ /\ M_n\ c) \qquad (5.14)$$

where V_T is the terminal velocity under gravitational braking, E_{Lyc} is the luminosity of the central star in the Lyman continuum, M_n is the mass of the nebula, c is the velocity of light and r is the radius of the nebula upto which it remains optically thick. For typical values of $E_{Lyc} = 4.76 \times 10^{29}$ Watts (T = 60000^0K), r = 0.1 pc, M_n = 0.05 $M_\odot$ and V_T = 10 km/s, we find from the above equation that Lyc radiation pressure can effect a change of 4 km/s in the expansion velocity. Clearly

radiation pressure can be a dominant accelerative mechanism when V_T is small and the star has a high luminosity in the Lyman continuum. For an optically thin shell, PR find that radiation pressure tends to increase the expansion velocity at the poles (i.e., the cusp regions in the diagrams of Figs. 5.2 and 5.3) and make initial configurations more spherical or spheroidal. Since the nebular ejection time is considered to be of the order of 10^3 years which is shorter than the central star evolution time for attaining high enough temperatures to emit sufficient Lyc radiation, the effect of radiation pressure may be considered as though it is switched on soon after the ejection of the shell. This assumption, however, is not justified in the case of larger core masses ($> 0.8M_\odot$) in which case the evolution is more rapid. Further, the intervening matter between the central star and the nebular shell being optically very thin (because the remnant envelope mass after the nebular shell ejection is much smaller than the mass of the latter), the brunt of the Lyc radiation may be assumed to be borne by the shell alone.

A few more accelerative mechanisms that affect the shell kinematics are the Lyman alpha (Lyα) pressure within the shell, diffusion into and deceleration by the interstellar medium and the effect due to stellar winds. The effects on the kinematics of the shell for some of the above mechanisms have been considered by other authors. Interstellar braking, for instance, becomes significant only for nebular sizes ≥ 0.5 pc (Gurzadyan, 1970, p.191). The presence of both a Reimers type wind prior to shell ejection and a fast wind after shell ejection can affect the expansion of the nebula. If the Reimers wind causes only a small

fraction of the envelope to be lost compared to the envelope mass lost during shell ejection (Barkat and Tuchman, 1980; Renzini, 1981) then it appears that it may not significantly decelerate the nebular shell. The amount of deceleration may be worked out along similar lines as in the case of interstellar braking. The changes in the shell kinematics due to a fast wind have not been incorporated in the model and needs to be included. The effects of Lyα pressure pose a "less tractable problem " (Phillips and Reay, 1977) and may significantly modify the shell kinematics. Since Lyα radiation trapped in the shell exerts pressure in all directions a velocity gradient would be set up in the shell. In such a case the force of Lyα radiation pressure on the outer layers of the nebula can be comparable with the gravitational force of the central star (Gurzadyan, 1970, p.181). Furthermore, in our model we have considered only the gross structural features of the nebula. Features like filaments, knots etc which are observed in PNe would require further insight into the gas hydrodynamics with due consideration of magnetic field effects. As may be realized, a complete and rigorous treatment of the kinematics of the shell including all the above factors is a complicated task and our proposed model is therefore presented as only a first step in this direction.

5.6 Possible formation mechanisms for some of the observed PNe:

Before concluding this chapter we discuss in this section the possible formation mechanisms for some of the PNe which we have observed. In this context we may first consider some of the hour-glass PNe viz. NGC 650/1, 2346, 2440, 2818 and 6302.

Based on the morphologies alone, we note that all these PNe may have been formed by the interacting-winds mechanism. Particularly in the case of NGC 2346, the density contrast that is required in the two-wind mechanism to form an hour-glass morphology, could be due to the binary nature of the central star of NGC 2346. In the other PNe under consideration it has not been established whether the central stars have binary companions and in these cases the density contrast has to be provided by some other physical mechanism.

The observed kinematics of all these PNe generally indicates that the expansion velocities are larger in the hour-glass lobes than in the waist.This behaviour is confirmed observationally in the case of NGC 650/1 (Recillas Cruz and Pismis, 1984), NGC 2440 (Icke, Preston and Balick, 1989 and also our observations) and in NGC 6302 (Meaburn and Walsh, 1980b). The observed triple structured profile in NGC 2818 (refer Chapter III,) can also be construed to imply similar kinematic behaviour. In NGC 2346, Walsh's (1983) observations indicate almost equal expansion velocities in the lobes and waist. But since these are the projected radial velocities along the line of sight and keeping in mind that there is evidence for a tilt in this nebula, it appears likely that the actual expansion veocities may be slightly higher in the lobes than in the waist. This kind of kinematic behaviour in hour-glass PNe is in accordance with mechanisms for hour-glass PNe formation based on the interacting-winds scenario (for e.g. Icke, Preston and Balick, 1989). It also agrees with our model for hour-glass PNe wherein we also expect larger expansion velocities in the lobes than in the

central toroidal waist. However in NGC 650/1, the kinematics of the bright central bar suggests that it is an elliptical ring in projection (refer Chapter IV) and as explained earlier such a geometry is not expected from the interacting-winds scenario. In the context of our model also, the central toroidal waist of an hour-glass PNe is expected to be of a circular shape and therefore is in variance with what is observed in NGC 650/1.

Similarly the elongated elliptical disc seen at a position angle of $\sim 45^0$ in NGC 2440 does not perhaps fit straight into the interacting-winds scenario or our model. However as mentioned earlier, in the absence of kinematic data for this disc, it is difficult to decide whether it is truly elliptical or a tilted circular disc seen in projection. The orientation of the disc with respect to the hour-glass structure of NGC 2440 suggests that it is probably of the former geometrical form. It is relevant to ask how such an extended disc is formed at the waist of the hour-glass lobes of NGC 2440. A possible explanation is that the extension of the disc is caused due to the effect of Lyc radiation pressure. It is expected that, if the hour-glass lobes are optically thin while the central waist is optically thick, then radiation pressure would preferentially accelerate the matter in the central waist thereby giving it the appearance of an extended disc. Such a disc should however be circular instead of elliptical because of the isotropic nature of the Lyc radiation as well as the nebular matter in the disc. It may be noted that the near equality of the Hydrogen and Helium Zanstra temperatures in this PN viz. $310,000^0$K and $400,000^0$K respectively (Atherton, Reay and Pottasch, 1986) may be construed to imply that the nebula is

optically thick to Lyc radiation. Such an interpretation for the optical depth of the nebula must however be made with some caution for reasons pointed out by Pottasch (1984) and Kaler (1985). On the other hand Barker (1978) has shown that optically thick PNe are generally characterized by having a higher [NII] electron temperature compared to the [OIII] temperature - the opposite of which is found in NGC 2440 (Shields, Aller, Keyes and Cyzak, 1981).

Finally we consider the two multiple shell PNe that have been observed - IC 4593 and NGC 1535. Regarding IC 4593 we have already discussed at length (in Chapter III) as to how its kinematics is not easily explainable by the interacting-winds scenario. With reference to NGC 1535, it has been mentioned that its morphology consists of two shells, with the inner one constricted by a toroidal ring of matter. In the interacting-winds mechanism such a morphology may be explained by considering that the bipolarity seen in the inner shell is due to the propagation of a fast wind into an anisotropic AGB wind (which is manifested in NGC 1535 as the outer shell). The existence of the fast wind is confirmed in the P Cygni profiles observed in the ultraviolet spectrum of NGC 1535 and the terminal velocities of which have been measured to be ~ 2000 km/s (Adam and Koppen, 1985; Cerruti-Sola and Perinotto, 1985). However the observed kinematics of the two shells with the outer shell expanding marginally slower than the inner one, is difficult to reconcile with the two-wind mechanism as mentioned earlier. In order to explain the morphology of NGC 1535 in the context of our model, we have to assume three ejections - the first ejection corresponds to the outer shell and

the next two lead to the formation of the bipolar inner shell as per our proposed model for the formation of hour-glass PNe. Since we cannot put constraints in our model for the expected relative velocities of the inner and outer shells, the observed kinematics of these shells in NGC 1535 may not go against our model. On the other hand, in the case of the bipolar inner shell of NGC 1535 our model predicts faster expansion for the hour-glass lobes than for the equatorial toroid which seems to be in agreement with Clayton's (1988) observations. In general we note from the work of CJA that the morphologies and kinematics of MSPNe provide an important means by which the theoretical predictions of different mechanisms for PNe formation may be tested. However, the detailed kinematic studies of MSPNe have only recently begun and not much data is available. But even with the limited data available CJA indicate rather clearly that there are a few observed features in MSPNe which are not easily explainable by either the multiple shell ejection mechanism of TB or the two-wind and three-wind mechanisms. It would therefore appear that although major advances have been made in our understanding of the different methods by which PNe are formed and consequently shaped, there still remain certain areas where our knowledge is incomplete and where further studies are required. We end this chapter by summarizing the main conclusions that have been reached.

5.7 Conclusions:

(i)   A general mechanism is proposed, based on a multiple shell ejection process, to account for the the commonly observed morphological forms of PNe viz. spherical, ellipsoidal,

hour-glass and multiple shell PNe. We indicate a new method for the formation of hour-glass PNe which first requires the ejection of a partial toroidal shell (caused by rotation of the progenitor star) followed by the ejection of a second more rapidly expanding shell. In extension, we show that the ejection of two complete shells lead to the formation of a multiple shell PN. We also show that the predicted kinematics of the waist and hour-glass lobes of bipolar PNe formed by the proposed mechanism is consistent with the observed velocity field in some of the well-known hour-glass PNe.

(ii)   In the event of a single shell ejection we show how the spherical and ellipsoidal morphological forms of PNe can arise and also indicate the velocity fields that should be expected in them.

CHAPTER VI

SUMMARY AND SCOPE FOR FUTURE WORK

We summarise in this chapter the work contained in the thesis with emphasis on the important and new results that have been obtained. The scope for future work, as an extension of and related to the present studies, is also indicated.

6.1 Summary :

The thesis is devoted to the kinematic studies of PNe. In order to carry out this investigation a high-resolution, piezo-scanning cum servo-controlled Fabry-Pérot spectrometer was designed and fabricated. Kinematic observations were made of ten selected PNe. In six of these PNe viz. NGC 2818, 5882, 6153, 6302 and IC 4406 and 4593, observations were made only in the central region while in the remaining PNe viz. NGC 2440, 2346, 1535, and 650/1 the velocity field was mapped relatively more extensively, thereby permitting the construction of spatio-kinematic models. The observations of all the PNe were carried out in either one or more of the following emission lines viz. [OIII] 5007Å, Hα 6563Å and [NII] 6584Å.

The important kinematic results obtained from this investigation can be divided into four broad categories as follows:

(i) The present study has allowed us to confirm whether the observed kinematics of some of the PNe is in accordance with that

predicted by some of the proposed physical mechanisms for PNe formation and morphological shaping. In the PN IC 4593, we find evidence that the outer shell is expanding faster than the inner one. This result is at variance with the prediction of the interacting-winds mechanism for PNe formation and to bring the observed results in conformity with the above mechanism, additional accelerative mechanisms on the outer shell have to be invoked (for example thermal diffusion into vacuum or the action of radiation pressure on dust present in the outer shell). In NGC 6153, we find evidence for a bipolar flow which is not too common a phenomenon in PNe. Although a hydrodynamical model based on the two-wind mechanism has been proposed by Balick (1987) to explain such collimated bipolar flows, it appears from the morphology of NGC 6153 that the origin of the bipolar flow may not be attributable to the above model and therefore needs an alternative explanation. In the case of NGC 2440, we have constructed a detailed spatio-kinematic model to explain the observed kinematics and morphology of the nebula. The model assumes an hour-glass structure for the nebula with the added presence of a disc of matter at the intersection plane of the hour-glass lobes. Such a geometrical form is consistent with the apparent morphology of NGC 2440 and more important is the fact that such an assumed geometrical form can result from models for the formation of hour-glass PNe based on the interacting-winds mechanism. We find that our model explains satisfactorily the kinematic results obtained by us in this nebula and also reproduces well the echelle slit spectrum images of this PN as obtained by other observers. This therefore implies that the interacting-winds mechanism could

be the one that is responsible for the formation and shaping of NGC 2440. However one discordant feature that is noticed is the apparently elliptical shape of the disc seen across the face of NGC 2440. In the interacting-winds mechanism this disc is predicted to be circular. Similarly in the hour-glass PN NGC 650/1, our kinematic results plus those of other obsevers, indicate that the central waist is elliptical in shape which is again at variance with predictions with the interacting-winds mechanism. Another PN whose observed kinematics permits a conjecture on its formation mechanism is NGC 2818. The unusual triple-structured line profiles obtained in this hour-glass PN in the [OIII], Hα and [NII] lines can be interpreted to represent the kinematics of a slower expanding waist and faster expanding hour-glass lobes. Such a kinematic configuration is again consistent with predictions from the two-wind mechanism for PNe shaping.

(ii) From the kinematic studies we have been able to draw inferences regarding some of the physical conditions in PNe. In the case of the multiple shell PN NGC 1535, we have generated emission line profiles and compared them with the observed profiles. We find that the kinematics of NGC 1535 may be well explained by assuming that the physical conditions existing in the nebula are represented by a constant expansion velocity (instead of a $v = \alpha r$ relationship that is generally used) of 21 km/s in the [OIII] line emitting region, a $n_e(r) \propto r^{-3}$ relation for the dependence of electron density on distance and the presence of turbulence in the inner shell characterized by a most probable velocity of 7.5 km/s. We have also estimated the nebular

temperatures (by comparison of the widths of the Hα and [NII] lines) in two other PNe viz. NGC 2346 and NGC 6153 and shown that they are in fair agreement with values derived by other authors from the intensity ratios of forbidden lines.

(iii) The present study has yielded new expansion velocity results in certain PNe for which such measurements had not been made earlier. New V_{exp} values are valuable generally since they increase the sample size used in statistical studies aimed at studying the evolution of PNe. An example of such work is the expansion velocity versus radius correlation study as outlined for example in Sabbadin (1984) or Weingberger (1989). The first results presented here consist of the determination of the [OIII] expansion velocity in NGC 2346, 5882, 6153 and IC 4593. The [NII] expansion velocity in NGC 6153 is also new. In addition, our observations also supplement the available V_{exp} data particularly in NGC 650/1, 2818 and 2440. These three nebulae have not been studied too well in the [OIII] line and in at least one of these PNe viz. NGC 650/1 our observations indicate a significantly different V_{exp} value than the only other existing measurement (Sabbadin and Hamzaoglu, 1982).

(iv) This study has also demonstrated the importance and relevance of the geometrical/morphological aspect of PNe in explaining certain observed features. In the case of NGC 2346, we have shown how the puzzling spatial variation of the relative intensity of the blue and red components observed in this nebula (by Walsh, 1983) can be explained by assuming a simple morphological model for the nebula. In the model the nebula is

assumed to be of hour-glass form and tilted towards the observer. Similarly in NGC 5882, we find an interesting behaviour of the measured expansion velocity when different aperture sizes are used. Due to the apparent spherical shape of this PN, it is expected that the expansion velocity should decrease with increasing aperture size. We instead find evidence for an opposite trend indicating thereby that the true morphology of this nebula is probably different from the apparent one.

Having presented the observations and the kinematic results of the PNe, we next made a more detailed discussion of how the different morphological forms of PNe can arise. We indicated how the interacting-winds mechanism faces perhaps some difficulty in explaining the morphologies and kinematics of certain types of multiple shell planetary nebulae. We also discussed a model by Phillips and Reay (1977), which by assuming a rapid single shell ejection shows how spherical, ellipsoidal and toroidal forms of PNe can be formed. However hour-glass PNe are not formed in this model. In view of the above points we proposed a general model to account for the commonly observed morphological forms of PNe viz. spherical, ellipsoidal, hour-glass and multiple shell PNe. In particular, a new method is proposed for the formation of hour-glass PNe which first requires the ejection of a partial toroidal shell (caused by rotation of the progenitor star) followed by the ejection of a second more rapidly expanding shell. In extension, we showed that the ejection of two complete shells lead to the formation of a multiple shell PN. We also showed that the predicted kinematics of the waist and hour-glass lobes of bipolar PNe formed by the proposed mechanism appears to be

consistent with the observed velocity field in some of the hour-glass PNe that are covered in this study viz. NGC 650/1, 2346, 2440, 2818 and 6302. In the event of a single shell ejection we showed how the spherical and ellipsoidal morphological forms of PNe can arise and also indicate the velocity fields that should be expected in them. Finally we discuss the shortcomings of the proposed model and indicate the other accelerative mechanisms that need to be considered to make the model more rigorous and complete.

6.2 Scope for future work :

It is perhaps fitting to indicate here some suggestions for future work in this field that can serve as a useful extension of the present studies. Further some of the difficulties that have been encountered may also be stated along with remedial measures.

One factor, which has been largely detrimental to studying the velocity field more extensively has been the use of a photo-multiplier tube (PMT) as a detector. Since a PMT is essentially a single channel detector it is difficult to map a PN in several regions within the restricted telescope time that is available. To overcome this handicap therefore, it is necessary to use an array detector. Such an array detector viz. the Imaging photon detector (IPD) which consists of a microchannel plate-stack and a position sensitive detector has been procured. By coupling this detector to the F.P.S. that has been used for the present study it would be possible to obtain both high spatial and spectral resolution images of a PN. Further since the IPD has a

much lower dark-count rate than the PMT (although they both have almost the same quantum efficiency) it would be possible to extend the studies to fainter objects.

As has been stressed at several places, the kinematics of multiple shell PNe can prove to be a critical test for many of the mechanisms that have been proposed for PNe formation. It has also been mentioned that not much work has been done in this direction. It is therefore proposed to study the kinematics of these PNe extensively. The IPD would be ideally suited for studying the outer shells or extended haloes of these PNe which are generally very faint.

It is also necessary to study some of finer features like filaments, knots etc.that are seen in several PNe (for example in NGC 650/1, 2440 and in the Helix nebula NGC 7293). The kinematic studies of such structures have hardly been carried out and very little theoretical work has been done in either explaining the origin of such structural features or in predicting their kinematics. It is therefore necessary to study the kinematics of such structures and see what physical processes need to be invoked to explain their observed properties.

It would also be useful to study a few selected PNe that may again prove instrumental in deciding the mechanisms responsible for the shaping of PNe. One such example is the planetary nebula Sp 1. As has been mentioned, Bond and Livio (1990) have proposed that a density contrast can be created in the ejected matter from a PN with a binary nucleus and this contrast can lead to the formation of an hour-glass PN. But in spite of having a binary nucleus Sp 1 still displays a spherical

morphology. It is however possible that Sp 1 is actually an hour-glass PN seen pole-on and in this context kinematic studies can help establish its true morphology.

The magnitude of turbulence in PNe is another aspect that possibly needs a more detailed investigation. The line profiles in PNe generally show a much larger width than that expected due to the effects of thermal broadening. To account for the excess broadening the presence of turbulence is invoked or a velocity dispersion in the nebular matter along the line-of-sight is considered (i.e., a dependence of velocity on radial distance is assumed). However, by determining the width of the line profiles obtained from regions situated at the edge of the PN shell, the contribution due to velocity dispersion may be made negligible and thereby a better estimate of the turbulent velocities in PNe can be obtained.

We hope to investigate and find answers to the above problems in the future.

REFERENCES

Acker, A. , 1976, Publ. Obs. Strasbourg 5, fasc.1

Acker, A. and Jacniewicz, G., 1985, Astron. Astrophys., 143, L1

Adam,J. and Köppen,J., 1985, Astron. Astrophys., 142, 461

Allen,C.W., 1973, Astrophysical quantities (Athlone Press, London)

Aller, L.H., 1956, " Gaseous Nebulae", Chapman and Hall, London

Aller, L.H., Czyzak, S.J and Kaler, J.B., 1968, Astrophys. J.,151, 187

Aller, L.H. and Walker, M.F., 1970, Astrophys. J., 161, 917

Aller, L.H. and Czyzak, S.J, 1979, Astrophys. Space Sci., 62, 397

Anandarao, B.G., Suhasini, S. Rao, 1986, Bull.Astr.Soc. India,14, 25.

Atherton , P.D. , Reay , N.K., Ring , J. and Hicks , T.R. , 1981 Opt. Engg., 20 , 806

Atherton, P.D., Reay, N.K. and Pottasch, S.R., 1986, Nature, 320, 423

Balick, B., Preston, H.L. and Icke,V., 1987, Astron. J., 94, 1641

Balick,.B., 1987 , Astron.J, 94 ,671.

Barkat,.Z. and Tuchman,Y.,1980, Astrophys. J ,237,105.

Barker, T. ,1978, Astrophys. J., 219, 914

Benett, C.L., 1987, Astrophy. J., 323, L123

Bianchi, L., Grewing, M., Barnstedt, J. and Diesch,Ch., 1989,in IAU Symp. No. 131, "Planetary Nebulae", ed:S.Torres-Peimbert, Kluwer, Holland

Bianchi, L., Grewing, M., Falcetta,C. and Baessgen, M., 1987, in "Planetary and Proto-Planetary Nebulae : From IRAS to ISO", ed:A.Preite-Martinez, D.Reidel, Hoiland, p.153

Bland, J. and Brent Tully, R. , 1989, Astron. J., 98(2), 723

Bohm, D. and Aller, L.H., 1947, Astrophys. J., 105, 131

Bohuski, T.J. and Smith, M.G., 1974, Astrophys. J., **193**, 197

Bond, H.E. and Livio, M., 1990, (preprint), to appear in Astrophys. J., June 1, 1990

Born, M. and Wolf, E., 1965, "Principles of Optics", Pergamon Press

Cahn, J.H. and Kaler, J.B. , 1971, Astrophys. J. Suppl., **22**, 319

Calvert, N. and Peimbert, M., 1983, Rev. Mexicana Astron. Astrof.,**5**, 319

Cerruti-Sola, M. and Perinotto, M., 1985, Astrophys. J., **291**, 237

Chabbal , R., 1958 , Rev. Opt. , **37** , 49

Chandrasekhar , S., 1969, Ellipsoidal figures of Equilibrium(Yale University).

Christiani, S., Sabbadin, F. and Ortolani,S., 1989, in IAU Symp.No. 131, "Planetary Nebulae", ed: S. Torres- Peimbert, Kluwer, Holland

Chu, Y.H. and Jacoby,G., 1987, in "Late stages of stellarevolution", ed: S.Kwok and S.R.Pottasch, D.Reidel, Holland, p.351

Chu, Y.H., Jacoby, G.H. and Arendt, R., 1987, Astrophys.J.Suppl., **64**, 529.

Chu, Y.H., 1989, in IAU Symp. No. 131, "Planetary Nebulae",ed: S. Torres-Peimbert, Kluwer, Holland

Clayton,C.A., 1988 ,Astron.Astrophys.,**195** ,263.

Cohen, M., Barlow, M.G., 1975, Astrophys. Lett., **16**, 165.

Cohen, M., Harrington, J.P. and Hess,R., 1984, Astrophys. J., **283**, 687

Courtes, G., Louise, R. and Monnet, G., 1968, Ann. d'Astr., **31**, 493.

Curtis, H.D., 1918, Pub. Lick. Obs., **13**, 57

Daub, C.T. , 1982, Astrophys. J., **260**, 612

Desai, J.N. , 1984, Proc. Indian. Acad. Sci.,(Earth Planet Sci), **93**, 189

Dopita, M.A. , 1972, Astrophys. Space Sci., **18**, 350

Dufour, R. , 1984, Astrophys. J., **287**, 341

Dyson, J.E. and Meaburn, J.,1971, Astron. Astrophys., **12**, 219

Fabry, C. and Pérot, A. , 1899, Ann. Chim. Phys(7), **16**, 115

Foukal, P., 1969, Astrophys. Space Sci., **4**, 127

Friend, D.B. and Abbott, D.C., 1986, Astrophys. J., **311**, 701

Gathier, R. , 1987, Astron.Astrophys. Suppl. Ser., **71(2)**, 245

Geyling, F.T. and Westerman, R.H., 1971, "Introduction to orbital mechanics", Addison Wesley, 1971, pp. 170-175

Gieseking,F. and Solf,J., 1986, Astron. Astrophys., **163**, 174

Greig, W.E., 1971, Astron. Astrophys., **10**, 161

Gurzadyan, G.A.,1970, Planetary Nebulae, trans. and ed:D.G.Hummer, D.Reidel, Holland

Harm, R. and Scharwzschild, M., 1975, Astrophys. J., **200**, 324

Healy , A.P. and Huggins, P.J., 1988, Astron. J., **95**, 866

Heap, S.R., 1987, Nature, **326**, No. 6113, 571

Heathcote,S.R. and Weller, W.G., 1987, in "Late stages of stellar evolution", ed: S.Kwok and S.R.Pottasch, D.Reidel, Holland

Hernandez , G. , 1966, Appl. Opt., **5**, 1745

Hernandez , G. , 1970, Appl. Opt., **9**, 1591

Hernanedez ,G. , 1974, Appl. Opt., **13**, 2654

Hernanedez ,G. , 1986, "Fabry-Pérot interferometers", University Press, Cambridge

Hicks, T.R., Reay, N.K., Scaddan, R.J., 1974, J. Phys. E (Sci.Instrum.) **7**, 27.

Iben (Jr) , I. and Truran, J.W., 1978, Astrophys. J., **220**, 980

Iben (Jr) ,I., 1981, in "Physical processes in Red giants", eds: I. Iben(Jr.) and A. Renzini, D.Reidel, Holland

Iben (Jr) ,I., 1985, Q. Jl. R. astr. Soc., **26**, 1

Icke, V. , 1988, Astron. Astrophys., **202**, 177

Icke, V., Preston, H.L. and Balick, B. 1989, Astron. J., **97(2)**,462

Jacquinot, P., 1954, J.Opt. Soc.Amer, **44**, 761

Jacquinot, P. , 1960, Rep. Prog. Phys. ,**23**, 267

Jacniewicz., G., Acker, A., 1986, Astron. Astrophys., **160**, L1-L3.

Jones, R.V, Richards, J.C.S., 1973, J.Phys. E.(Sci.Instrum.) 6 , 589.

Kahn, F.D. and West, K.A. ,1985, Mon. Not. Roy.astr. Soc., **212**, 837

Kaler, J.B. , 1974, Astron. J., **79**, 594

Kaler, J.B. and Aller, L.H., 1974, Publ. Astron. Soc. Pacific, **86, 635**

Kaler, J.B., 1976, Astrophys. J. Suppl., **182**, 31

Kaler, J. B., 1985, Ann. Rev. Astron. Astrophys., **23**,101

Kaler, J. B. , 1986, Astrophys. J., **308**, 322

Keeley, D.A., 1970, Astrophys. J., **161**, 643.

Khromov, G.S. and Kohoutek, L., 1967, IAU symp. No. 34, eds: D.E. Osterbrock and C.R. O'Dell, D.Reidel, Holland, p.227

Kohoutek, L., Senkbeil, G., 1973. In Les Nebuleuses Planetaires, 18th Liege Collq., P.485.

Kohoutek ,L., 1983, Mon.Not.R.astr.Soc., **204**, 93p

Kolesnik, I.G. and Pilyugin, L.S., 1986, Sov. Astron., **30**(2), 169

Kudritzki, R.P. and Reimers,D., 1978, Astron. Astrophys., **70**, 227

Kwok, S. , 1982, Astrophys. J., **258**, 280

Kwok, S., Purton, C.R. and Fitzgerald, P.M., 1978, Astrophys. J., **219**, L125.

Lang, K.R., 1974, "Astrophysical formulae", Springer-Verlag

Lester, D.F. and Dinerstein, H.L., 1984, Astrophys. J., **281**, L67

Loiise, R., 1974, Mem. Soc. Roy. Liege, **4**, 465

Louise, R. and Pascoli, G., 1985, Astron. Astrophys., **150**, 285

Maciel, W.J. and Pottasch, S. R. ,1980, Astron. Astrophys., **88**, 1

Mallik,D.C.V. and Peimbert,M.,1988, Rev.Mexicana. Astron. Astrof., **16**, 111

Mathews, W.G.,1978, in IAU Symp.No. 76, "Planetary Nebulae", ed: Y.Terzian, DReidel, Holland, p.251

Meaburn, J. , 1976, Detection and Spectrometry of Faint Light, D. Reidel, Holland

Meaburn, J. and Walsh, J. R. 1980a, Mon. Not. Roy. astr. Soc., 191, 5P

Meaburn, J. and Walsh, J. R. , 1980b, Mon. Not. Roy. astr. Soc., 193, 631

Meatheringham, S.J. Wood, P.R. and Faulkner, D. J. , (refer Weinberger, 1989)

Mendez,R.H., 1978, Mon. Not. Roy. astr. Soc., 185, 647

Mendez, R.H., Niemala, V.S., 1981, Astrophys.J., 250, 240.

Mendez, R.H., Gathier, R., Niemala, V.S., 1982, Astron. Astrophys., 116, L5.

Mendez,R.H., Kudritzki, R.P., Herrero, A., Husfeld, D. and Groth,H.G., 1988, Astron. Astrophys., 190, 113

Milne, D.K. and Aller, L.H., 1975, Astron. Astrophys., 38,183

Milne, D.K. and Aller, L.H., 1982, Astron. Astrophys. Suppl. Ser.,50, 209

Minkowski, R. , 1964, Publ. Astron. Soc. Pacific. ,76, 69

Minkowski, R. and Aller, L.H., 1956, Astrophys. J., 124, 93

Morris, M., 1981, Astrophys. J., 249, 572

O'Dell, C.R., 1962, Astrophys. J., 135, 371.

Ortolani, S. and Sabbadin, F. , 1985, Astron. Astrophys. Suppl. Ser. 62, 17

Osterbrock, D.E. , 1974, Astrophysics of Gaseous Nebulae, Freeman, San Francisco

Osterbrock,D.E., Miller,J.S., Weedman,D.W., 1966, Astrophys. J., 145, 697

Paczynski, B. and Ziolkowski, J., 1968., IAU symposium 34, Planetary Nebulae, ed. D.E.Osterbrock and C.R. O'Dell,D. Reidel, Holland

Paczynski, B., 1971, Acta. Astron., 21, 417

Paczynski, B., 1975, Ap. J., 202, 558.

Peimbert, M. and Torres-Peimbert, S. ,1971, Boll. Obs. Tonantzintlay Tacubaya, 6, 21

Peimbert, M., 1981, Physical Processes in Red Giants, P.409, D.Reidel , Holland.

Perek, L., Kohoutek, L., 1967, Catalogue of Galactic Planetary Nebulae (Czechoslovak Academy of Sciences, Prague).

Phillips, J.P. and Reay, N.K., 1977, Astron.Astrophys., **59**, 91.

Poe, C.H. and Friend, D.B., 1986, Astrophys. J., **311**, 317

Pottasch, S.R., 1984, Planetary Nebulae, D.Reidel , Holland.

Pottasch,S.R., Dennefeld, M. and Mo,J.-e.,1986 ,Astron. Astrophys., **155**, 397

Press, W.H., Flannery, B.P., Teukolsky, S.A. and Vetterling, W.T. 1986, Numerical Recipes, Cambridge University Press

Ramsay, J.V. , 1962, Appl. Opt., **1** ,number 4, 411

Ramsay, J.V., 1966, Appl. Opt., **5**, number 8, 1297

Reay, N.K, Hicks, T.R., Atherton, P.D., "Servo-control of Fabry-Pérot Interferometers: 1-Technique", Instrumentation in Astronomy V,A.Boksenberg, D.L.Crawford, Eds. Proc.S.P.I.E. **445**, 13-20, 1984.

Recillas-Cruz, E. and Pismis, P.,1984 Mon. Not. Roy. astr. Soc., **210**, 57

Reimers, D.,Mem. Soc. Roy. Sci. Liege, 6e Ser.8., 369

Renzini, A. and Voli, M., 1981, Astron. Astrophys., **94**, 175

Renzini, A., 1981, in Physical Processes in Red giants, ed. I.Iben.Jr. and A.Renzini ,D. Reidel, Holland

Ring, J., 1978, Proceedings of the fourth International Colloquium on Astrophysics held in Trieste, P.93

Robinson, G.J., Reay, N.K. and Atherton, P.D. , 1982 Mon. Not. Roy. astr. Soc., **199**, 649

Roessler, F.L. , 1974, Methods of Experimental Physics, Vol.12-partA, ed: N.Carleton, Academic Press, New York and London

Roth, M., Echevarria, J., Tapia, M., 1984, Astron.Astrophys., **137**, L9.

Roxburgh, I.N., 1967, Nature, **215**, 838.

Sabbadin, F., 1976, Astron.Astrophys., **52**, 291.

Sabbadin, F. and Hamzaoglu, E. , 1981, Mon. Not. Roy. astr. Soc., **197**, 363

Sabbadin, F. and Hamzaoglu, E. , 1982, Astron. Astrophys., **110**, 105

Sabbadin, F., 1984, Astron. Astrophys. Suppl. Ser., **58**, 273.

Sabbadin,F., Bianchini,A. and Hamzaoglu,E., 1984, Astron. Astrophys., **136**, 193

Sabbadin,F., Gratton, R.G., Bianchini,A. and Ortolani, S., 1984, Astron. Astrophys., **136**, 181

Sahu, K.C., Desai, J.N. and Jog, N.S. ,1984, Proc. Soc. photo-opt., Instr. Eng., **445**, 33

Sahu, K.C. , 1985, Ph.D Thesis, University of Gujarat

Schaeffer, B.E., 1985b, Astrophys.J., **297**, 245.

Schmidt-Voigt, M. and Köppen, J. , 1987a, Astron. Astrophys., **174**, 223

Schmidt-Voigt,M. and Köppen,J., 1987b, Astron. Astrophys., **174**, 211

Schönberner, D., 1981, Astron. Astrophys., **103**, 119

Schönberner, D., 1983, Astrophys. J., **272**, 708

Schönberner, D. and Weideman, V., 1983, IAU Symp. No. 103, D.Reidel, Holland

Shields, G.A., Aller, L.H., Keyes, C.D. and Czyzak, S.J., 1981, Astrophys. J., **248**, 569

Smeethe, M.J. and James, J.F. , 1971,J.Phys. E: Sci. Instrum. 429

Smith, R.L. and Rose, W.K., 1972, Astrophys. J., **176**, 395.

Soker, N. and Livio, M., 1988, Astrophys. J., **339**, 268

Taylor, K., 1979, Mon.Not.R.astr.Soc., **189**, 511.

Thorne, A.P., 1974, "Spectrophysics", Chapman and Hall.

Tifft,W.G., Connolly, L.P. and Webb,D.F., 1972, Mon. Not. Roy. astr. Soc., **158**, 47

Tolansky, S., 1947, "High resolution spectroscopy", Methuen Press

Torres-Peimbert, S. and Peimbert, M., 1977 ,Rev.Mexicana. Astron. Astrof., **2**, 181

Tuchman, Y., Sack, N. and Barkat, Z., 1978, Astrophys. J., **219**, 183

Tuchman, Y., Sack, N. and Barkat, Z., 1979, Astrophys. J., **234**, 217.

Tuchman, Y. and Barkat, Z., 1980, Astrophys. J., **242**, 202.

Turoff, M., 1965. A computer model for planetary nebulae. Dissertation printed at the Institute for Defence Analysis, Arlington, Virginia,U.S.A.

Users Manual for CS100, Queensgate Instruments Ltd., Middlesex, England.

Van de Hulst, H.C. and Reesinck, J.J.M. , 1947, Astrophys. J., **106**, 121

Vityazev, V. V., 1969, Astrofizika, **5**, 183.

Volk, K.M. and Kwok, S., 1985, Astron. Astrophys., **153**, 79

Walsh, J.R., 1983, Mon. Not. R. astr. Soc., **202**, 303.

Walsh, J.R. and Meaburn, J., 1987, Mon. Not. R. astr. Soc., **224**, 885

Weinberger, R. , 1989, Astron. Astrophys. Suppl. Ser. **78**, 301

Weller, W.G. and Heathcote, S.R. , 1987, in Late Stages of Stellar Evolution, eds : S.Kwok and S.R.Pottasch, D. Reidel, Holland

Welty, D.E., 1983, Publ.Astron. Soc.Pacific., **95**,217.

Wilson, O.C., 1950, Astrophys. J., **111**, 279.

Wood, P.R.,1974, Astrophys. J., **190**, 609.

Woyk, E., 1967, IAU symp. No. 34, eds: D.E. Osterbrock and C.R. O'Dell, D.Reidel, Holland

Zanstra, H., 1931, Publ. Dom. Astrophys. Obs., **4**, 209

Zuckerman, B. and Gatley, I., 1988, Astrophys. J., **324**,501